INFORMATION TO USERS

This manuscript has been reproduced from the microfilm master. UMI films the text directly from the original or copy submitted. Thus, some thesis and dissertation copies are in typewriter face, while others may be from any type of computer printer.

The quality of this reproduction is dependent upon the quality of the copy submitted. Broken or indistinct print, colored or poor quality illustrations and photographs, print bleedthrough, substandard margins, and improper alignment can adversely affect reproduction.

In the unlikely event that the author did not send UMI a complete manuscript and there are missing pages, these will be noted. Also, if unauthorized copyright material had to be removed, a note will indicate the deletion.

Oversize materials (e.g., maps, drawings, charts) are reproduced by sectioning the original, beginning at the upper left-hand corner and continuing from left to right in equal sections with small overlaps.

Photographs included in the original manuscript have been reproduced xerographically in this copy. Higher quality 6" x 9" black and white photographic prints are available for any photographs or illustrations appearing in this copy for an additional charge. Contact UMI directly to order.

Bell & Howell Information and Learning
300 North Zeeb Road, Ann Arbor, MI 48106-1346 USA

UMI®
800-521-0600

Hot Workability of Magnesium Alloys

Aaron Absalom Mwembela

A thesis

in

The Department

of

Mechanical Engineering

Presented in Partial fulfillment of the requirements

for the Degree of Doctor of Philosophy at

Concordia University

Montreal, Quebec, Canada

September 1997

ABSTRACT

Hot Workability of Magnesium Alloys

Aaron Absalom Mwembela, Ph.D.

Concordia University, 1997

For the alloy AZ91 (Mg-9.0Al-0.7Zn-0.13Mn) die cast specimens were subjected to torsion testing at 150, 180, 240, 300, 420 and 450°C at 0.05 0.5 and 5.0 s^{-1}. The as-cast specimens exhibited hot shortness at 360°C and above; however in that domain, after prior thermomechanical processing (TMP) at 300°C, they showed much improved properties (which were reported along with as-cast properties at 300°C and below).

For AZ31-Mn (Mg-3.2Al-1.1Zn-0.34Mn), AZ31 (Mg-2.8Al-0.88Zn-0.01Mn), AZ63 (Mg-5.5Al-2.7Zn-0.34Mn) and ZK60 (Mg-5.7Zn-0.65Zr-0.01Al), the specimens were subjected to hot torsion testing in the range 180 to 450°C and 0.01, 0.1, and 1.0 s^{-1}. In the temperature range below 300°C flow curves rise to a peak with failure occurring immediately thereafter. Above 300°C the flow curves exhibited a peak and a gradual decline towards steady state. The temperature and strain rate dependence of the strength is described by a sinh-Arrhenius equation with Q_{Hw} between 125 and 144 kJ/mol; this indicates control by

climb in comparison with creep in the range 200-400°C. The alloy strength and activation energy declined in the order AZ63, AZ31-Mn, AZ91, AZ31 and ZK60, while ductility increased with decreasing strength.

In working of Mg alloys from 150 to 450°C, the flow curves harden to a peak and work soften to a steady state regime above 300°C. At temperatures below 300°C, twinning is observed initially to bring grains into more suitable slip orientations. At high T a substructure develops due to basal and prismatic slip, forming cells of augmented misorientation first near the grain boundaries and later towards the grain cores. Near the peak, new grains appear along the old boundaries (mantle) as a result of dynamic recrystallization DRX but not in the core of the initial grains. As T rises, the new grains are larger and the mantle broader; enhanced DRX results in higher ductility. At intermediate T, shear bands form through alignment of mantle zones resulting in reduced grain sizes and higher misorientation. Dynamic recrystallization does not become general as in Cu or Ni, thus it does not markedly raise the ductility. Retention of the hot worked substructure, or the refined grains, improves the strength and ductility of the product.

ACKNOWLEDGEMENTS

The author wishes to express his gratitude and appreciation to his supervisor Dr. Hugh J. McQueen who provided guidance and encouragement throughout this research project. Special thanks go to Dr. Terry Maccagno who gave technical assistance with respect to the mechanisms of the torsion testing machine and computer programming. The author gratefully acknowledges the advice of Janet Bowles with respect to metallographic work presented in this thesis. The author acknowledges the help of Dr. Elena Konopleva in the preparation of some of the AZ31-Mn, AZ31 and AZ91 specimens. He is also grateful to Timminco Ontario for providing cast specimens of Mg alloys and also M. Avedesian and M. Pekguleryuz who authorized provision of AZ91 samples. He would like to thank the Canadian Commonwealth Scholarship and Fellowship plan (CCSFP), Natural Sciences and Research Council of Canada (NSERC) and Fonds pour la Formation des Chercheurs et l'Aide à la Recherche (FCAR) for providing the funds in making this project possible.

To my wife Beauty, my children Saona and Joshua I say thank you for your patience with me as I worked on the thesis.

I love thee, O Lord, my strength

The Lord is my rock, and my

Fortress, and my deliverer,

My God, my rock, in whom I take refuge,

My shield, and the horn of my salvation,

My stronghold, because

He made my feet like hinds' feet

And set me secure on the heights.

He trains my hands for war,

So that my arms can bend a bow of bronze.

Thou hast given me the shield of thy salvation

And thy right hand supported me,

And thy help made me great

Thou didst give a wide place for my steps under me

And my feet did not slip

PREFACE

The work described in this thesis was carried out by the author in the Department of Mechanical Engineering, Concordia University and the Department of Mining and Metallurgy, McGill University between August 1992 and May 1996, under the supervision of Dr. H.J. McQueen. No part of this thesis has been previously submitted at this or any other university. The data used in this research if they are from other research work has been duly acknowledged in the text. A list of references is included at the end of this thesis. Parts of this work have been presented at the 32rd, 33rd and 35th Annual Canadian Institute of Mining and Metallurgy conferences, in Quebec City, Toronto and Montreal, in 1993, 1994 and 1996 respectively.

TABLE OF CONTENTS

LIST OF FIGURES

LIST OF TABLES

LIST OF SYMBOLS

A:	Material Constant [s^{-1}]
L_o:	Specimen Gage Length [mm]
m:	Strain Rate Sensitivity Exponent
N:	Number of Turns
n:	Stress Exponent
n'':	Strain Hardening Exponent
Q_C:	Activation Energy for Creep [kJ/mol]
Q_{HW}:	Activation Energy for Hot Working [kJ/mol]
R:	Universal Gas Constant [8.314 J/mol-K]
r:	Specimen Gage Radius [mm]
Z:	Zener-Hollomon Parameter [s^{-1}]
α:	Stress Multiplier [MPa^{-1}]
γ:	Torsional Strain
ε:	Equivalent Strain
$\dot{\varepsilon}$:	Strain Rate [s^{-1}]
ε_f:	fracture strain
σ:	Equivalent Flow Stress [MPa]
σ_p:	Peak Flow Stress [MPa]
τ:	Shear Stress [MPa]
FS:	Fractional Softening

GB	Grain Boundary
PSN	Particle Stimulated Nucleation
SG	Subgrain
SGB	Subgrain Boundary
TEM	Transmission Electron Microscopy
DRX	Dynamic Recrystallization
DRV	Dynamic Recovery
SFE:	Stacking fault energy
SRX:	Static recrystallization
SRV:	Static recovery
T:	Temperature
T_m:	Melting temperature
T_i:	Holding time
Γ:	Torque
θ:	Angle of twist per unit length
π:	3.1416
ε_0:	Initial Instantaneous Strain
ε_c:	Critical Strain
ε_1:	Strain at the end of Stage 1

Research Objectives

1) To conduct torsional testing on Magnesium alloys AZ31-Mn, AZ91, AZ31, ZK60 and AZ63, thus determining the dependence of strength and ductility on temperature in the range 180-450°C and strain rate 0.01-5.0 s^{-1}.
2) To establish a data base and constitutive equations for modeling of mechanical forming processes, notably extrusion, forging and rolling.
3) To examine the specimens by optical microscopy to determine the mechanisms of deformation for the purpose of explaining the dependence of strength and ductility on temperature and strain rate.
4) To predict the effect of the worked microstructures on product properties.

1. INTRODUCTION

Magnesium alloys, in recent years, have seen considerable growth in automotive applications as a result of their high isotropic modulus at strength-to-weight ratios comparable to polymer matrix composites [1-5]. Magnesium and its alloys are attractive for many engineering structural and non-structural applications not only because of high strength-to-weight ratios in both the cast and wrought forms, but because they exhibit good machinability, weldability and hot formability. The addition of Mn has led to improvement in corrosion resistance, a factor that is of considerable significance [4-8]. The resurgence has been primarily in die cast products because of the superb shaping capability and productivity. On the other hand, the use of wrought products has grown slowly since the 1950's when they became non-competitive for aeroplane structures [1].

The strain hardening from interactions of dislocations, whose glide and multiplication are the main mechanisms of plastic flow, is alleviated at high temperatures by dynamic recovery (DRV). The reduction in the dislocation density through climb, cross-slip and annihilation results in subgrains which are larger and more perfect as T rises and strain rate $\dot{\varepsilon}$ declines. In Al alloys and ferritic steels, DRV occurs to a high level so that the flow curves rise monotonically to a steady state regime in which the substructure density remains constant [9-18]. In austenitic steels and Ni base alloys, DRV is much lower so that at a critical strain ε_c, dynamic recrystallization (DRX) initiates leading to a flow curve peak (ε_c, σ_p) followed by flow softening to a steady state regime [9,12,13,17,19-21]. In Mg, the level of

DRV is sufficiently low that DRX ensues above 240°C ($0.4T_m$) giving rise to new fine grains at the grain boundary (GB) of the initial grain which relieves stress concentrations at triple junction due to GB sliding [11-13, 22]. The hot ductility is enhanced by DRV, which relieves stress concentrations at triple junctions due to grain boundary sliding, and by occurrence of DRX which separates GB from fissures, inhibiting their propagation. The hot work substructures are able to induce static recovery SRV or recrystallization SRX after deformation either between stages or during final slow cooling [10]. The substructures from DRV or the refined grains from DRX or SRX may be utilized in thermomechanical processing TMP to strengthen the product [15]. Of course, GB sliding occurs in the hot working range and initiates failure in course grained alloys [10-13]. However, due to enhanced GB sliding, fine grained alloys with suitable second phase stabilizers undergo superplastic deformation which is fairly common in (α + β) Ti alloys [12,13,15,16].

Magnesium wrought products have been used in areas where their light weight is of prime importance. Wrought magnesium has been widely utilised in transportation, handling equipment and sports equipment. Examples include tools for handling concrete, utility carts, tennis rackets, ladders and truck bodies. Wrought magnesium alloys are produced as bars, billets and shapes, wire, sheet and plate, forgings and tubing, with moderate mechanical properties [22-29]. In the period between the two world wars difficulties were encountered with magnesium alloy castings because they tended to have large variable grain size that often resulted in poor mechanical properties and excessive directionality in wrought components [23-32]. In 1937 it was discovered that zirconium had an intense grain refining effect on magnesium. Paradoxically, zirconium could not be used in the existing commercial alloys because it was removed from solution by the formation of stable compounds with both aluminum and manganese. This led to the evolution of a

complete new series of cast and wrought zirconium-containing alloys having much improved mechanical properties at both room and elevated temperatures [6,23]

Magnesium alloys like other metals with hexagonal crystal structures, are much more workable at elevated temperatures than at room temperature. Magnesium parts are usually drawn at elevated temperature in one operation without repeated annealing and redrawing, thus reducing the time involved for making the part and eliminating the necessity of additional die equipment for extra stages [31]. Hot-formed parts can be made to closer dimensional tolerances than cold-formed parts because of less springback [1,3,23]. On expectation of a resurgence in mechanical shaping, a program on hot workability of Mg alloys was launched by publication of a review [1] which drew on experience in Al alloys, ferritic and austenitic steels.

2: DEFORMATION MECHANISMS IN HCP METALS

2.1.1 Plastic Deformation by Slip

Macroscopically, slip may be defined as the irreversible shear of part of a crystal with respect to another without the breaking of a large number of interatomic bonds (fracture) or changing crystallographic orientation (twinning)[33,34]. If dislocation movement is assumed to cause all slip, one can deduce that the shortest slip vector which preserves the ABAB basal, close-packed plane stacking (Fig 2.1) is of magnitude a and direction $\langle 11\bar{2}0 \rangle$ (Figure 2.2). The total strain energy is lowered by the dislocation dissociation in the basal plane into two partial dislocations having the slip vector $a/3$ $\langle 10\bar{1}0 \rangle$ [35], producing a stacking fault in a narrow ribbon between the two partials. As a result of the balance between the decrease of energy in the dislocation strain field, which results from dissociation, and the surface energy of the fault ribbon dependent on γ estimated to be in the range 0.20-0.40 J/m^2 [30], the separation of the partials at room temperature would be of the order of an interatomic distance. The stabilization of dislocation lines in the basal plane due to dissociation into partials is a real but marginal effect so that with increasing temperature, thermal activation of dislocation constriction would allow escape of dislocations from the basal plane to give wavy lines [36]. At low T straight lines of slip on the basal plane are easily observable on previously polished surfaces of magnesium but they are more difficult to identify for purer magnesium and higher temperature of deformation.

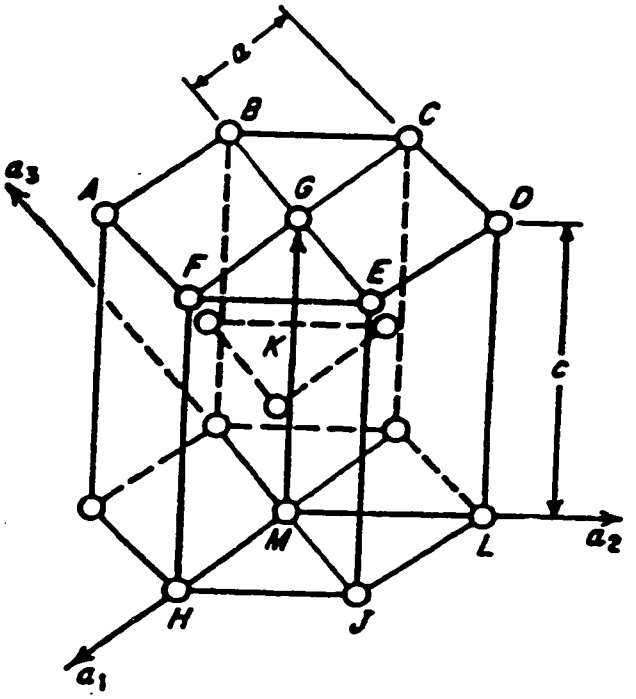

Basal plane (0001) *ABCDEF*

Prism plane $(10\bar{1}0)$ *FEJH*

Pyramid planes

Type I, Order 1 $(10\bar{1}1)$ -*GHJ*

Type I, Order 2 $(10\bar{1}2)$ -*KJH*

Type II, Order 1 $(11\bar{2}1)$ -*GHL*

Type II, Order 2 $(11\bar{2}2)$ -*KHL*

Diagonal axis $[11\bar{2}0]$ *FGC*

Figure 2.1: Magnesium hexagonal close-packed structure showing the basal, prism and pyramidal planes.[1]

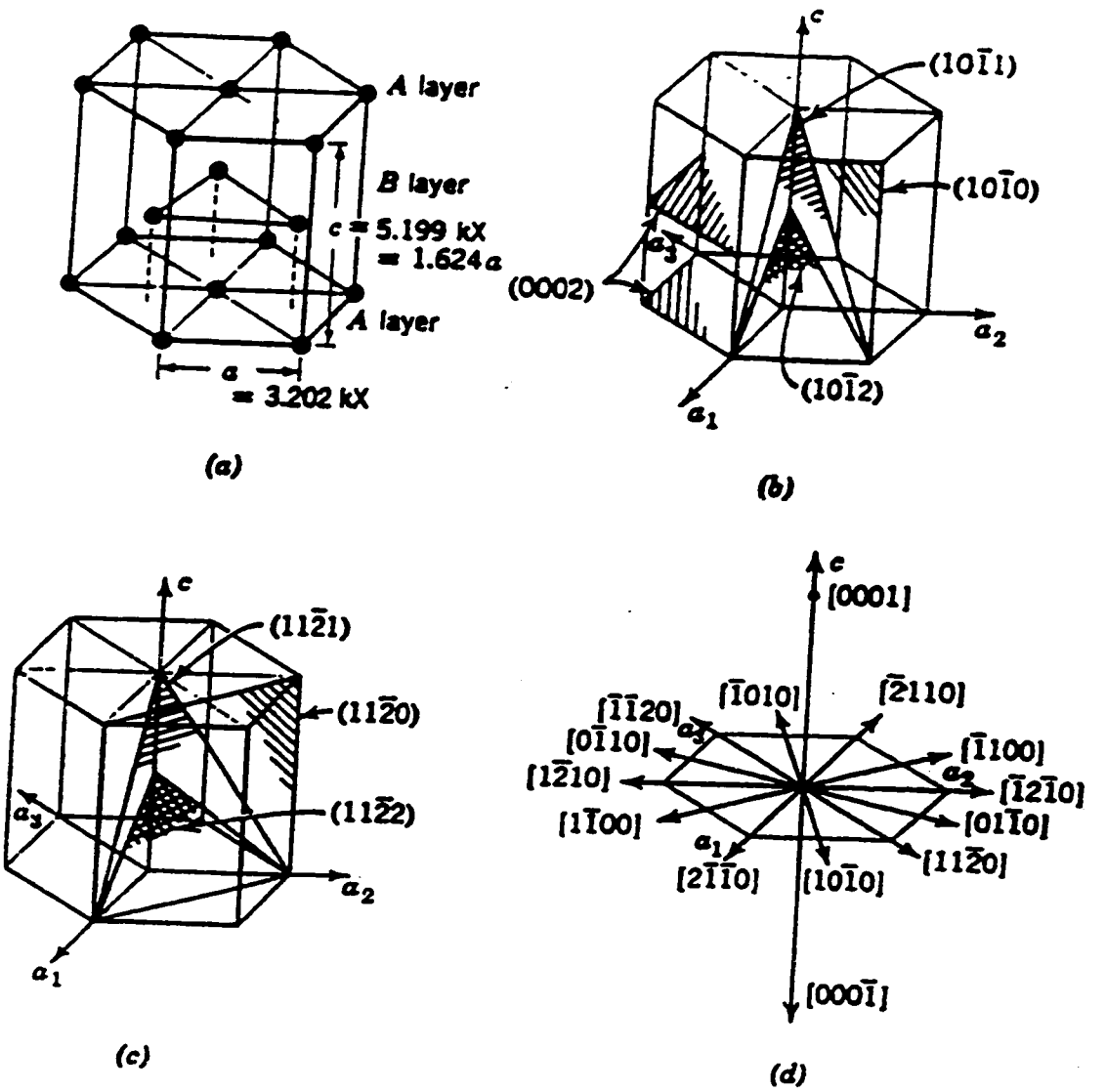

Figure 2.2: The magnesium crystal. (a) Atomic positions; (b) principal planes of the $[1\bar{2}10]$ zone; (c) principal planes of the $[1\bar{1}00]$ zone; (d) principal directions[4].

In metallic crystals there have only been limited evidence of slip which is not in the most closely packed direction in the crystal. Such slip is of negligible importance in cubic metals since their crystal symmetry allows several noncoplanar slip directions. Since all the close-packed or $\langle 11\bar{2}0 \rangle$ directions in magnesium lie in the basal plane of the crystal, plastic deformation by multiple slip in polycrystalline magnesium is not possible, in principle. Considerable plasticity is observed because several other mechanisms supplement that of simple slip including non-basal slip, twinning, and grain boundary deformation [36-38]. For many years there was evidence of slip on prismatic planes such as $\{10\bar{1}0$ and on pyramidal planes such as $\{10\bar{1}1$ only at temperatures above 225°C. However, more detailed examination in recent years has shown that as constraints increase either when shear stress in the basal plane is very low or near grain boundaries in polycrystals, slip on prismatic and pyramidal planes takes place. It is clear that as T increases notably above 225°C slip on non-basal planes becomes more frequent [39-41].

Taylor [42,43] noted that in random polycrystals, grains must deform in the same manner as the object as a whole. This requires 5 slip systems and 24 orientations, covering all directions in each grain. Dislocations cannot glide from one grain to another because of misalignment of the slip planes [44]. Pile-ups occur near the GB (slip steps at surface fade near GB). The pile-ups cause stress concentration in the next grain, so may activate additional local slip systems. Stated in another way, grains must remain welded to each other, so they exert constraint on each other because they slip in different directions. The additional local strain produces 'geometrically necessary dislocations', along GBs. These form tangles and subgrains earlier than centres of grains. Cell formation has been observed in polycrystalline magnesium and magnesium alloys notably near grain boundaries. Only in

part is such cell formation the result of the simple aggregation of basal slip dislocations into arrays by glide and climb.

2.1 2.Plastic Deformation by Twinning

Magnesium twins mechanically on $\{10\bar{1}2\}$,$\{30\bar{3}4\}$,$\{10\bar{1}3\}$, $\{11\bar{2}4\}$, and perhaps on $\{10\bar{1}1\}$, $\{10\bar{1}4\}$, $\{10\bar{1}5\}$, and $\{11\bar{2}1\}$.[9,10] The importance of $\{10\bar{1}2\}$ twinning in deformation of the metal was realized early since it was detected by the "crackling" sounds when a single crystal or recrystallized bar of polycrystalline pure magnesium is bent. The boundaries of lenticular $\{10\bar{1}2\}$ twins are easily etched in metallographic sectioning, which also shows second-order twins and $\{10\bar{1}2\}$ twin intersections of several types. After roller leveling (straightening between rolls) of sheets of magnesium which have basal planes in the plane of the sheet are shorter and thicker due to twinning $\{10\bar{1}2\}$. The reason for these dimensional changes is apparent in Figure 2.3, which shows the shear strain (0.131) and one possible direction, $[\bar{1}011]$of the family $\langle 10\bar{1}1\rangle$, for $\{10\bar{1}2\}$ twinning in magnesium. When the atoms above the twinning plane move into the mirror positions across it with respect to those below it, an over-all increase in length occurs in the *c* direction and a decrease occurs in the *a* direction. This is a simple geometrical result of the angle between $\{10\bar{1}2\}$ and (0001), 43° 9', being less than 45°.

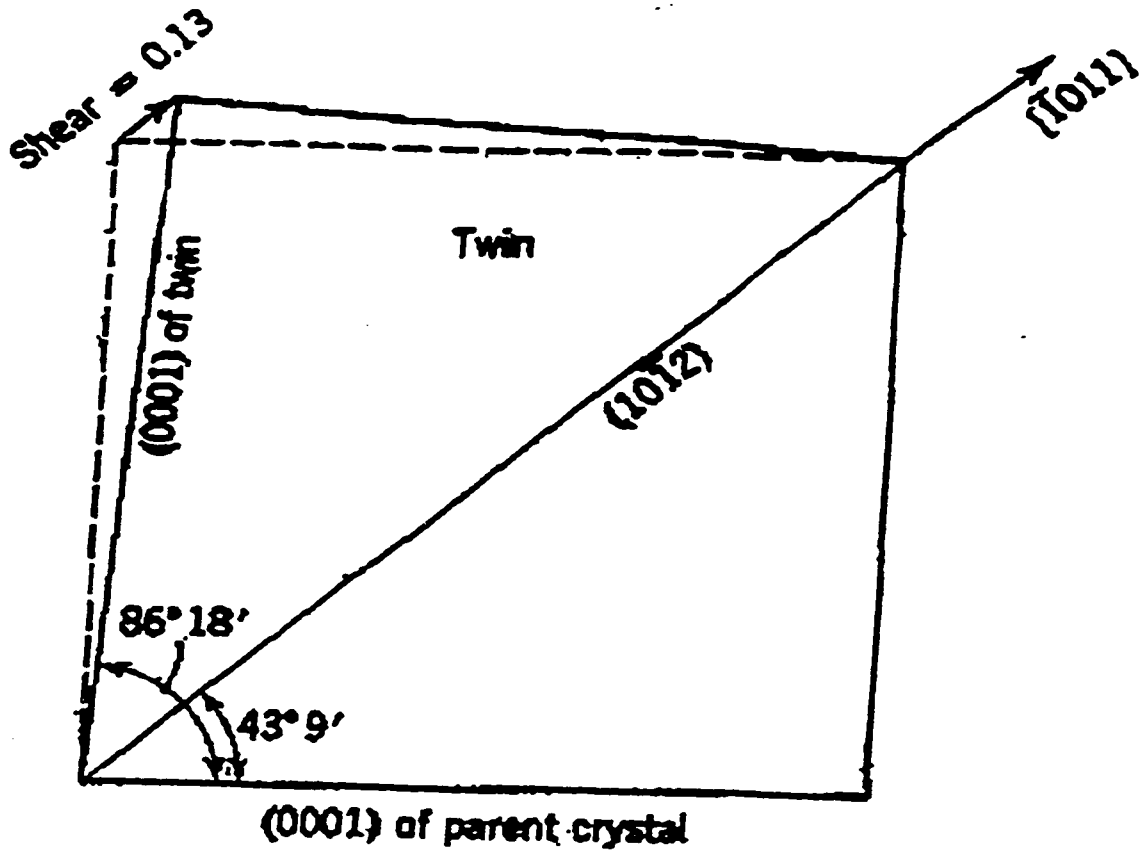

Figure 2.3: $\{10\bar{1}2\}$ twinning in magnesium[4].

It can be said that $\{10\bar{1}2\}$ twinning is favored by compression parallel to the basal plane and tension perpendicular to it [45,46]. After hot rolling or cold-rolling plus annealing, recrystallized magnesium alloy sheet is composed of grains more or less near to the "ideal" orientation, with the *c* axis perpendicular to the surface. The thickening of sheet after bending operations can be explained here by applying the single-crystal orientation criterion to the "ideal" texture. However the single-crystal orientation criterion is not very reliably applied to individual grains in an aggregate subject to known macroscopic stresses. In cases where twinning has been found to occur in opposition to overall macrostresses, it contributes a strain, which is negative to the over-all plastic strain [47]. The complete formation of a twin is possible under the simple condition where the parent crystal has no restraint. In practice, accommodation to the shear is accomplished by the phenomenon of kinking with bend or kink planes on both $\{10\bar{1}0\}$ and $\{11\bar{2}0\}$ planes, as has been observed in magnesium.

2.2 Creep

Metals undergoing continuous deformation at elevated T under constant load are said to creep. Under a wide range of conditions, the creep rate declines to a constant value as a result of attaining a balance between hardening and dynamic recovery [48,49]. A creep curve of strain versus time for constant load in Figure 2.4 (a) illustrates the stages observed in

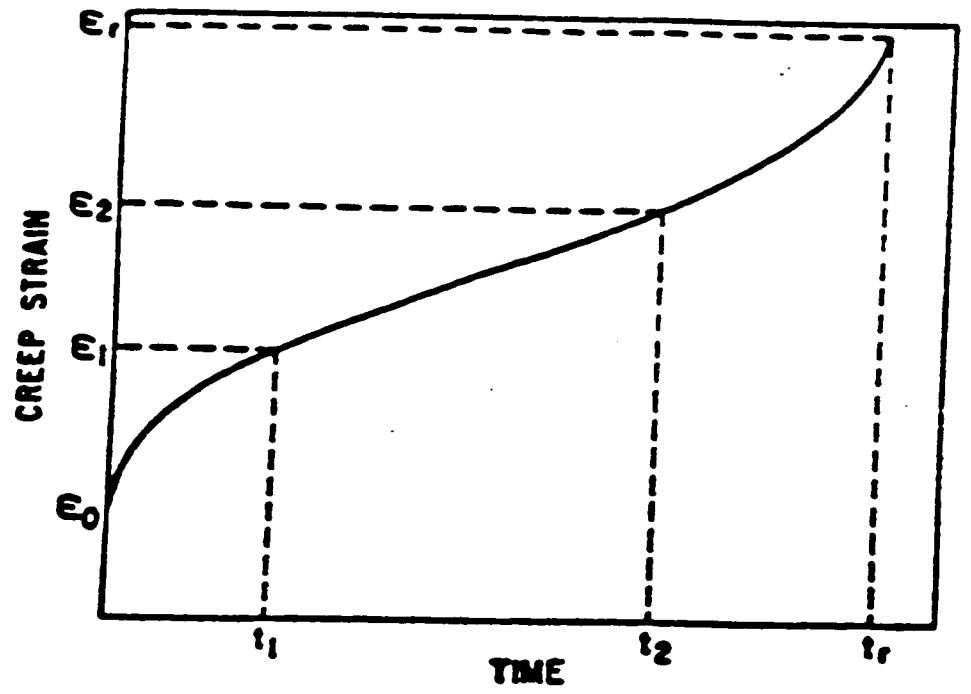

Figure 2.4(a) Schematic representation of a creep-rupture curve (Garofalo) [45].

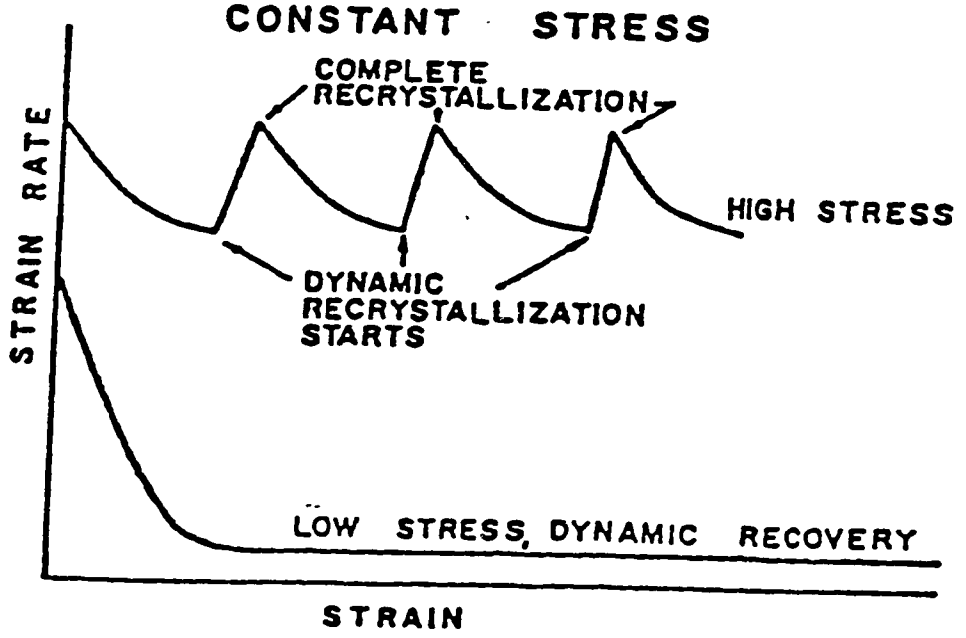

Figure 2.4(b): Dynamic recrystallization during creep at high stress and temperature (upper curve) and dynamic recovery during creep at low stresses (lower curve) [9,42].

metal which restores by dynamic recovery only. The first stage up to ε_1, which is characterized by a continuous decrease of the creep rate, is called primary or transient creep and corresponds to the strain hardening part of the flow curve [49]. The portion between ε_1 and ε_2 where the creep rate remains constant, called secondary or steady state creep, is identified with the third part of the flow curve where stress, strain rate and temperature remain constant. The stage between ε_2 and ε_r with creep rate increasing steadily is called tertiary creep. The equivalent section in the flow curve at constant strain rate is not usually clearly defined, although the fracture mechanisms are similar.

When dynamic recrystallization takes place, the creep curve exhibits alternating cycles of normal and accelerated creep. This is illustrated in Figure 2.4(b). After a normal stage of primary creep, the strain rate accelerates, indicating that dynamic recrystallization is occurring. At low stresses, there is insufficient build-up in dislocation density to nucleate dynamic recrystallization, so that creep proceeds due only to dynamic recovery [49].

It has now been recognized that the creep behavior of metallic solid solution alloys divides into two distinct classes [50-52]. The first type, termed as class M (metal type) [54], has characteristics which are similar to pure metals, including a stress component close to 5, a normal primary stage of creep, and the formation of an internal subgrain structure. The second type, termed class A (alloy type) [18,47,50,53], behaves differently to pure metals, with a stress exponent close to 3, either an almost instantaneous steady-state behavior or a very brief normal or inverted primary stage, and the formation of a substructure consisting initially of a uniform distribution of dislocations. Class M behavior is generally attributed to a recovery process involving dislocation climb, whereas class A behavior is attributed to a viscous drag process in which the glide of dislocations is restricted

due to the presence of solute atom atmospheres. Although these two types of behavior are well supported by experimental results on several face centered cubic (FCC) solid solution alloys, a lack of detailed creep data has so far prevented a similar approach in other crystal systems.

2.2.1.Creep Behavior of Magnesium

Investigations of creep mechanisms in polycrystalline Mg [54-60] revealed three different mechanisms, with the creep process depending on the testing T and stress level. In the low T range, up to 300°C, the activation energy for creep is equal to ~135 ± 10 kJ/mole, there is normal primary and secondary creep, the stress exponent is close to 5.2 with extensive basal slip. This behavior is consistent with control by dislocation climb. At intermediate T, 300- 450°C, the activation energy is about 140 ± 10 kJ/mole; at low stresses in alloys, solute drag is evident with a stress exponent of 3. However, at stresses above 2.5 MPa there is primary and secondary creep, the stress exponent is close to 6.0 and the substructure consists of subgrains arising from basal slip and dislocation climb. At high stresses and temperatures, the activation energy rises to about 230 ± 10 kJ/mole in association with extensive non-basal slip; this behavior is consistent with the cross-slip of dislocations from basal to pyramidal planes [39-41]. At high T, above 450°C, and low stresses below 2.5 MPa, the activation energy is equal to ~135 ± 10 kJ/mole, there is little or

no primary creep, the stress exponent is close to 1.0 and there is an absence of visible slip lines. This behavior is attributed to lattice diffusion [38-40].

3. HOT WORKING CHARACTERISTICS

3.1 Restoration Mechanisms on Hot Working

Hot working is considered to be deformation at a temperature above 0.5 T_m (melting temperature, K) and strain rate between 10^{-3} to 10^{3} s^{-1} The strains may vary from 0.1 to as high as 50. At these temperatures, most metals have low flow stress and high ductility. Both dynamic and static softening mechanisms take place during the hot working process which includes the preheating, deformation and subsequent cooling. Hot working is employed because metals can be subjected to large and rapid changes in shape without cracking. The perennial need for improved processes and products generates continued and growing interest in high temperature deformation [62-64].

Hot deformation of any metal will cause an increase in dislocation density within the grains, which serves to strain harden the material and ultimately leads to fracture if some form of restoration mechanism is not active to alleviate stress concentrations. Since hot working is generally performed in several steps, the restoration processes can be divided into two main groups: those occurring during deformation are called dynamic and those taking place in the absence of stress or strain on the material are termed static. In any deformation process, one or all of the following restoration mechanisms may be active:

(i) Dynamic Recovery (DRV)

(ii) Dynamic Recrystallization (DRX)

(iii) Static Recovery (SRV)

(iv) Static Recrystallization (SRX)

Their initiation and control is dependent on both material properties and on the selection of such parameters as temperature, strain, strain rate and time [62-64]. The major material factor that determines whether recovery or recrystallization will take place during hot working at a specific condition is the stacking fault energy (SFE). For high SFE metals, only DRV is observed. However, for metals of moderate or low SFE, DRX takes place above a critical strain [9,14,17,18,19,20,21,65].

3.2.Dynamic Recovery (DRV)

Dynamic recovery (DRV) is the basic mechanism that leads to the annihilation of pairs of dislocations during deformation. As shown in Figure 3.1 a simple flow curve, increasing strain hardening to a steady state plateau, is characteristic of pure DRV. The flow curve exhibits three distinct stages. During the first, the elastic strain is increasing from zero to the yield stress. Strain hardening takes place during the second stage; however, the slope of the curve continually decreases as the rate of work hardening diminishes. The amount of work hardening and the strain to the end of this stage decreases as the temperature is raised and the strain rate lowered. In the third stage, the work hardening rate has reached zero and the flow stress has levelled off at an equilibrium steady state value. Therefore, in hot working, the temperature, the strain rate and the flow stress are constant in the steady state regime. In practice, the flow curve may decrease after the plateau

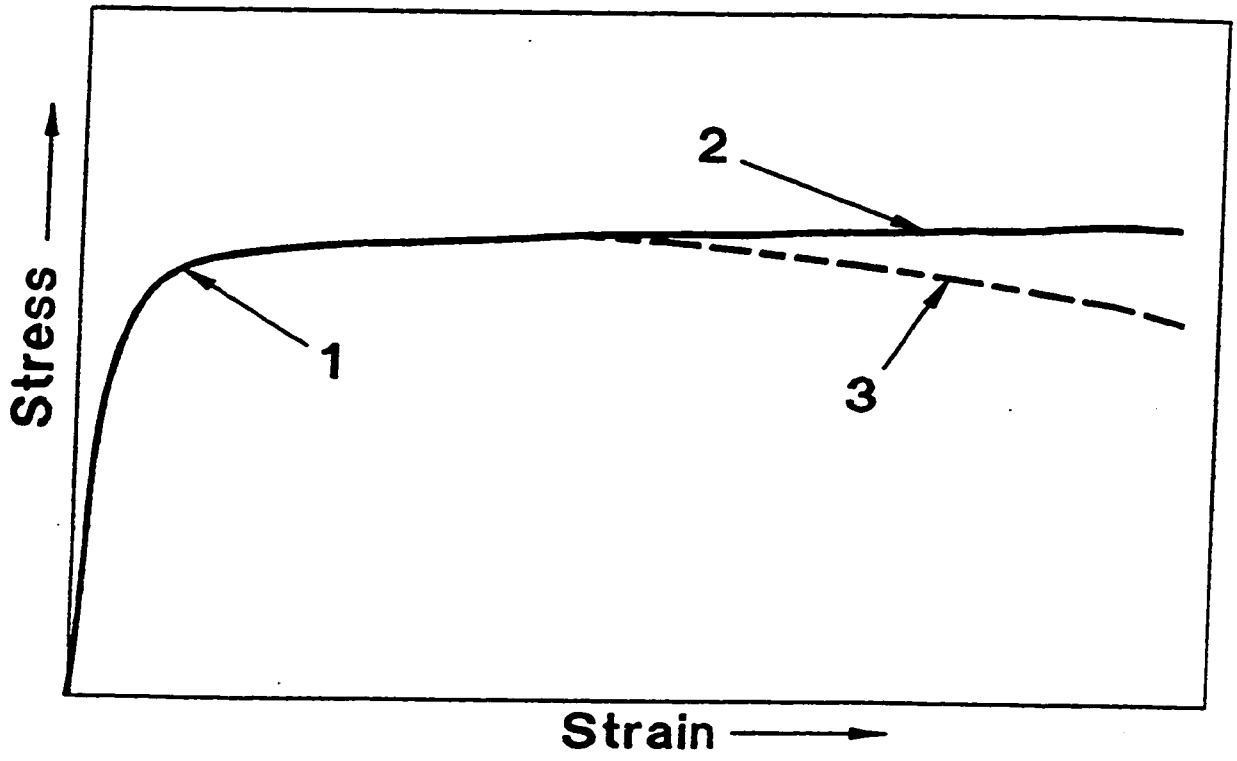

Figure 3.1 Typical dynamic recovery flow curve: after an initial strain hardening phase (1), there is a region of steady state deformation without strain hardening (2). In practice, the flow curve may decrease as the result of deformation heating or precipitate coalescence (3) [64].

has been reached as the result of other factors such as deformation heating or precipitate coarsening [9,14,16,17,19,63,64,66].

During the initial loading stage of the flow curve, some dislocation multiplication takes place, increasing slightly the dislocation density. In the strain hardening stage, the dislocations increase greatly and become entangled into a substructure within the grains. As deformation continues in metals with high SFE, the sub-boundaries increase in number and dislocation density and rearrangements by DRV also rise until a dynamic equilibrium is reached between dislocation generation and annihilation. At this point where the subgrains reach the equilibrium size, a steady state is established in which the flow stress remains constant. While the grains are deforming in correspondence with the external shape, the subgrains remain equiaxed even after large strains, indicating that the individual sub-boundaries are being decomposed and reformed. This dynamic regeneration [54] termed repolygonization explains the absence of any distorted subgrains even after very large strains. The subgrains become larger in size as the deformation temperature is increased or as the strain rate is decreased. Such larger subgrains and their boundaries, both contain less dislocations [9,14,18,63-67].

3.3 Dynamic Recrystallization (DRX)

The typical flow curve of a material undergoing DRX is shown in Figure 3.2. Several distinguishing characteristics of the Figure 3.2 are:

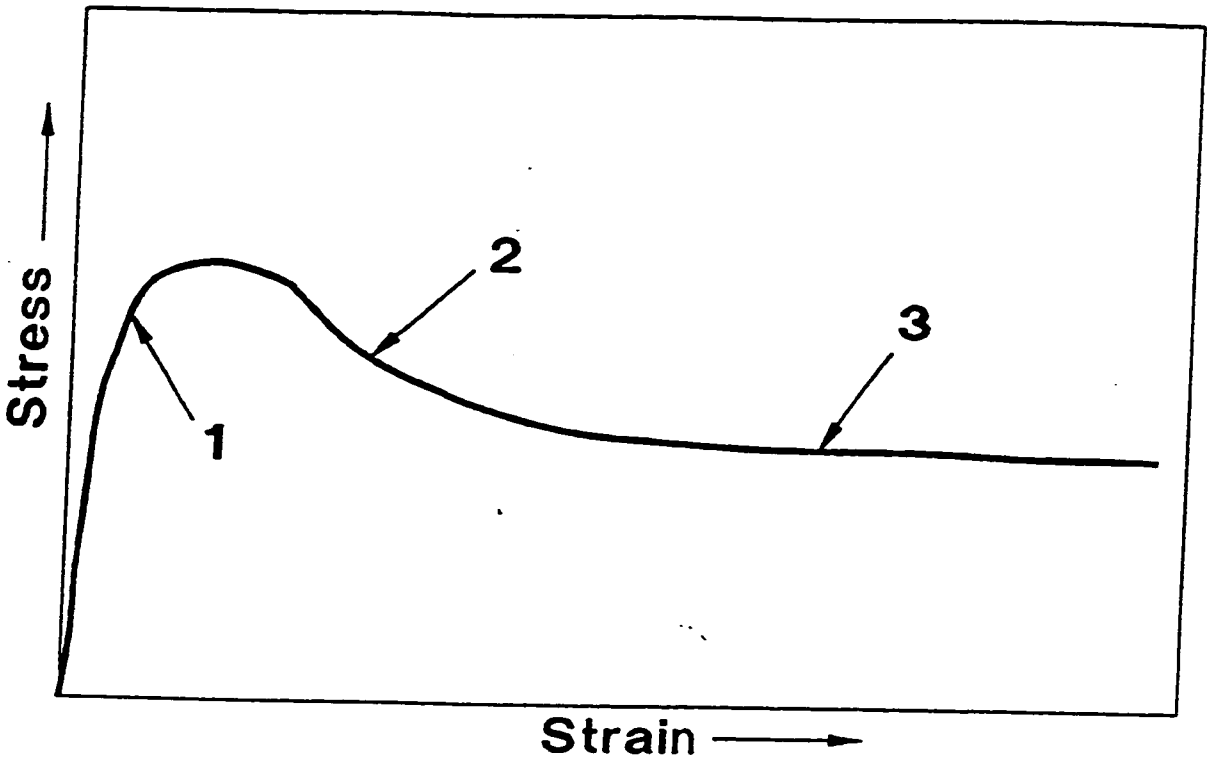

Figure 3.2 Typical dynamic recrystallization flow curve: the accumulation of dislocations is sufficiently great that recrystallization is nucleated during deformation (1). Since the recrystallized grains have a lower density of dislocations (2) than the unrecrystallized material (1), there is work softening. These recrystallized grains are continually reworked and repeatedly recrystallized giving the steady state flow stress (3) [64].

(i) The initiation of recrystallization after a critical strain denoted by a decrease in work hardening rate to a distinct peak in the flow curve.

(ii) A flow softening due to the growth of DRX grains which are also being deformed.

(iii) The flow stress levelling off at a steady state value due to the combination of strain hardening, DRV in the new grains and repeated uniformly distributed DRX nucleation.

At higher strain rates, DRX [9,19-21] is continuous after giving rise to a single peak stress value and produces grain refinement. However, at lower strain rates, the mechanism is periodic with each stress-decreasing recrystallization wave followed by a degree of work hardening. The result is a cyclic pattern of decreasing amplitude and grain coarsening [9,14,17,19-21,63-65,69].

DRX is generally observed in metals with low SFE whereas in metals with high SFE, it seldom occurs because DRV produces a low dislocation density. When the dislocation density builds up to a critical level, it is the critical strain at which DRX occurs. At lower strain rates nucleation possibly occurs by the bulging of existing grain boundaries. Migrating grain boundaries leave behind dislocation-free regions in which the dislocation density once again increases as strain proceeds until recrystallization is again nucleated. At high strain rates, a fine and dense tangled cellular structure is developed throughout the grains but more strongly at the grain boundaries and deformation bands. Nuclei develop initially along grain boundaries where there are high misorientations between the subgrains. The dislocation densities at the center of the new grains increase sufficiently that nucleation

occurs again before any wave of recrystallization is complete. As a result, there is a distribution of dislocation substructures which maintains the average flow stress at a steady state between the yield stress of statically recrystallized material and the peak stress [9,14,17,19-21,63-65,69].

3.4 Dynamic Recrystallization of Magnesium

It is generally agreed that dynamic recrystallization occurs most readily in those materials where dynamic recovery is slow, e.g. in materials of medium or low stacking fault energy such as copper, nickel and austenitic steels. A review by Sellars [9,14,19,21,69] and others revealed little or no evidence for dynamic recrystallization in aluminium or ferritic steels with the exception of high purity α-iron [71]. The reported values of stacking fault energy in magnesium are high [30], similar to those of aluminium [64] and therefore in terms of this parameter and its effect on recovery, magnesium might be expected to soften by dynamic recovery, rather than recrystallization. However, a review of literature [11-14,22,34,35,72,73] indicates that dynamic recrystallization is indeed important during the high temperature deformation of magnesium, and this is ascribed to the constraints imposed by the lack of easily activated slip systems rather than to the effect of stacking fault energy. Figure 3.3 shows data for the critical resolved shear stress of various slip systems in pure magnesium. It can be seen that at temperatures below ~ 327°C, basal slip, $(0001)\langle 11\bar{2}0\rangle$ is much the easiest, however, this provides only three independent slip systems [45, 72].

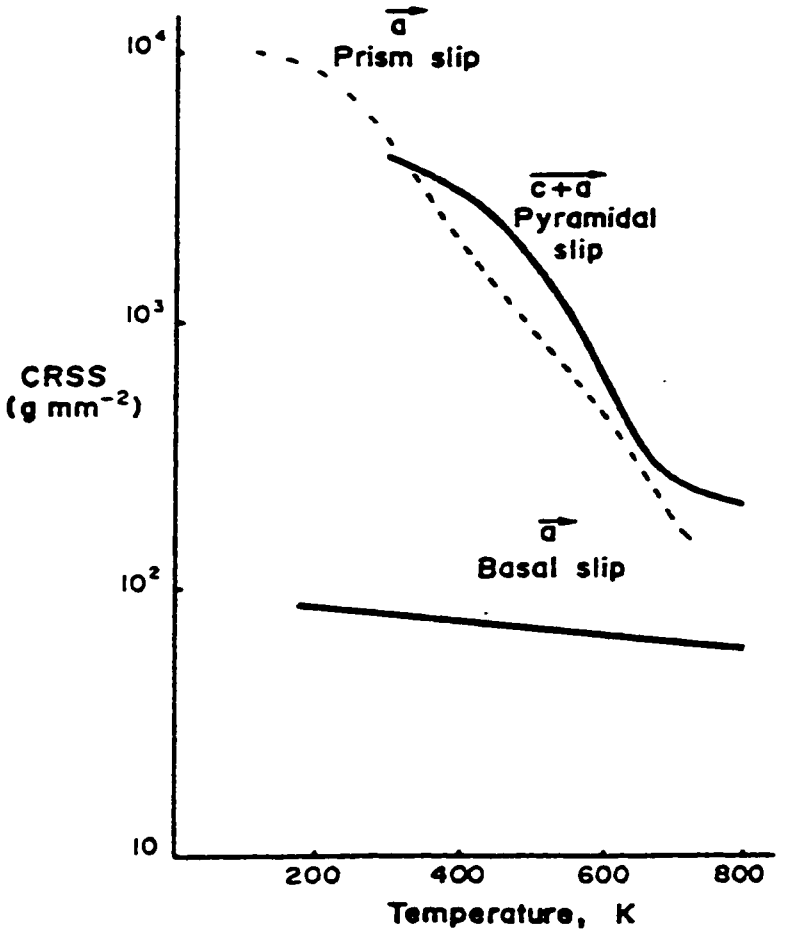

Figure 3.3 The Critical Resolved Shear Stress (CRSS) for various slip systems in pure magnesium [39].

In the paper by S. E. Ion, F.J. Humphries and S.H. White [39] it was observed that during the deformation at room temperature, some very localized shearing occurs at grain boundaries, although this is often associated with intergranular fracture [39,76]. Their observations show that the region of distortion good in the vicinity of the grain boundary is associated with the operation of nonbasal slip systems and dislocations of *c* + *a* Burgers vector, and that as the temperature of deformation is increased and the critically resolved shear stress (CRSS) for such slip decreases markedly, (Figure 3.3) the width of the rotated 'mantle' region increases. In the temperature range 152-327°C, a significant amount of plastic strain is acccommodated in the mantle regions, the cores of the grains being relatively undeformed. At temperatures above ~327°C, the CRSS for the non basal slip systems has decreased to such an extent that the mantles extend throughout the grains and microscopically homogeneous deformation occurs with the operation of the five independent slip systems required by Taylor[42].

In the temperature range 152-327°C, it is postulated that significant subgrain rotations, from deformation and dynamic recovery processes, within the severely distorted boundary regions lead to the formation of high angle grain boundaries and therefore of recognisable new grains without further significant changes in orientation. However, at high $\dot{\varepsilon}$ nucleation is related to formation of high angle misorientation cells at the boundary [76]. The work by Humphries and others [22,75] showed that magnesium does not dynamically recrystallize in this way. The optical, TEM and X-ray evidence suggests that the siting, size and orientation of the new grains is consistent with their formation from severely rotated regions adjacent to the grain boundaries [22,75].

3.5 Static Recovery (SRV) and Static Recrystallization (SRX)

At the end of a high temperature deformation, there is a dislocation substructure with an associated stored energy which is capable of driving static restoration mechanisms such as SRV and SRX [10,14,17-19,63,65,66,68].

SRV is the annihilation and rearrangement of dislocations in the sub-boundaries followed by growth of the subgrains. This process is the sole mechanism of softening if the critical stored energy is not surpassed and always occurs during the incubation period before the appearance of recrystallization nuclei. As the stored energy increases, the incubation period for SRX decreases so that there is less opportunity for SRV. An increase in temperature or strain energy (higher ε or $\dot{\varepsilon}$) increases the rate of SRV while the addition of alloying elements decreases [10,14,17-19,63,65,66,68].

SRX is the elimination of dislocations as a result of the motion of high angle boundaries. SRX is preceded by an incubation period for nucleation, i.e. formation of regions with low dislocation density surrounded by mobile high angle boundaries. The new grains grow until all the deformed grains are replaced. A critical strain is required for SRX to take place; it rises as the temperature rises and the strain rate falls. At higher strains or strain rates, the driving forces are higher making the rate of recrystallization faster. Part of this results from the reduction of the subgrain size and increase in sub-boundary density so that there is a higher density of nucleation sites [10,14,17-19,63,65,66,68].

The effects of second phases are varied depending on their size and spacing. If they are small and numerous, they tend to stabilize the substructure, thus both limiting

SRV and preventing nucleation of recrystallization. Larger particles distributed along the grain boundaries, may prevent their migration and consequently recrystallization without altering recovery. However, large and rigid particles (>0.6 μm) which cause additional flow in the surrounding matrix, create nucleation sites for SRX [18, 67,68].

3.6 Interdependence of Stress, Strain Rate and Temperature

A number of mathematical expressions have been proposed to describe the relationship between flow stress (σ), strain rate ($\dot{\varepsilon}$) and temperature (T, Kelvin). In creep, the increase of $\dot{\varepsilon}$ in the steady state region as T rises and σ increases can be expressed by a power law and an Arrhenius relationship:

$$\dot{\varepsilon} = A_1 \sigma^{n'} \exp(-Q_c/RT) \qquad (3.1)$$

where A_1 : Empirical Constant

R : Universal Gas Constant (8.314 J/mol-K)

Q_c : Activation Energy for Creep

For aluminum, the relationship holds over eight orders of magnitude from 10^{-8} to 10^{2} s^{-1}. The value of Q_c is approximately equal to that for self diffusion indicating that the rate controlling mechanism is dependent on vacancy migration [63-68].

The interrelationship between the three parameters σ, $\dot{\varepsilon}$ and T can also be written in the hot working form and with different stress functions:

$$A_1 \sigma^{n'} = \dot{\varepsilon} \exp(Q_{Hw}/RT) = Z \qquad (3.2)$$

$$A_2 \exp(\beta\sigma) = \dot{\varepsilon} \exp(Q_{Hw}/RT) = Z \qquad (3.3)$$

$$A_3[\sinh(\alpha\sigma)]^n = \dot{\varepsilon} \exp(Q_{Hw}/RT) = Z \qquad (3.4)$$

where A_i, α, β, n, n' : Empirical Constants

Z : Zener-Hollomon Parameter

Q_{Hw} : Activation Energy for Hot Working

These equations hold for DRV or DRX but Q_{Hw} would be different for the two mechanisms. The power law (Equation 3.2) works satisfactorily for low stresses and the value of n is usually in the range of 4 to 5. The exponential law (Equation 3.3) is useful for high stresses and β (= $\alpha n'$) has values in the range of 1 to 1.5×10^{-3} MPa^{-1}. The hyperbolic sine law (Equation 3.4) covers the entire stress range (10^{-8} to 10^{2} s^{-1}) (Figure 3.4). The Z parameter is a temperature compensated strain rate which increases as T decreases. In hot working tests, Z is constant since T and $\dot{\varepsilon}$ are the controlled variables [68,78].

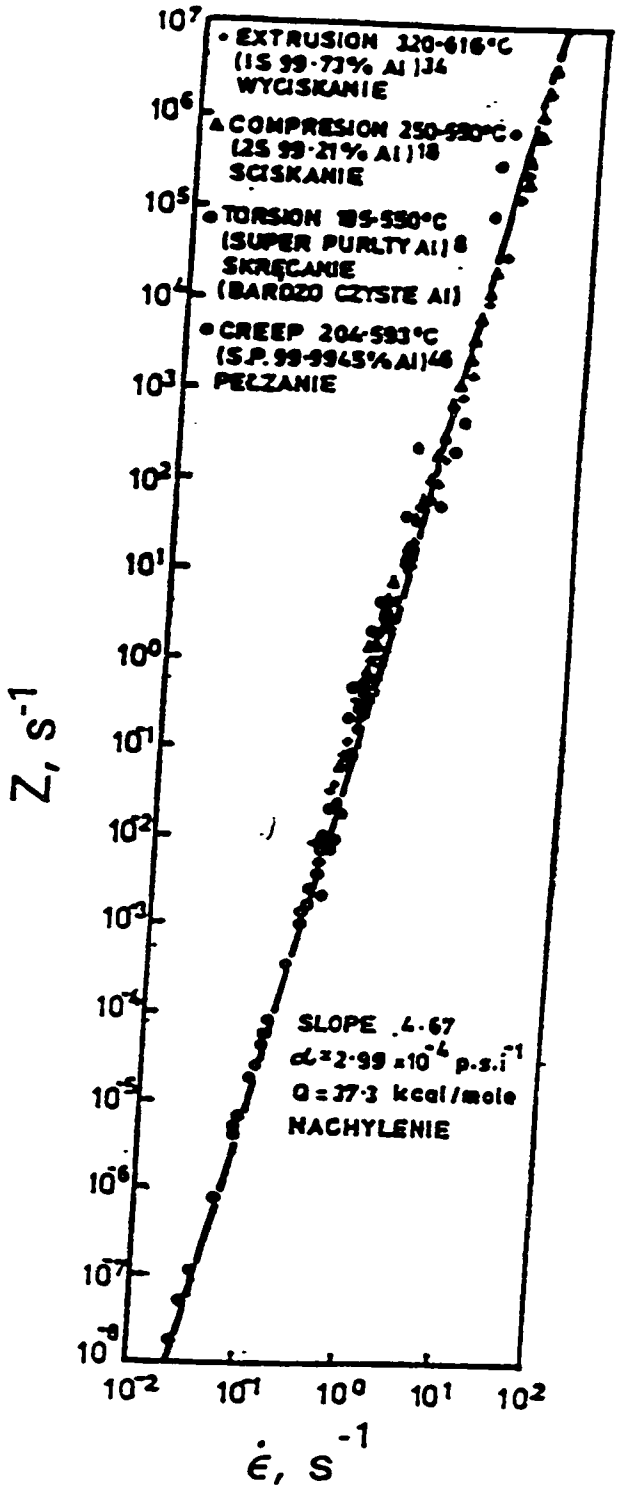

Figure 3.4 The application of Equation 3.4 to Aluminum over the strain rate range 10^{-2} to 10^{2} s^{-1} between 195 and 616°C [66].

4. EXPERIMENTAL PROCEDURE

4.1. Hot Torsion Testing

The strain and strain rate obtained during tensile testing are inadequate for industrial hot forming procedures. This mode of deformation suffers from necking instability which limits the uniform strain to a low value. The microstructure in the necked region is difficult to interpret because of the strain gradients. In compression testing there is no inherent instability. However, friction between specimen and anvil usually results in severe to slight barreling and in simulations limits the number of stages to two. The tension test is less useful than the compression and torsion test described below [79-81].

In recent years, hot torsion testing of solid cylindrical specimens has become more reliable in determining optimum hot working parameters such as strain, strain rate and temperature [79,82-87,88-91]. Although high strains can be achieved at a constant strain rate, there is a linear variation of strain and strain rate from zero at its center to maximum at the surface. If necessary, the effects of this variation can be reduced by use of a specimen with a tubular cross section. The major advantage of torsion over tension and compression testing is that there is no change in geometry of the specimen during deformation. In light of this fact, true strain and strain rate are equal to the engineering strain and strain rate in torsion.

Computer controlled torsion testing has come to be recognized as a powerful means of assessing material behavior at elevated temperatures, particularly under the conditions of high strain and relatively high strain rate. Therefore, industrial deformation processes, such at hot rolling and forging can be readily simulated.

Usually torsion testing data are recorded in the form of torque (Γ) versus angle of twist (θ) diagrams. Torsion testing data are usually recorded in the form of torque versus angle of twist diagrams. Torque is converted to maximum torsional surface shear stress (τ) by using the Fields Backofen equation [87,88]:

$$\tau = \Gamma(3 + m + n'') / 2\pi r^3 \qquad (4.1)$$

where Γ : Torsional Moment

m Strain Rate Sensitivity

n'' Strain Hardening Exponent

r Specimen Gauge Radius

Since all testing was conducted above 0.5 T_m, n" is generally taken as zero for the peak or steady state. However as T increases, m varies approximately from 0.01 to 0.2 for each of the materials tested. The variation of m with temperature has only a minor influence (< 10%) on the calculated stress because it is added to a larger factor in Equation (4.1).

Torsional strain is defined as the amount of relative rotation, by reference points on the surface of the specimen divided by the distance between them. Therefore, the torsional strain on the surface (γ) is [87]:

$$\gamma = 2\pi r N / L_o \qquad (4.2)$$

where N :Number of Turns

L_o :Original Gauge Length

In order to compare torsion data with tension and compression tests, the torsional shear stress and strains are converted to effective stresses and strains using the von Mises criterion for plastic yielding [87,88]:

$$\sigma = \sqrt{3}\tau \qquad (4.3)$$

$$\varepsilon = \gamma / \sqrt{3} \qquad (4.4)$$

where σ :Equivalent Flow Stress

ε :Equivalent Strain

4.2. Hot Torsion Machine

Testing was conducted on a computer-directed, servo-controlled, closed loop torsion machine designed as a joint project of Mechanical Engineering, Concordia University by Sandor Fulop et al. [88,90] and the Department of Mining and Metallurgy of McGill University (Figure 4.1). In this MTS electro-hydraulic system, torque is applied to a specimen through a rotary hydraulic actuator mounted on a converted lathe bed as schematically shown in Figure 4.2. The motor can develop a maximum torque of 100 N.m

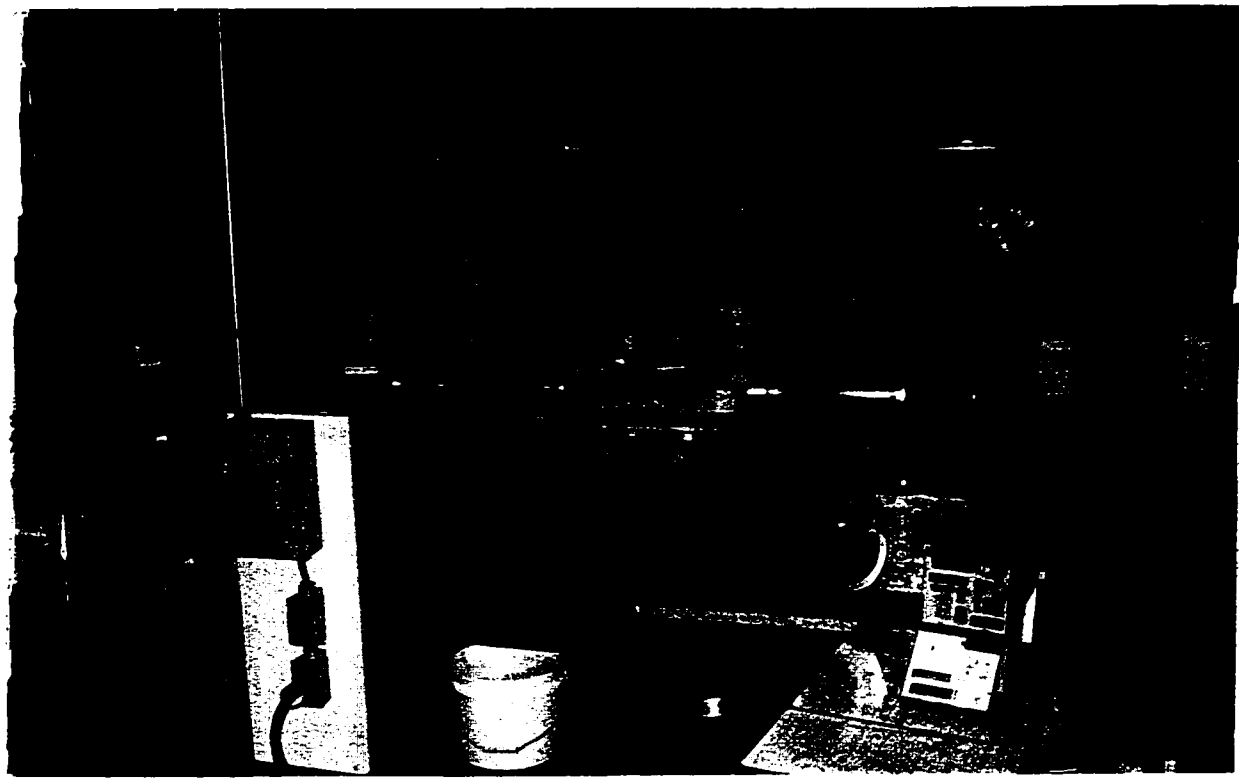

(a)

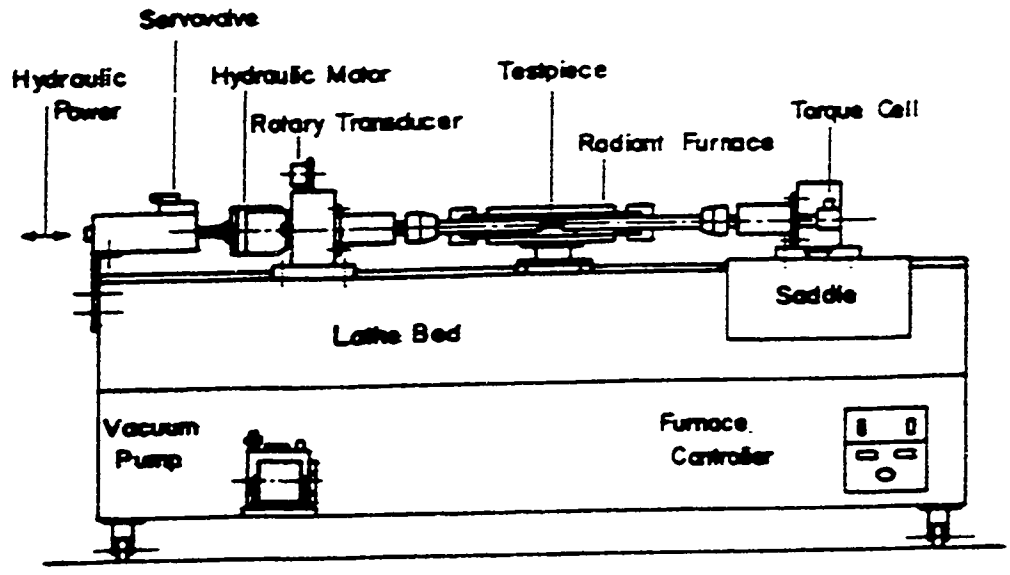

(b)

Figure 4.1 Servo-Controlled hot torsion machine: (a) photograph and (b) schematic[89].

and a maximum speed of 628 rpm. The speed and direction of rotation of the motor are controlled by a servo valve that proportions the hydraulic fluid flow to the motor in relation to the magnitude of an electrical signal. One end of the test piece is twisted by the hydraulic motor controlled by a servo-valve. Angular displacement is monitored by a dual gang potentiometer. They develop proportional voltages which are fed back to their respective channels in the control unit. The other end is held fixed by a torque cell [89]. The torque cell of 113 Nm (1000 in-lb) capacity is used to measure the load transmitted by the test piece. It is calibrated for four ranges 100, 50, 25, and 10 Nm.

The test piece is held by two coaxial superalloy bars with attached heat resistant grips. The specimen is heated by a quadruple elliptical radiant furnace (model E4-10PA) connected to programmable controller with varied power input. The furnace is water-cooled and capable of temperatures up to 1200°C with rapid heating rates. A transparent quartz tube runs through the furnace enclosing the specimens, grips and bars. Argon is circulating through the tube during heating and testing to prevent oxidation. The temperature is measured by an alumel (K-type) thermocouple, insulated with double bore ceramic tubing, extending along the stationary test piece shoulder and attached to the specimen with alumel-chromel wire to maintain thermal contact. The location of the thermocouple tip on the gauge section at the fixed end of the specimen was determined to be satisfactory since the thermocouple could be rigidly fixed to the specimen yet underwent only a small fraction of its total revolutions without suffering damage[88]. The temperature of the test piece is displayed by a digital read- out temperature indicator [69]. The procedure of programming of the furnace temperature is provided in the Appendix. Figure 4.3 shows the picture of the furnace.

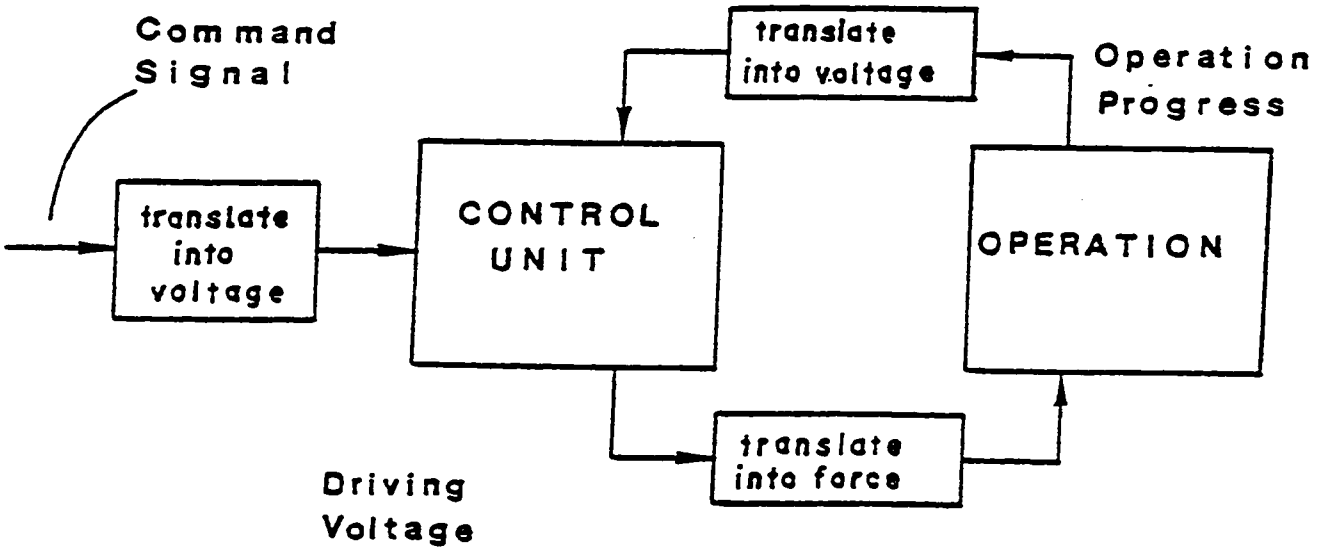

Figure 4.2 Logic of a closed loop controlling operation [92].

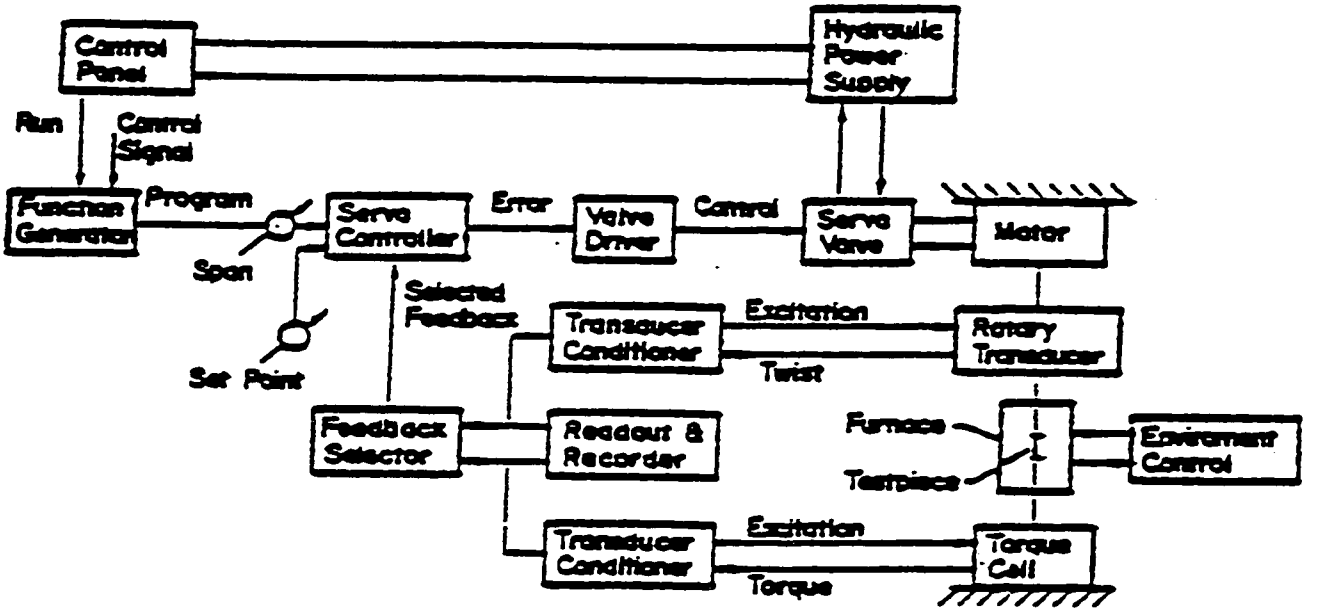

Figure 4.3: Block diagram of typical MTS system[88].

4.3 Computerized Testing System

The torsion machine was linked to an IBM-PC compatible 486/33 MHz. In this computer, OS/2 is employed for the operating system, together with Windows. TestStar is used to control the test procedure. Lotus 1-2-3/G was put on the hard disk for data processing. In a programmable system, the variations of all controllable parameters are entered via the program for the entire sequence which is initiated. The responsibilities of the computer may be viewed in terms of the following four categories[92,93]:

(i) Accept and interpret all test parameter information from the user.

(ii) Use the input information to activate the required hardware devices which will in turn send the appropriate command signals to the closed loop system and drive the test.

(iii) Monitor and record all output feedback information from the transducers within the closed loop system as the run is being executed.

(iv) Interpret the transducer output information and arrange it so it may be presented in a legible manner to the user.

4.4 Test Materials

Five different materials were used in the present studies. The specimens of alloy AZ91 were supplied as die cast by the Institute of Magnesium Technology, Sainte Foy, Quebec. The rest of the alloys, AZ31, AZ31 Mn, AZ63 and ZK60 , were supplied by Timminco, Ontario in the as-cast condition. The chemical compositions of the materials are shown in Table 4.1. Torsion specimens with axes parallel to the rolling or casting direction were machined to close tolerances, especially in gauge section, in order that twisting would be uniform. The test pieces have a gage length of 22.2 mm (0.875 in) and a diameter of 6.4 mm (0.25 in). The test specimen design is illustrated in Figure (4.4). Gage section geometry determines the deformation level and deformation rate for a given amount and a rate of twist. Alloy AZ91 was supplied by the Institute of Magnesium Technology as die cast specimens shown in Figure 4.5; no machining was performed on the gage section but only on the grips.

Table 4.1

Chemical Composition (wt%) [1]

Sample No.	Material	Composition							
		Al	Zn	Zr	Mn	Ca	Fe	Ni	Cu
1	AZ31	2.8	0.88	---	0.01	0.001	0.0031	0.001	0.001
2	AZ31 Mn	3.2	1.1	---	0.34	0.002	0.0014	0.001	0.001
3	AZ63	5.5	2.7	---	0.34	0.001	0.003	0.001	0.001
4	AZ91	9	0.7	---	0.13	---	---	0.001	0.001
5	ZK60	0.006	5.7	0.61	0.004	0.001	0.0066	0.001	0.001

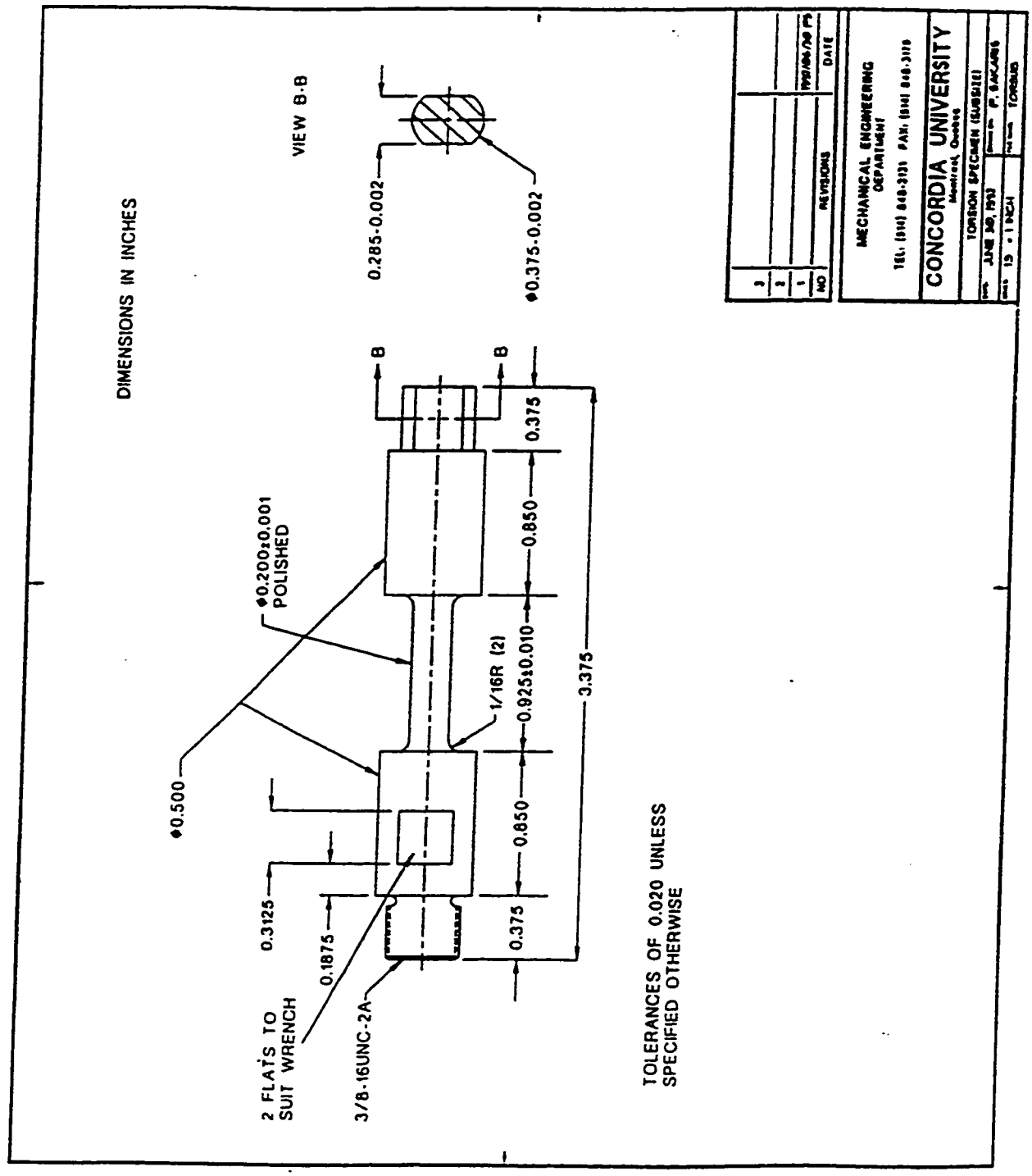

Figure 4.4: Torsion Specimen design.

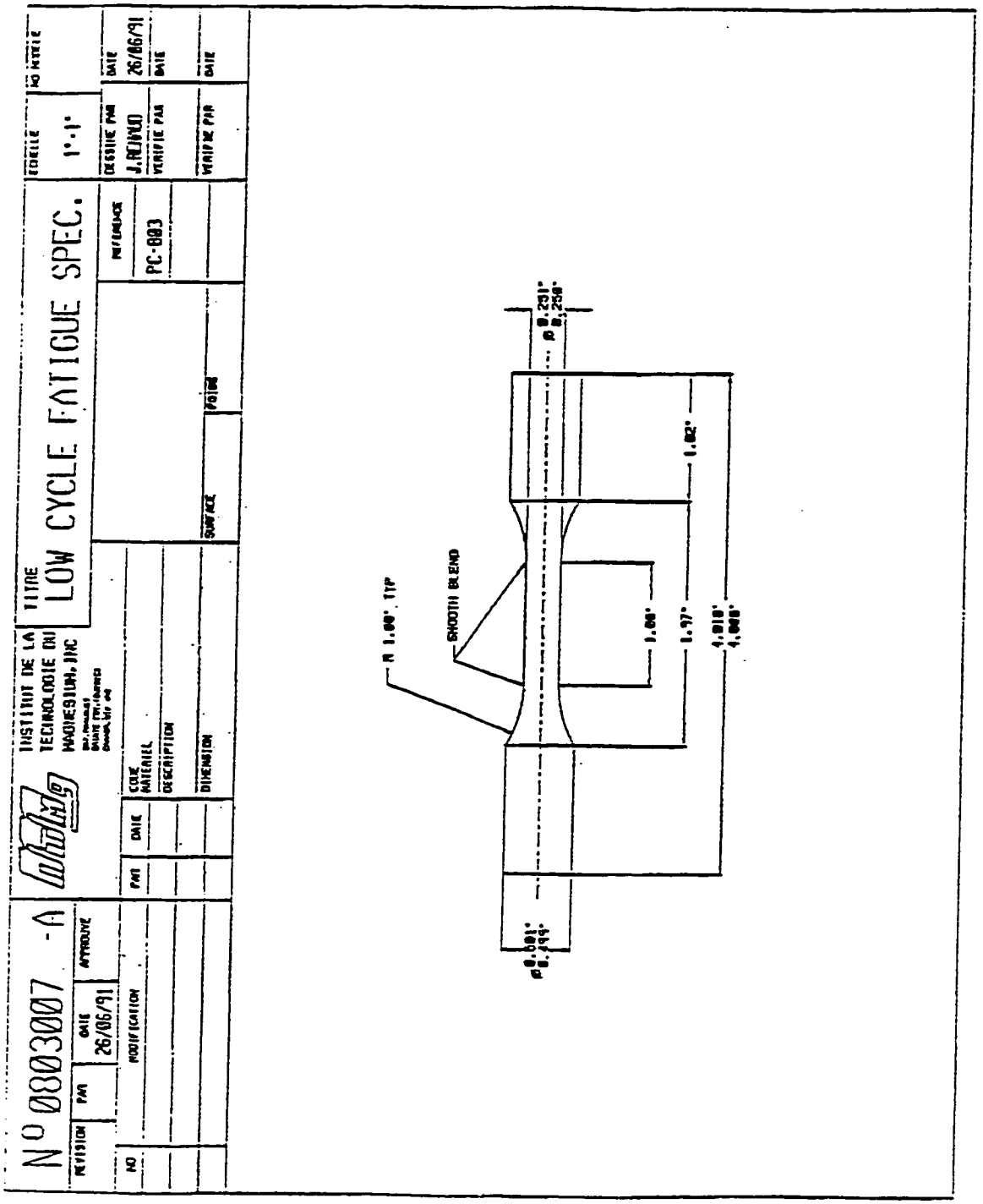

Figure 4.5: AZ91 die cast Specimen Design.

4.5 Test Procedures

Before starting any test, the reflecting surfaces of the furnace were cleaned with gauze so that the test temperature could be reached as quickly as possible. All specimens were inserted into the grips of the bars with a high temperature anti-seize agent and were tested in a controlled atmosphere of argon to prevent contamination during elevated temperature torsion studies. One end of the test specimen is threaded to be screwed into the grip attached to a torque transducer fixed to the lathe bed, while the other end has a rectangular section which fits into a slot attached to the actuator [91,92]. The specimen is not fully pushed into the slot until heated to avoid damaging the specimen. This arrangement allows for easy mounting and removal without accidentally straining the specimen.

Each specimen was heated to the desired temperature T within five minutes and held constant at that homogenizing temperature for ten minutes prior to deformation. The AZ91 specimens were tested at three different strain rates ($\dot{\varepsilon}$) of 0.05, 0.5 and 5.0 s^{-1} and at eight temperatures between 150 and 450°C. At high T, they suffered from hot shortness; however, this was eliminated by a prior thermo-mechanical process (TMP) at 300°C, 0.5 s-1, up to ε = 0.4 (2 stages of 0.2 with an interval of 5 minutes) which was approximately half the fracture strain. The rest of the specimens, supplied by Timminco, Ontario, were tested in the 'as-received' condition yielded very poor results due to early crack initiation at voids. Subsequently specimens were subjected to prior Hot Isostatic Pressing (HIPping) in order to reduce porosity and then deformed with the essentially as-cast microstructure which was expected to be quite fine grained. The specimens were twisted without any interruption to fracture. All specimens were quenched in water in less than two

seconds after deformation was completed. The data were stored by the computer and displayed as torque (Γ) versus angle (θ).

Only one test was conducted for each condition because this has been traditional in hot working in order to reduce the long time required to set up (several hours) and carry out multiple tests for each condition. The specimens are examined visually to ensure that the strain is uniform, indicating the absence of prior defects. For validation the results obtained throughout the matrix of conditions are compared to each other by several functions to check consistency and to tests conducted by other investigators on similar alloys.

4.6 Metallographic Procedure

In order to investigate the change in the structure with deformation, the gage lengths were sectioned using a diamond blade on a low speed saw to reveal tangential, longitudinal and transverse sections The specimens were then coarse ground through gage and shoulder simultaneously to produce a tangential flat slightly below the surface and a chord respectively. this permitted viewing the rapidly rising strain in the transition region from shoulder to gage. The specimens were subjected to mechanical grinding through 600 grit SiC paper, polishing on kitten ear cloth with 6μm and 1μm diamond paste with lubricating oil and finishing with 0.3μm and then 0.05μm alumina with distilled water. The surface was chemically polished with 10% nital for 10-15 s and then etched with acetic-picral

(5ml acetic acid, 6g picric acid, 10ml water, 100ml methanol); this is repeated until scratches and disturbed layer are removed.

5.EXPERIMENTAL RESULTS

5.1 Mechanical Results

5.1.1 Stress – Strain Curves

The torque and twist data were converted through the use of Equations 4.1 to 4.4 to equivalent σ and ε, in order to compare them to the findings of other researchers. The value of m was taken as the slope of $\log \Gamma$ versus $\log \dot{\varepsilon}$ (Figure 5.1 to 5.5). The m values vary from about 0.08 at 240 to 300°C up to 0.17 near 450°C for all five materials. The equivalent σ-ε curves for five materials are presented in Figures 5.6-5.9. The values of n' were taken as zero, which is valid only at the peak and during steady state, this introduces an error of less than 5% while greatly simplifying the analysis.

Strength comparison of the 5 alloys show that the peak stress is governed by the composition. Manganese is of great commercial importance not only in increasing corrosion resistance of Mg alloys but it increases the strength of both wrought and cast alloys. The addition of Al not only increases the strength, also improves the ductility of the alloys. Zinc also has great strengthening properties in both wrought and cast alloys. In the present study the alloys with high Al, Zn and Mn were found to have the highest strength and decreased in the order: AZ63 (5.5Al-2.7Zn-0.34Mn), AZ31-Mn (5.5Al-1.1Zn-0.34Mn), AZ91 (9Al-0.7Zn-0.13Mn), AZ31 (2.8Al-0.88Zn-0.01Mn) and finally ZK60 (Mg-5.7Zn-

0.65Zr-0.01Al). At temperatures below 300°C failure occurs near the peak and at higher T failure occurs well after the peak. The flow curves exhibit a rapid hardening at low strains to a peak followed by a decline towards a plateau. For these alloys σ_p decreases as T rises and $\dot{\varepsilon}$ declines, from as much as 260 to about 20 MPa. The strengths are consistent with those reported by other investigators [1].

The as-cast specimens of alloy AZ91 experienced hot shortness at 360°C and above; however in that domain, after a prior TMP at 300°C, they showed much improved properties, which are reported along with the as-cast properties at 300°C (Figure 5.7). The behavior of ZK60 (Figure 5.8) follows the pattern of the other alloys but is uniformly weaker across the entire range.

Figure 5.9 shows representative flow curves from isothermal multistage tests deformed at 240-420°C for AZ63, 0.01-1.0 s^{-1}; in the true hot working regime, the flow curves rise to a peak and are followed by gradual work softening characteristic of DRX in Mg alloys. The flow curve in each pass is strongly affected by the fractional softening (FS) preceding the pass as a result of the carry-over of the worked substructure from the previous passes. The flow stresses generally decrease with increasing deformation temperature, although the variation with strain rate are not consistent, the strengths on average are similar to the tests conducted by other investigators [1]. The intervals of 20 seconds between passes cause noticeable softening at 1.0 s^{-1} for 240 and 300°C. But under other conditions the softening is very little and does not change the combined flow curve substantially so that peak stresses can be derived for constitutive analysis.

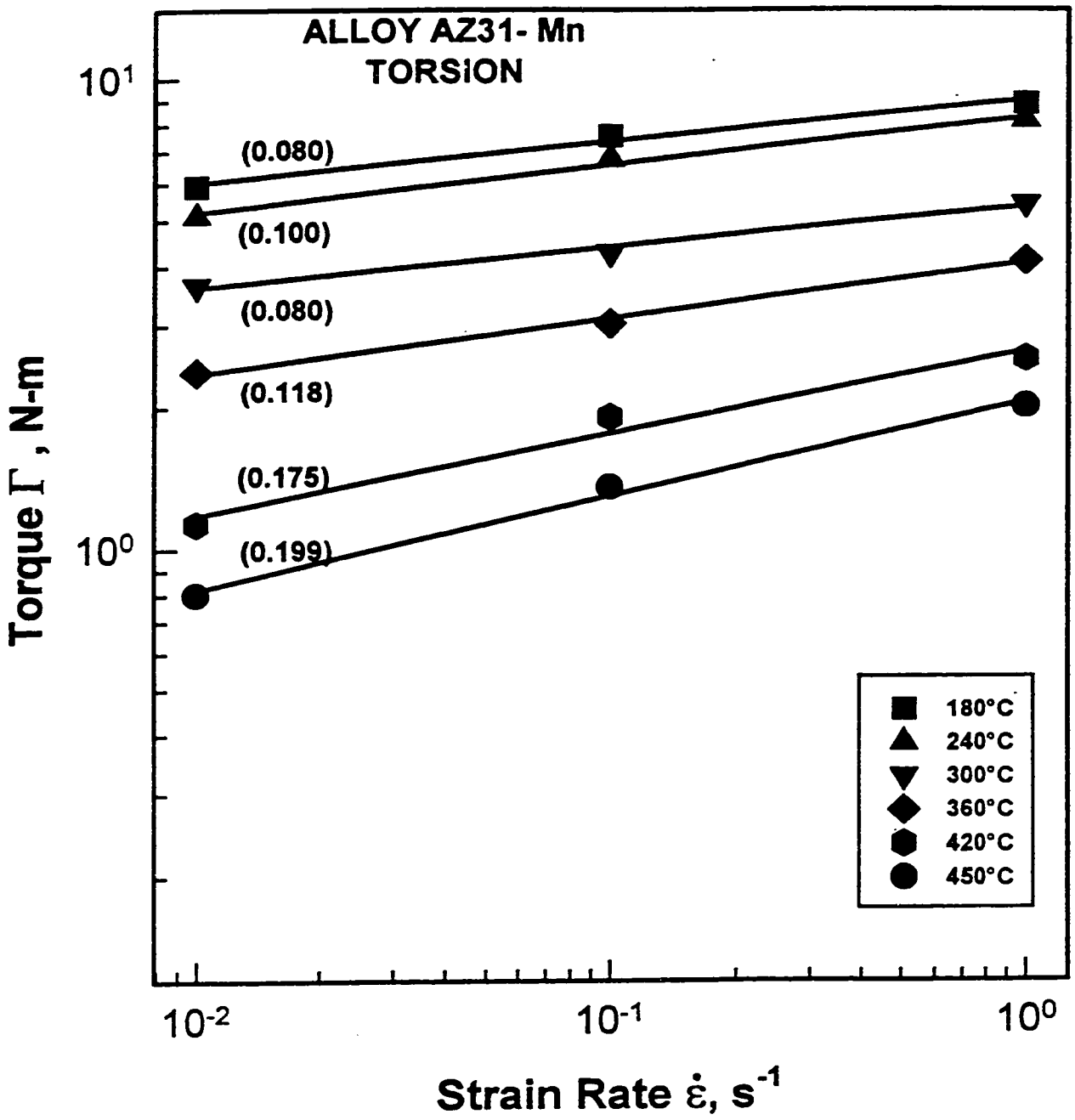

Figure 5.1 Plot of log Γ versus log$\dot{\varepsilon}$ for the alloy AZ31-Mn was used to calculate the m value.

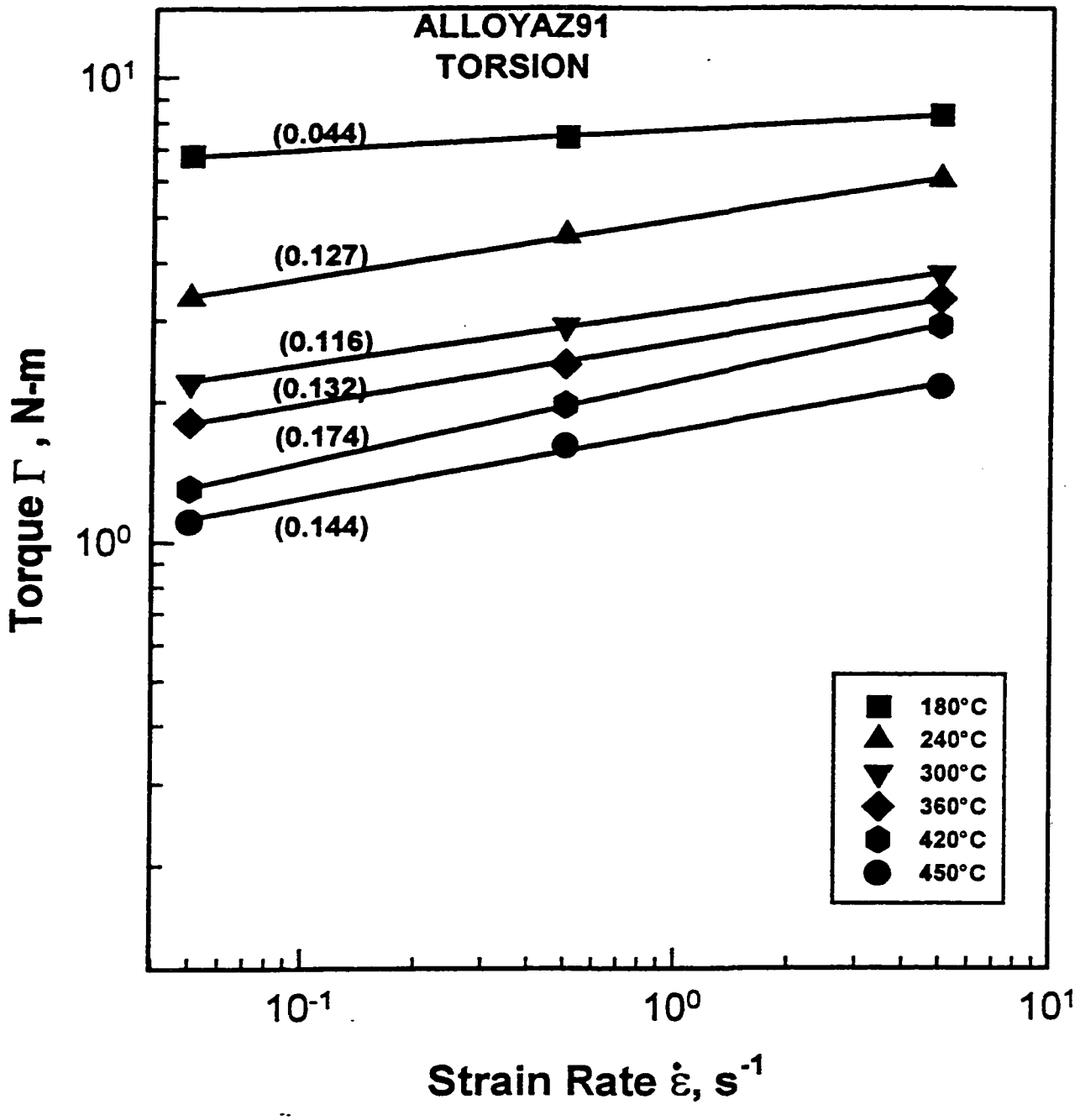

Figure 5.2 Plot of log Γ versus logε̇ for the alloy AZ91 was used to calculate the m value.

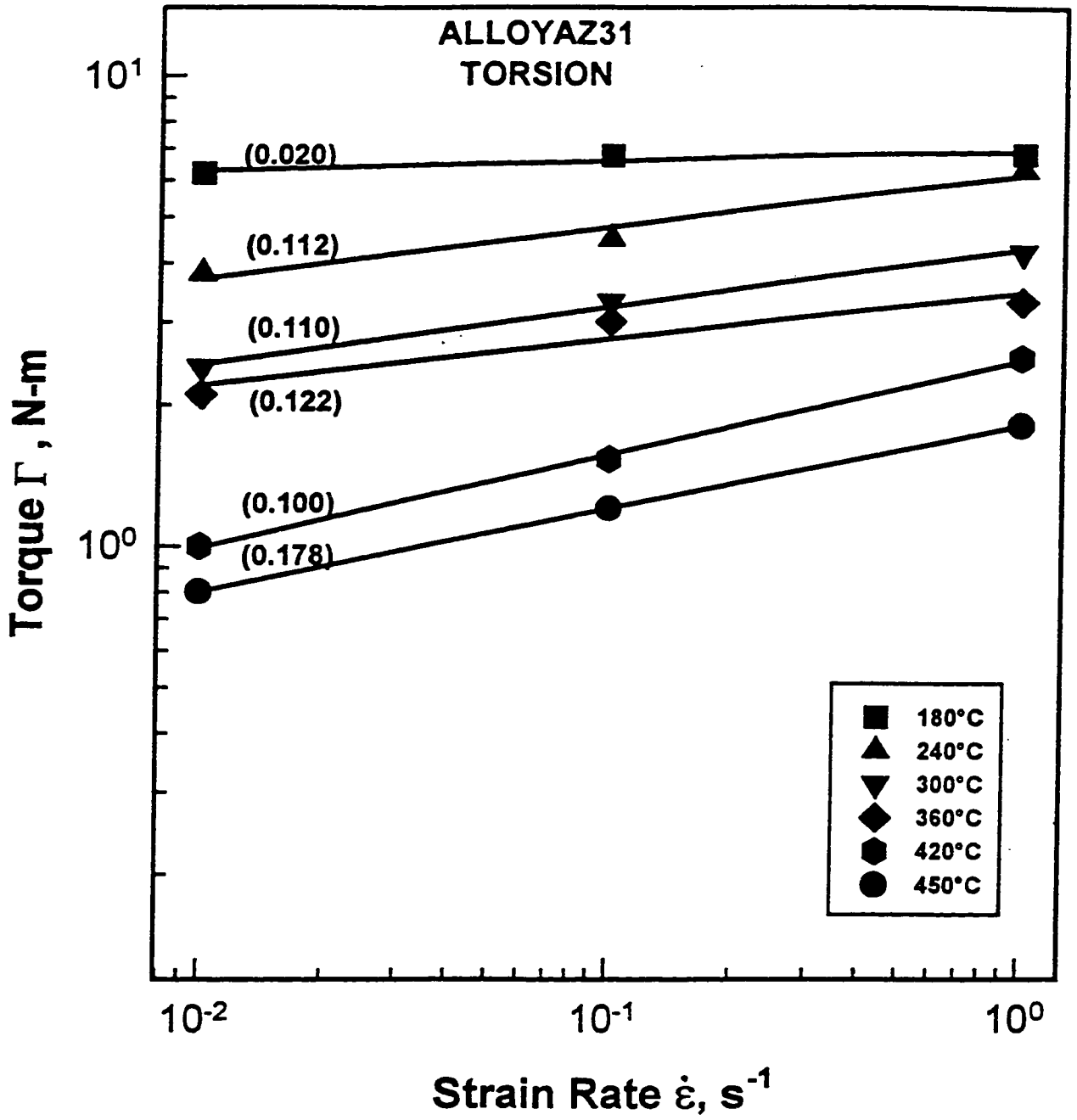

Figure 5.3 Plot of log Γ versus log$\dot{\varepsilon}$ for the alloy AZ31 was used to calculate the m value.

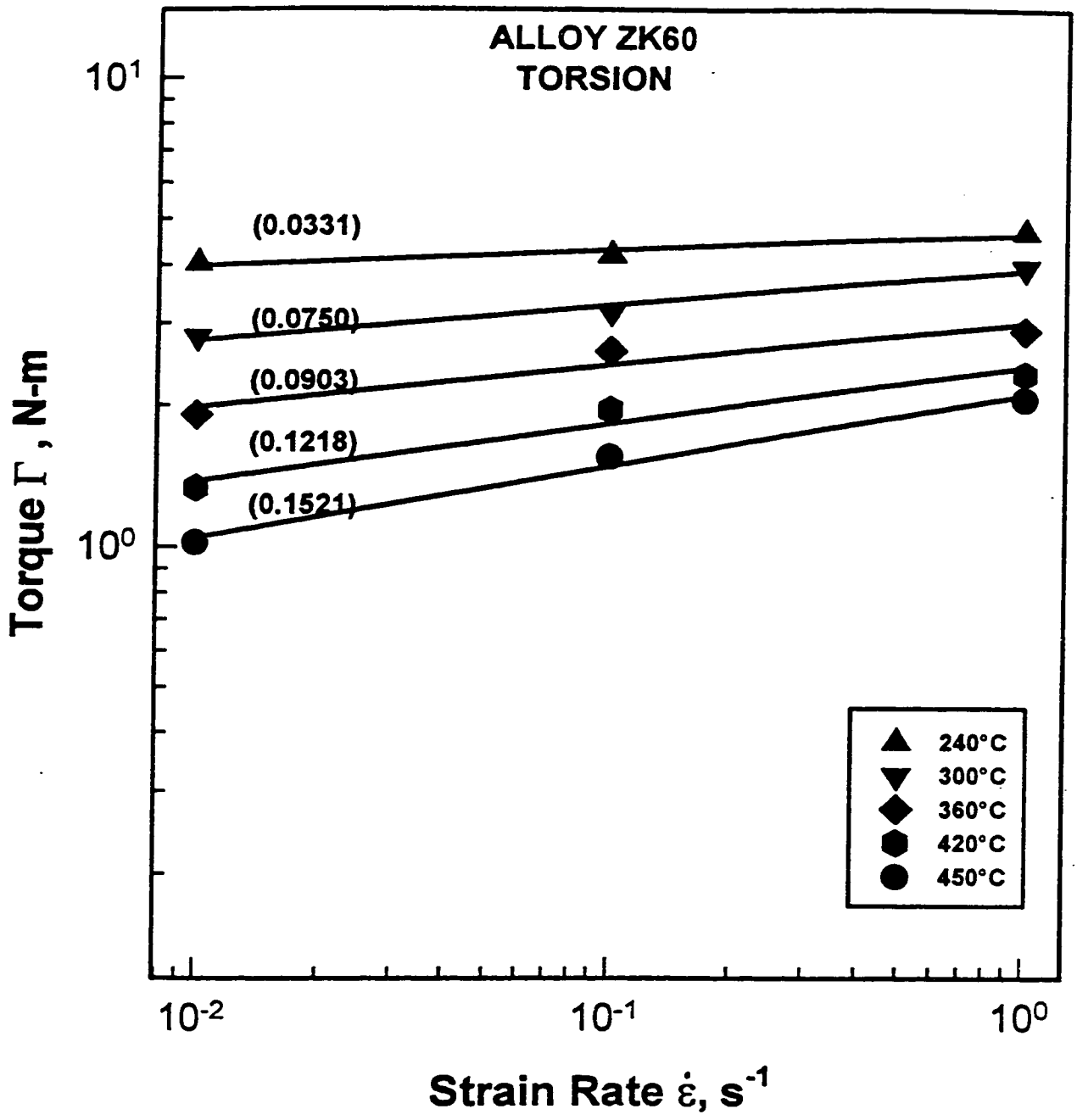

Figure 5.4 Plot of log Γ versus log$\dot{\varepsilon}$ for the alloy ZK60 was used to calculate the *m* value.

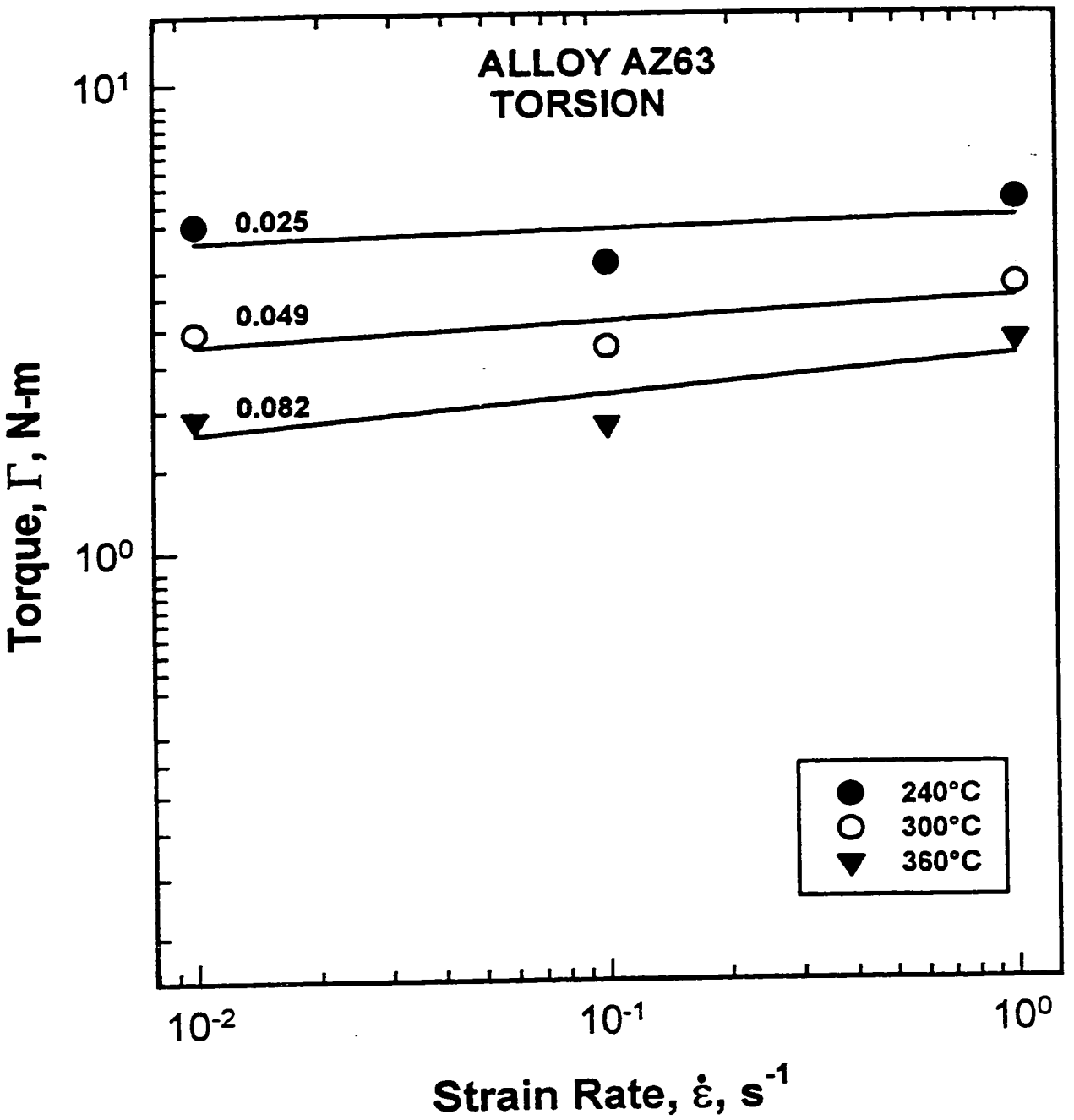

Figure 5.5 Plot of log Γ versus log$\dot{\varepsilon}$ for the alloy AZ63 was used to calculate the *m* value.

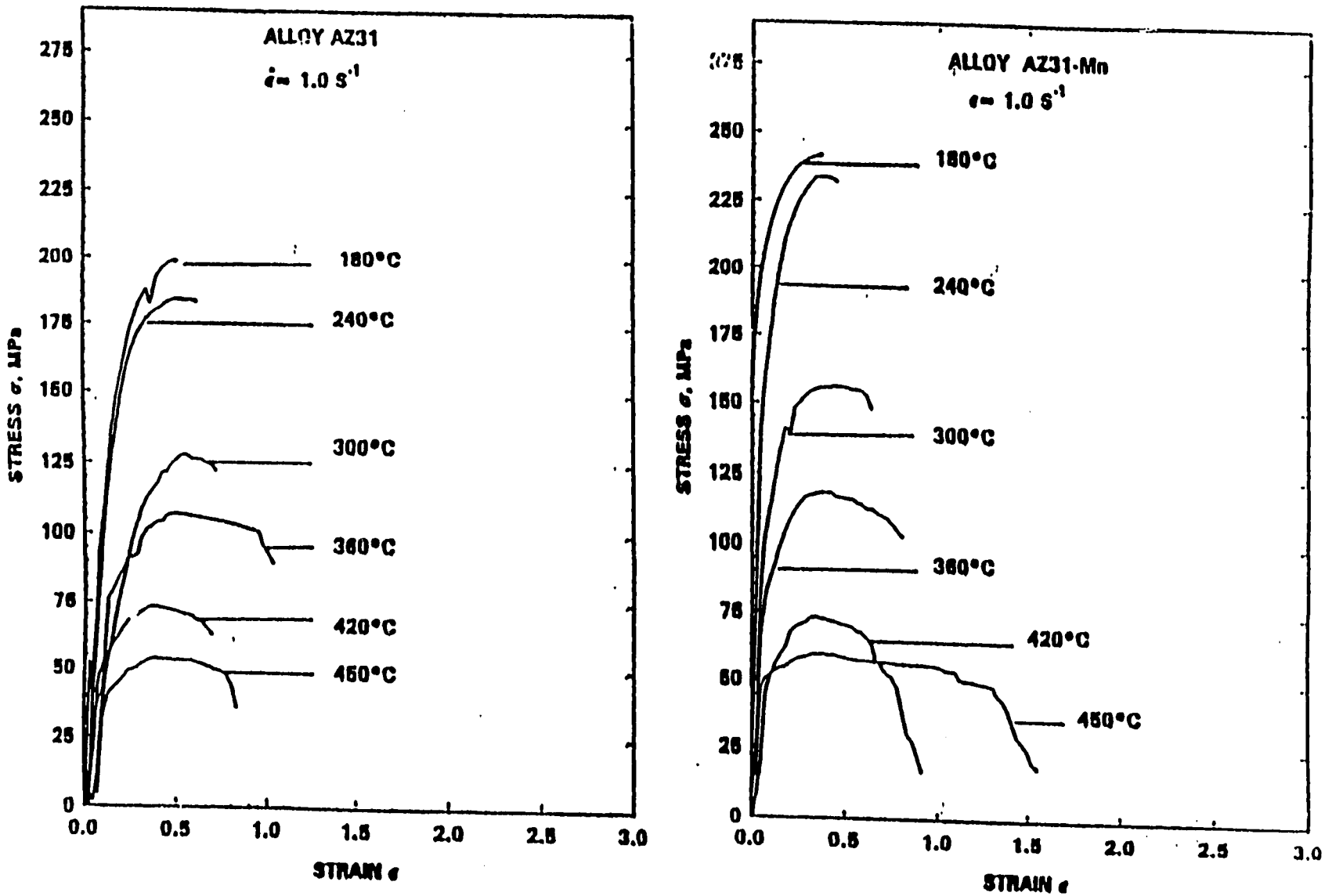

Figure 5.6 Representative σ-ε curves for alloys (a) AZ31 and (b) AZ31-Mn

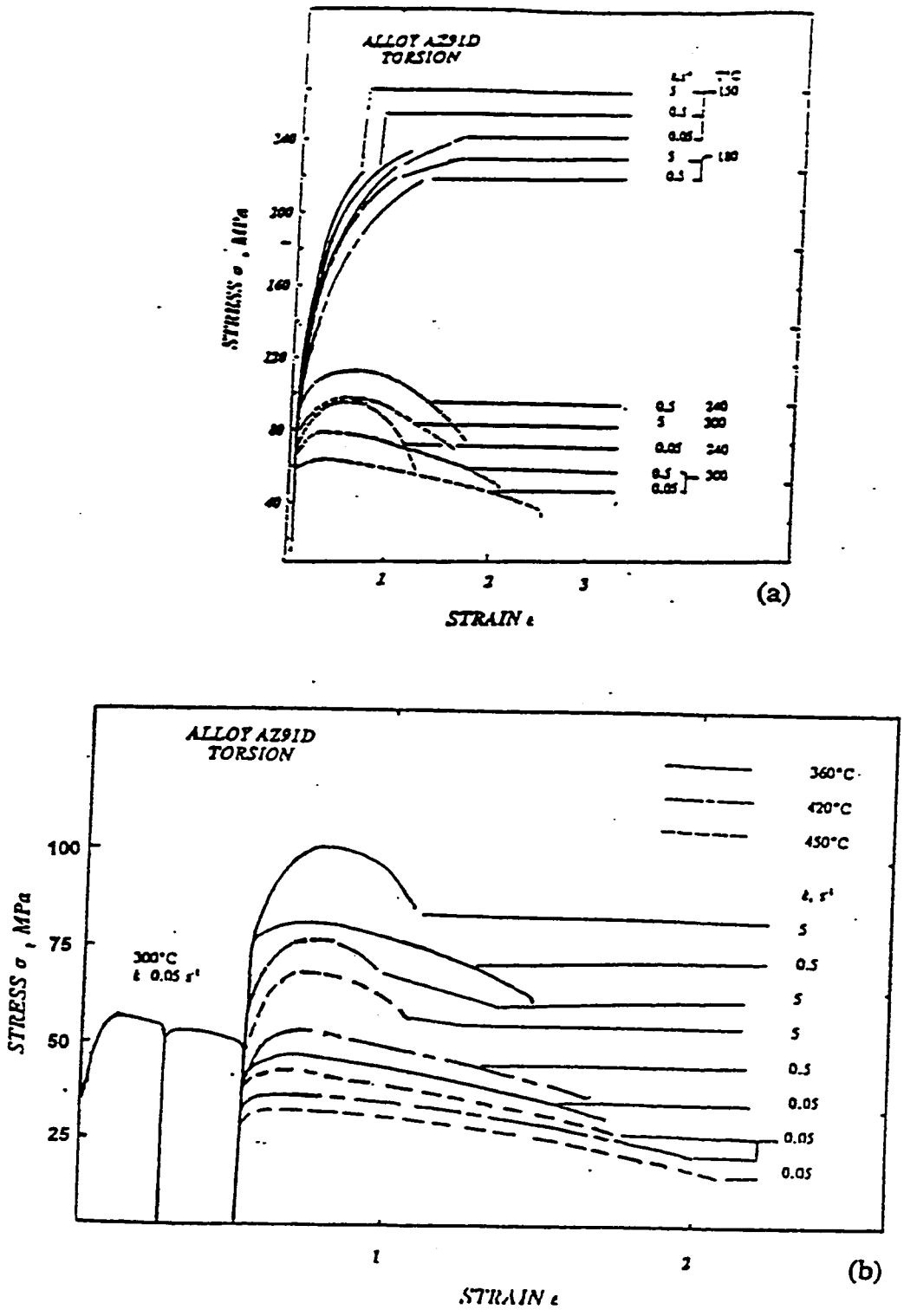

Figure 5.7 Representative σ-ε curves for alloy AZ91.

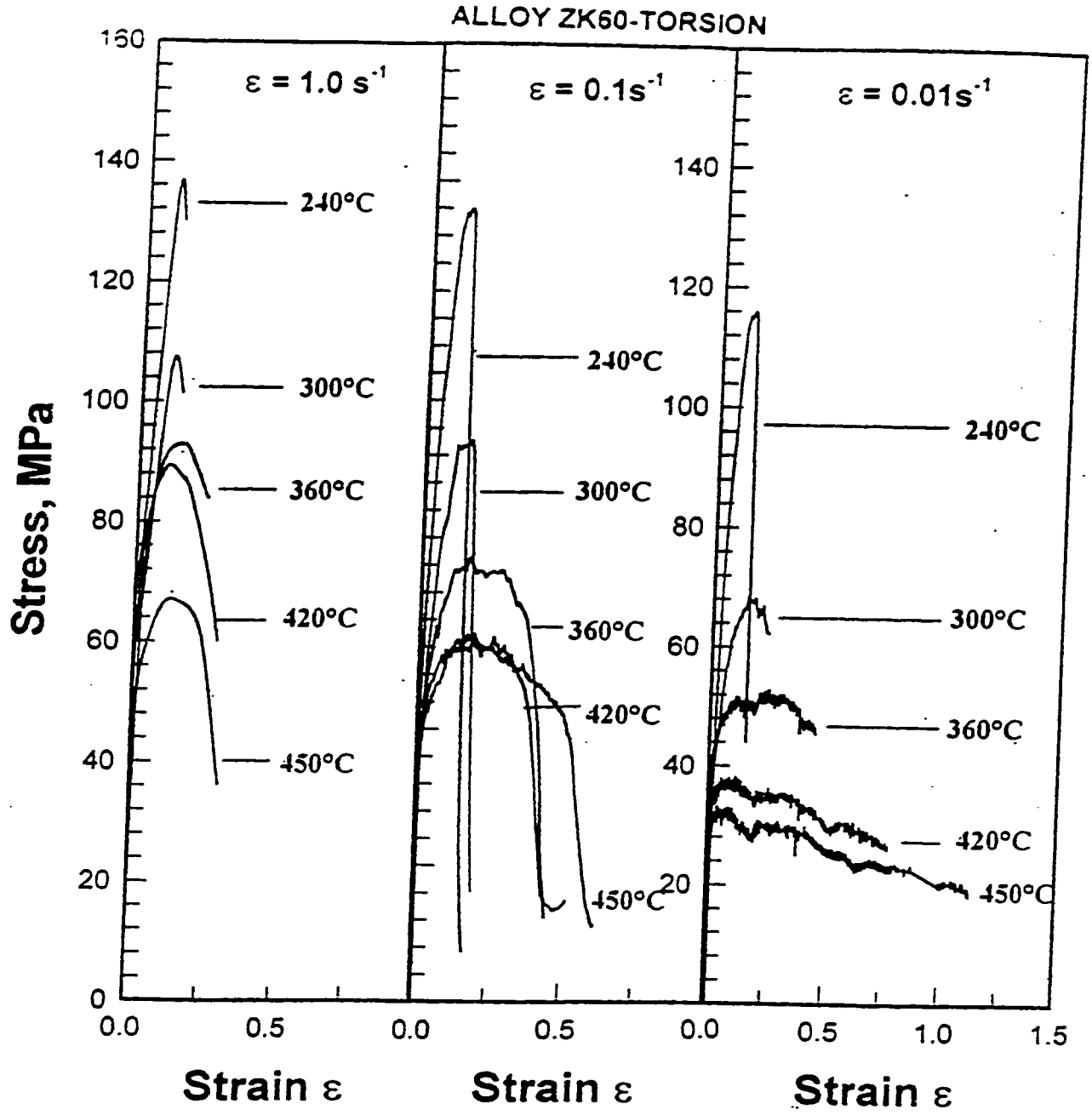

Figure 5.8 Representative σ-ε curves for alloy ZK60

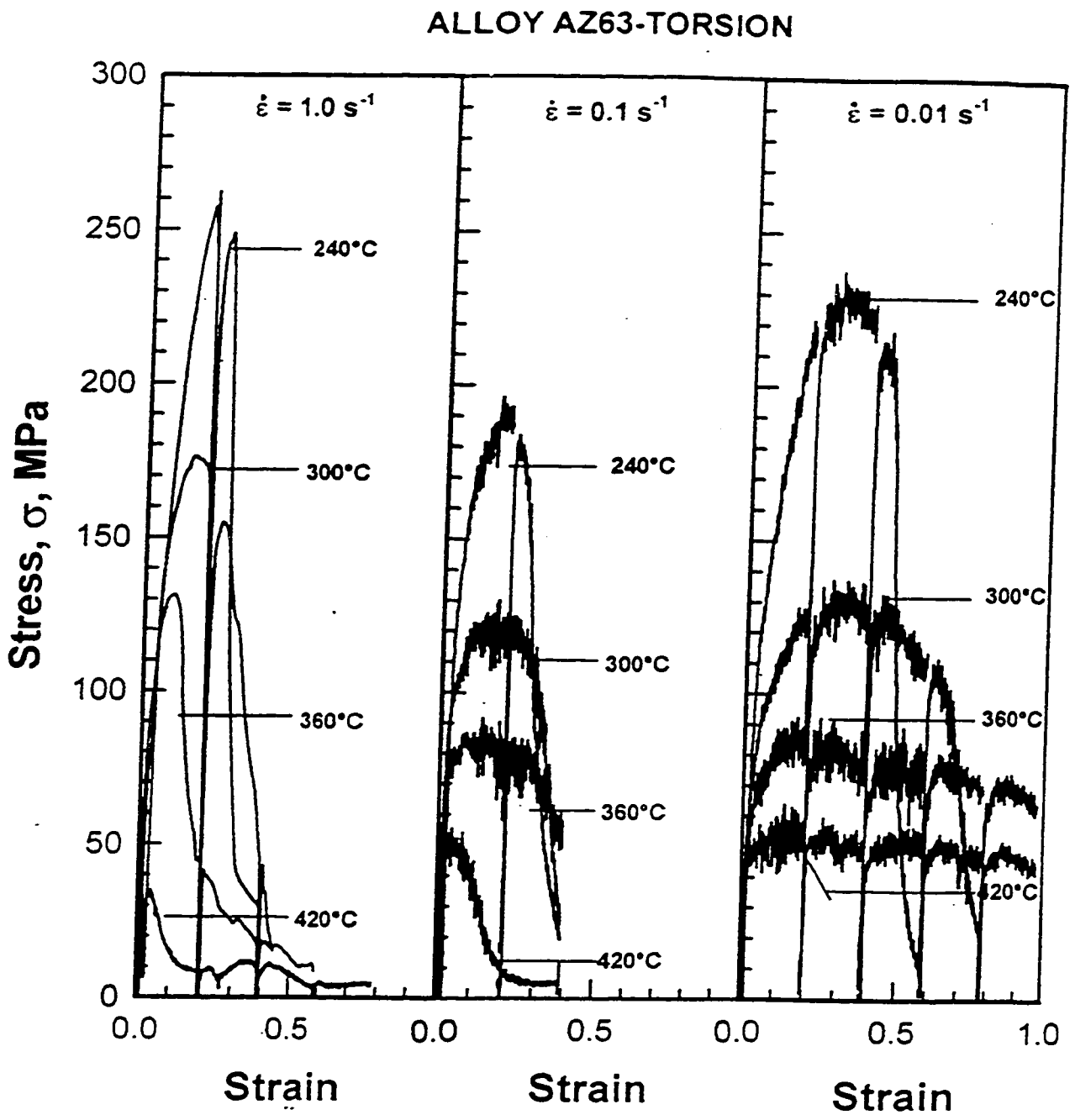

Figure 5.9 Representative multistage σ-ε curves (ε_i = 0.2, t_i = 20s) for alloy AZ63.

5.1.2 Peak Stress

The peak stresses decreases fairly smoothly but at a decreasing rate with rising temperature and are clearly higher with rising strain rate for all alloys except for AZ63 as shown in Figures 5.10-5.14. For the alloy AZ63 (Figure 5.14), the peak stresses at $0.01s^{-1}$ have values that are anomalously high. The inconsistency of the results appears to be the result of casting defects or segregation. It was not possible to confirm the results since so many specimens failed prematurely clearly as a result of major defects. The strengths at 1.0 s^{-1} and 0.1 s^{-1} are consistently slightly higher than those of AZ31. The strengths at 0.01 s^{-1} appear higher than that at 1.0 and 0.01 s^{-1} and out of line with the values for other alloys; evidently there was an error in test procedures so the results should be neglected. Further tests need to be conducted for AZ63 before the constitutive constants can be used for process modeling.

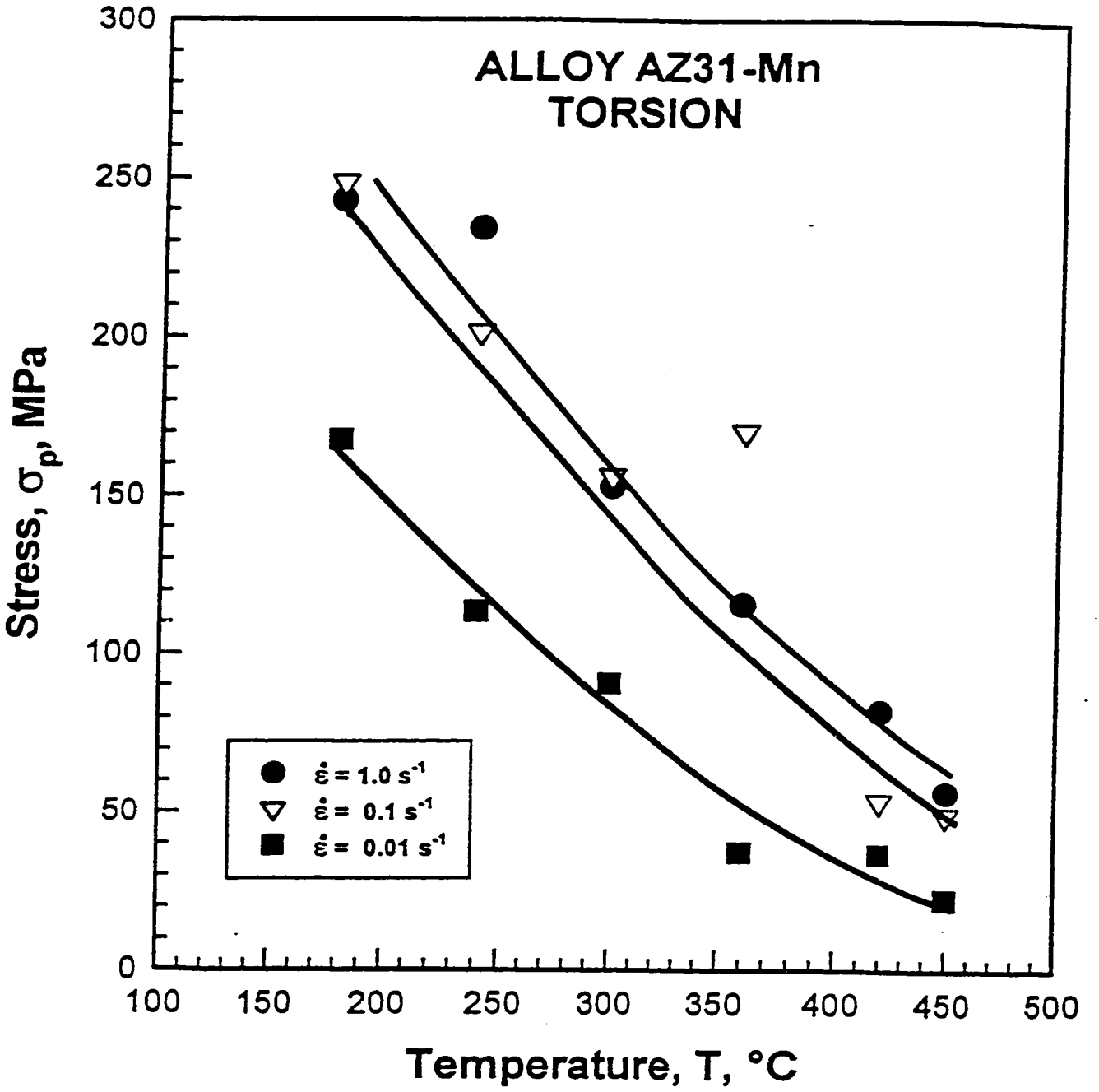

Figure 5.10 Strengths for the alloy AZ31-Mn declines uniformly with rising T.

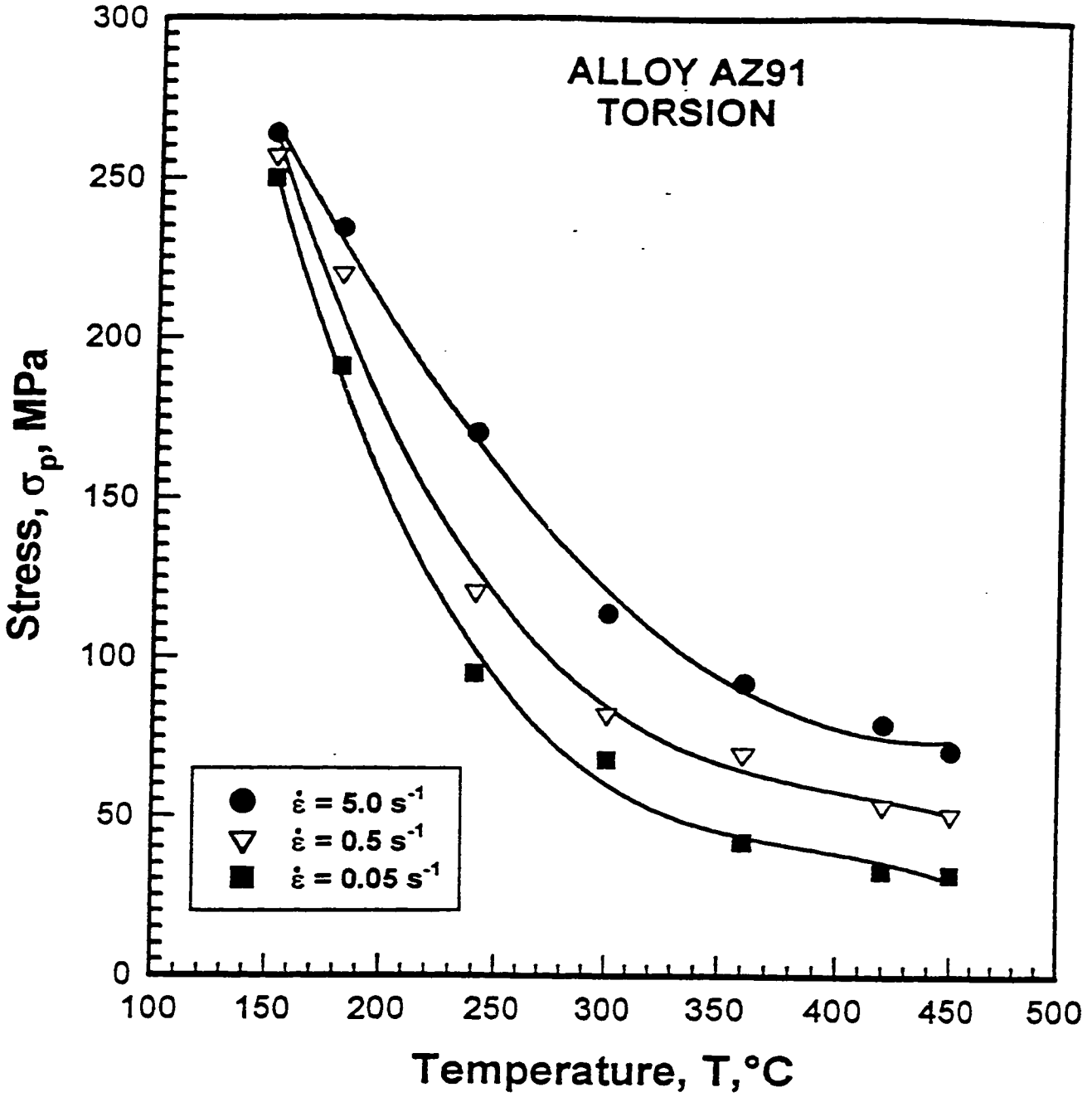

Figure 5.11 Strengths for the alloy AZ91 shows a general decline with rising T.

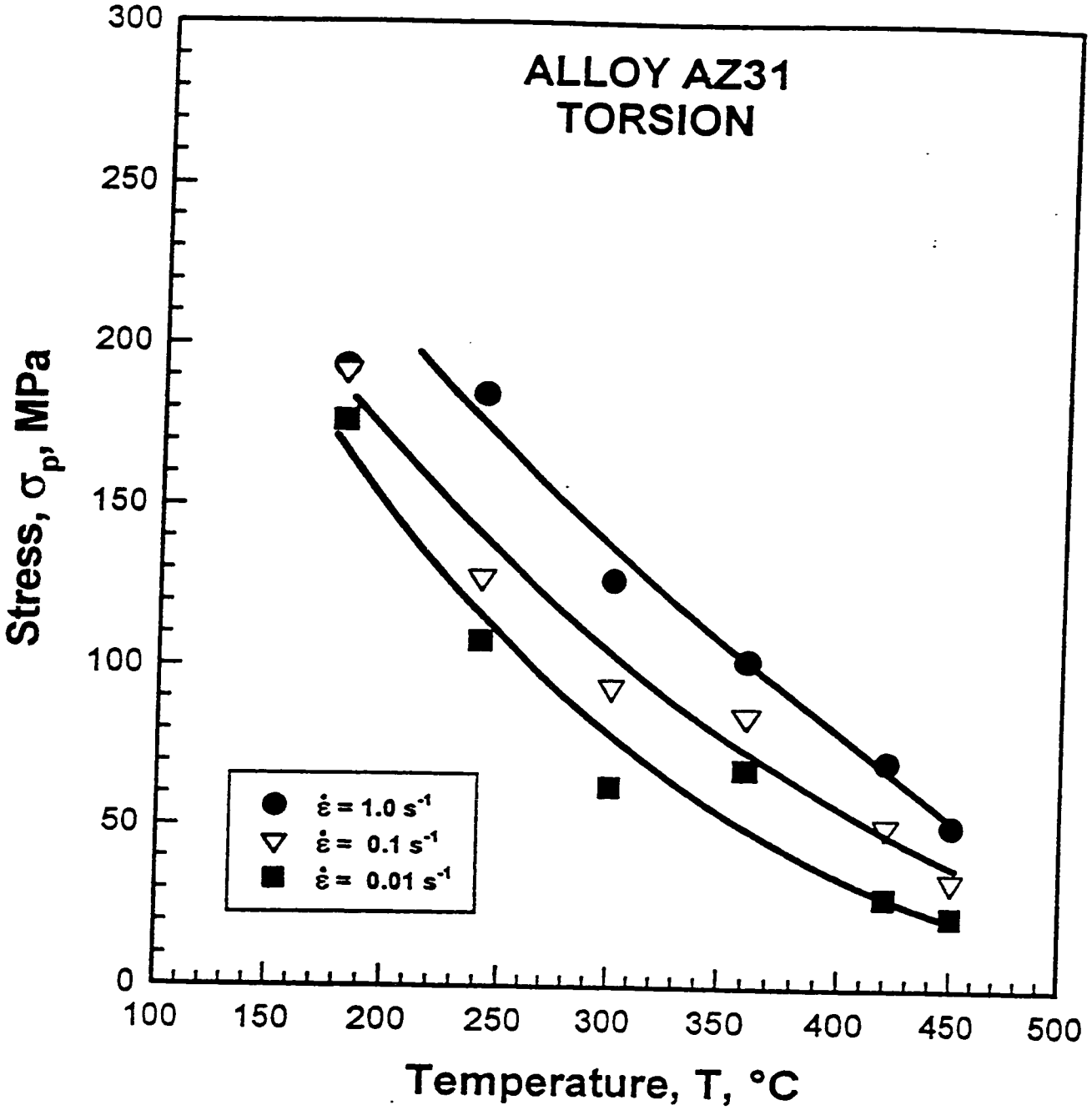

Figure 5.12 Strengths for the alloy AZ31 declines uniformly with rising T.

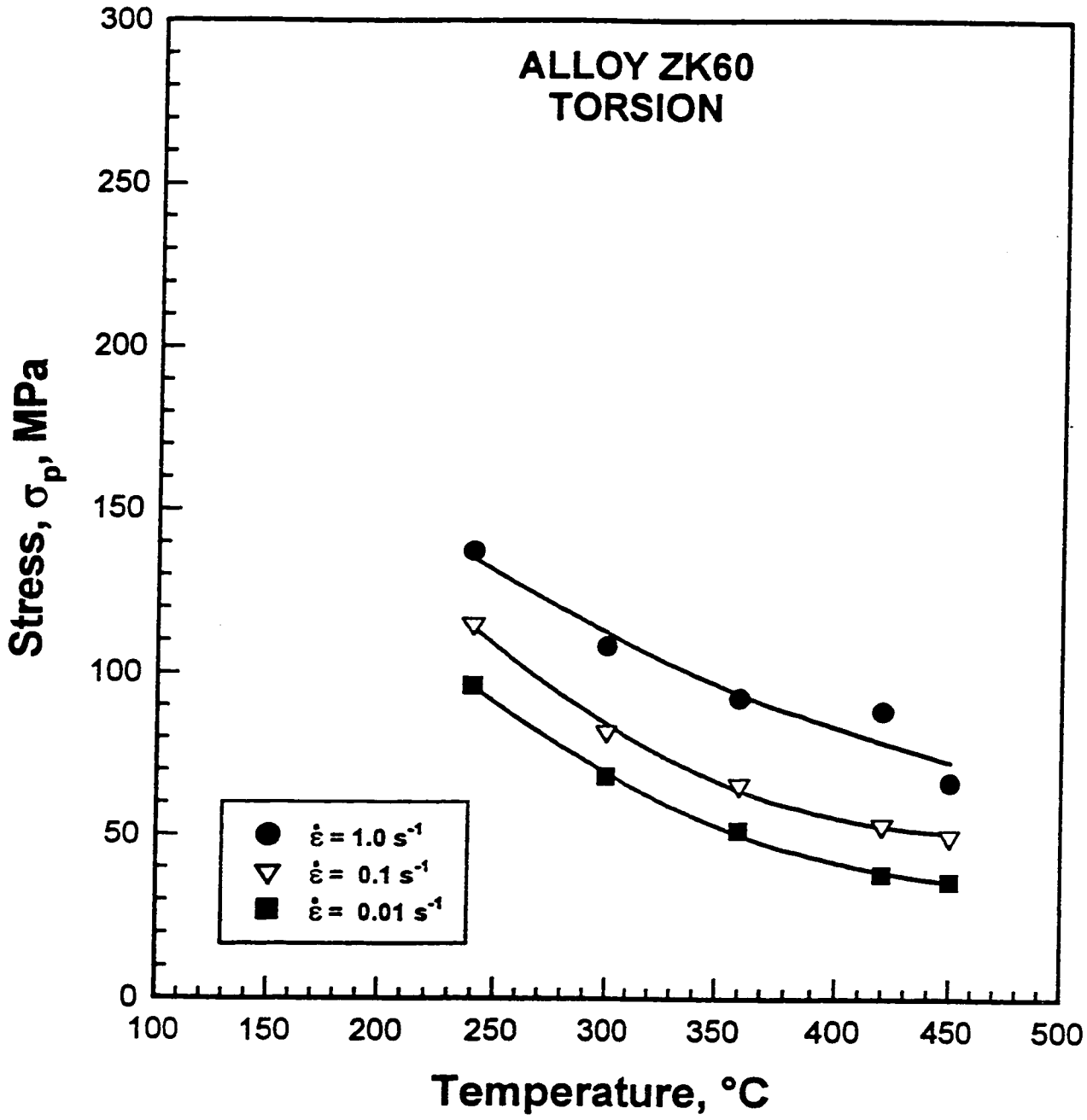

Figure 5.13 Strengths for the alloy ZK60 declines uniformly with rising T.

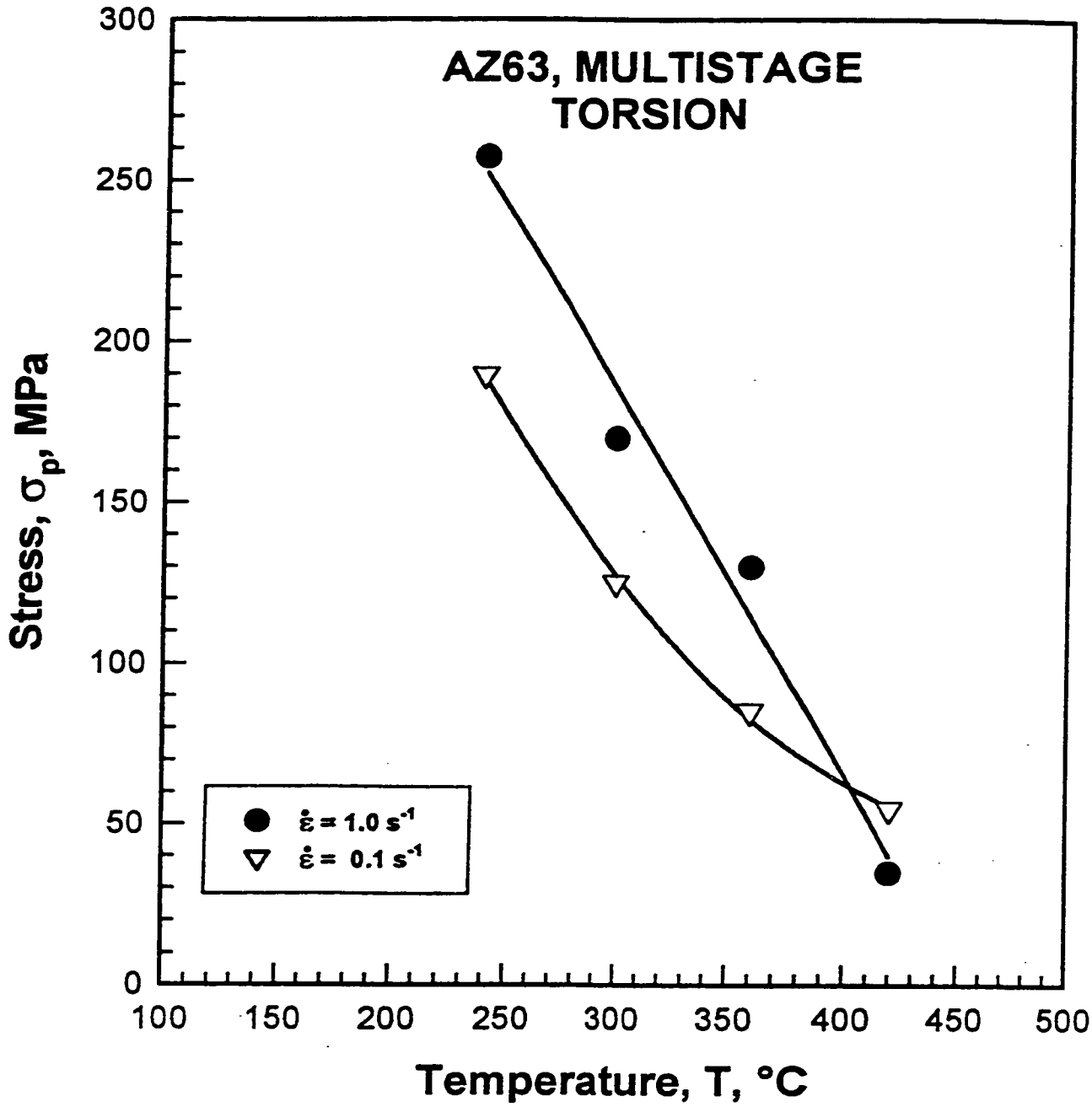

Figure 5.14 Strengths for the alloy AZ63 generally decline with rising T and are lower for lower strain rate except at 420°C.

5.1.3 Ductility

Torsional ductilities of the five materials are shown as graphs of strain to failure ε_f versus test temperature in Figures 5.15 to 5.19. In general, the ductility rises as the temperature rises and is higher for lower strain rate. The ductilities of all the alloys are in the range 0.2 to 1.0 below 300°C with the exception of AZ91 with high values. Above 340°C, the ductilities rise to the range 1.5 to 2.5 notably at low $\dot{\varepsilon}$ but at higher $\dot{\varepsilon}$ are maxima near 300°C except that AZ63 is quite different from the other alloys. In general strain increases rapidly initially and then slowly with rising T in parallel with the stresses decreasing rapidly at low T and more gradually at high T. As an exception, ε_f for ZK60 rises more rapidly at high T than at low.

The fracture strain of AZ63 rises to a maximum of about 1.0 at 420°C for 0.1 s^{-1} but is much lower than that of other alloys; it does not significantly rise with T at high strain rates. The fracture strain of alloy AZ31 Mn rises to about 2.5 at $\dot{\varepsilon}$ of $0.01s^{-1}$. In contrast the ductility of AZ31 saturates near 2.0 at 450°C and $0.01s^{-1}$. The lower result than that of AZ31-Mn may be explained by the presence of voids in the AZ31 which contributed to a marked reduction in its fracture strain. The alloy AZ91 exhibited good ductility in the intermediate range in the as-cast condition and high T range (above 300°C) in a TMP condition. The fracture strain ε_f rises from about 0.75 to 2.5 as T rises at $\dot{\varepsilon}$ =0.5 s^{-1}, but for each T, declines as $\dot{\varepsilon}$ rises, most noticeably from 2.5 to 1.25 at 420°C. For the alloy ZK60 the hot ductility generally rises with increasing T becoming almost twice as great due to

DRX in the hot working region (360°C and above) as in the warm working regime. Decreasing $\dot{\varepsilon}$ clearly raises the ε_f particularly above 350°C.

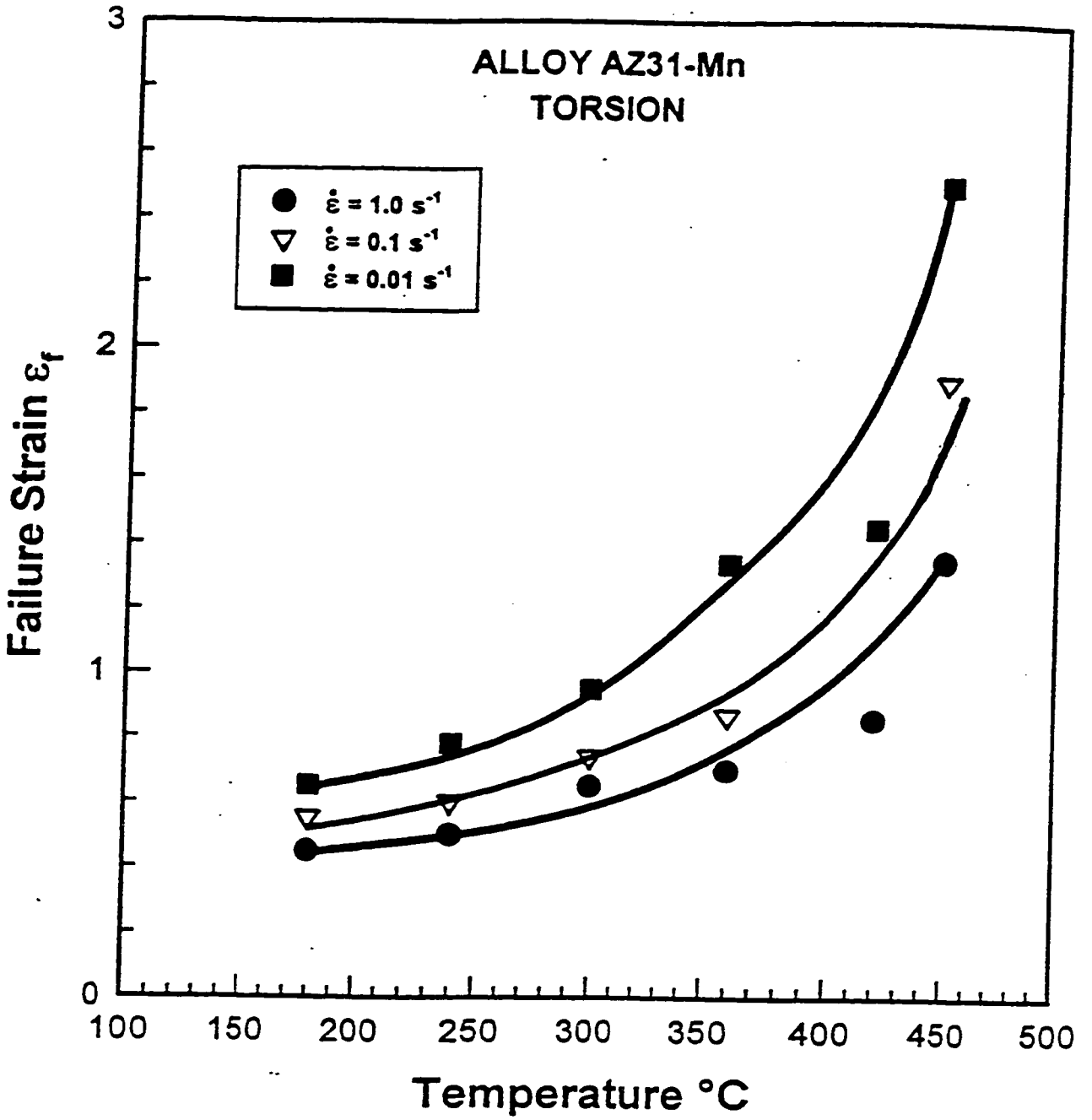

Figure 5.15 Ductility for the alloy AZ31-Mn increases with rising temperature and lower strain rate.

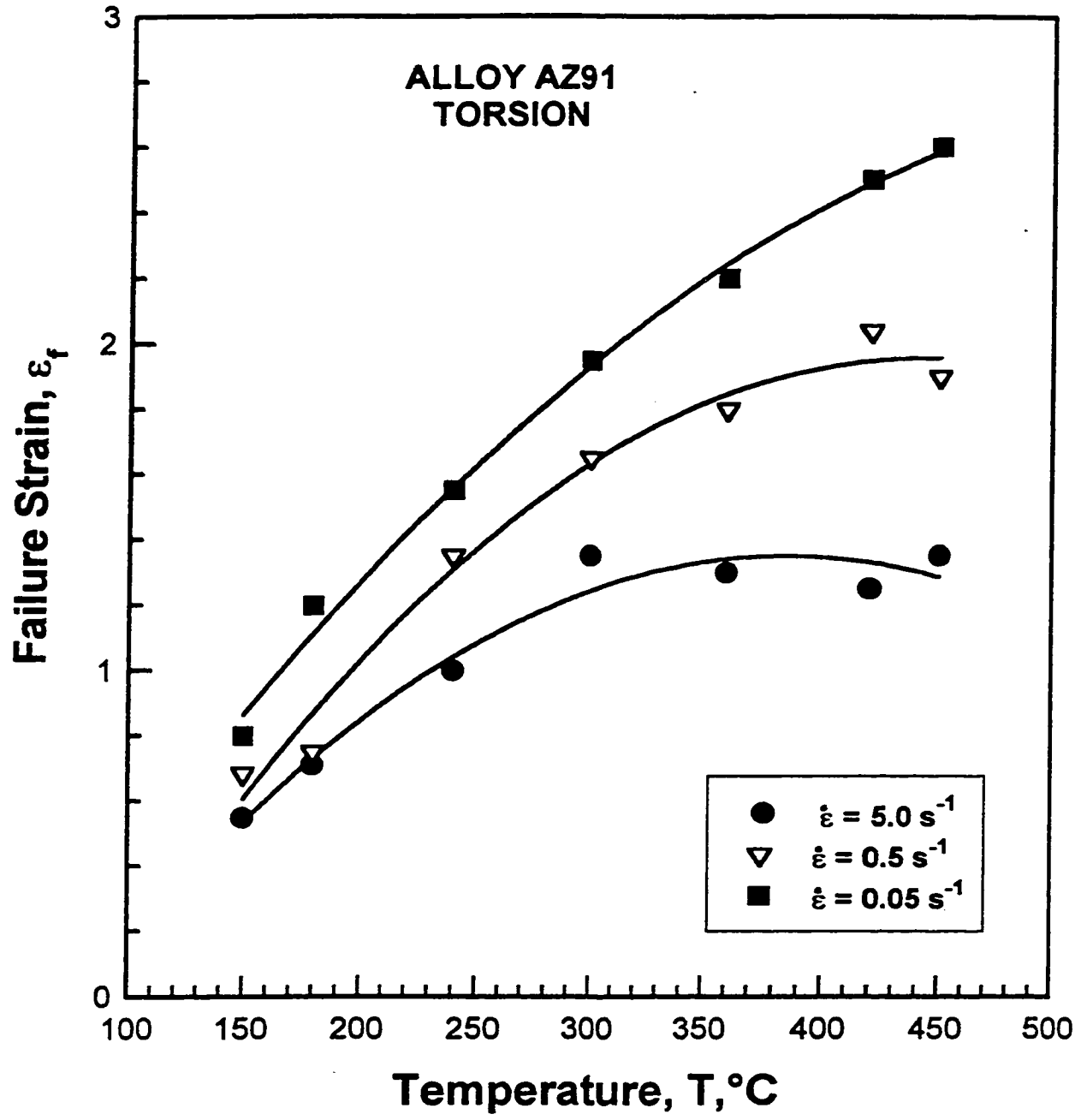

Figure 5.16 Ductility for the alloy AZ91 increases with rising temperature and lower strain rate.

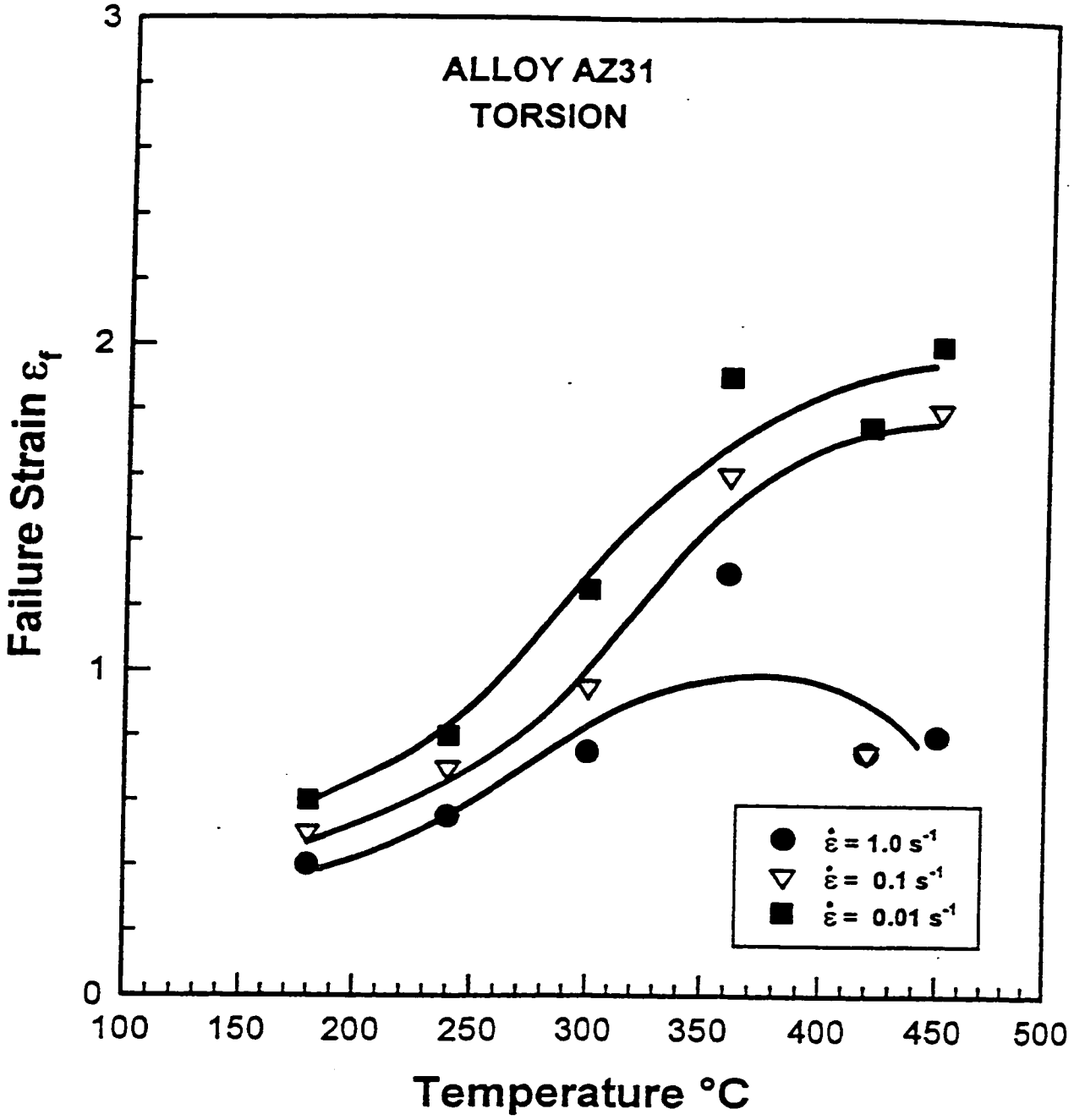

Figure 5.17 Ductility for the alloy AZ31 increases with rising temperature and lower strain rate but declines at the highest T.

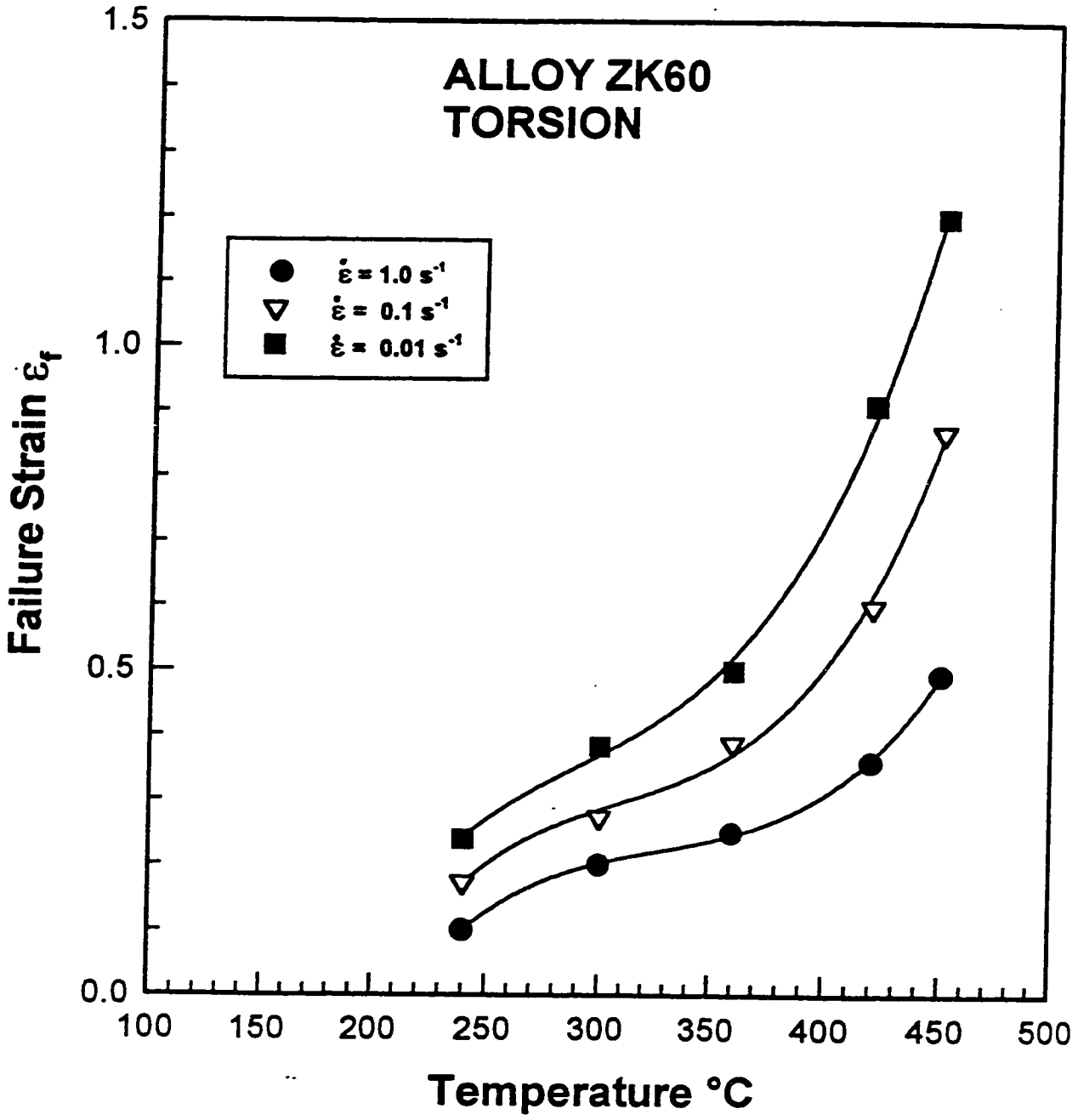

Figure 5.18 There is a marked improvement in ductility for the alloy ZK60 at higher T and low $\dot{\varepsilon}$

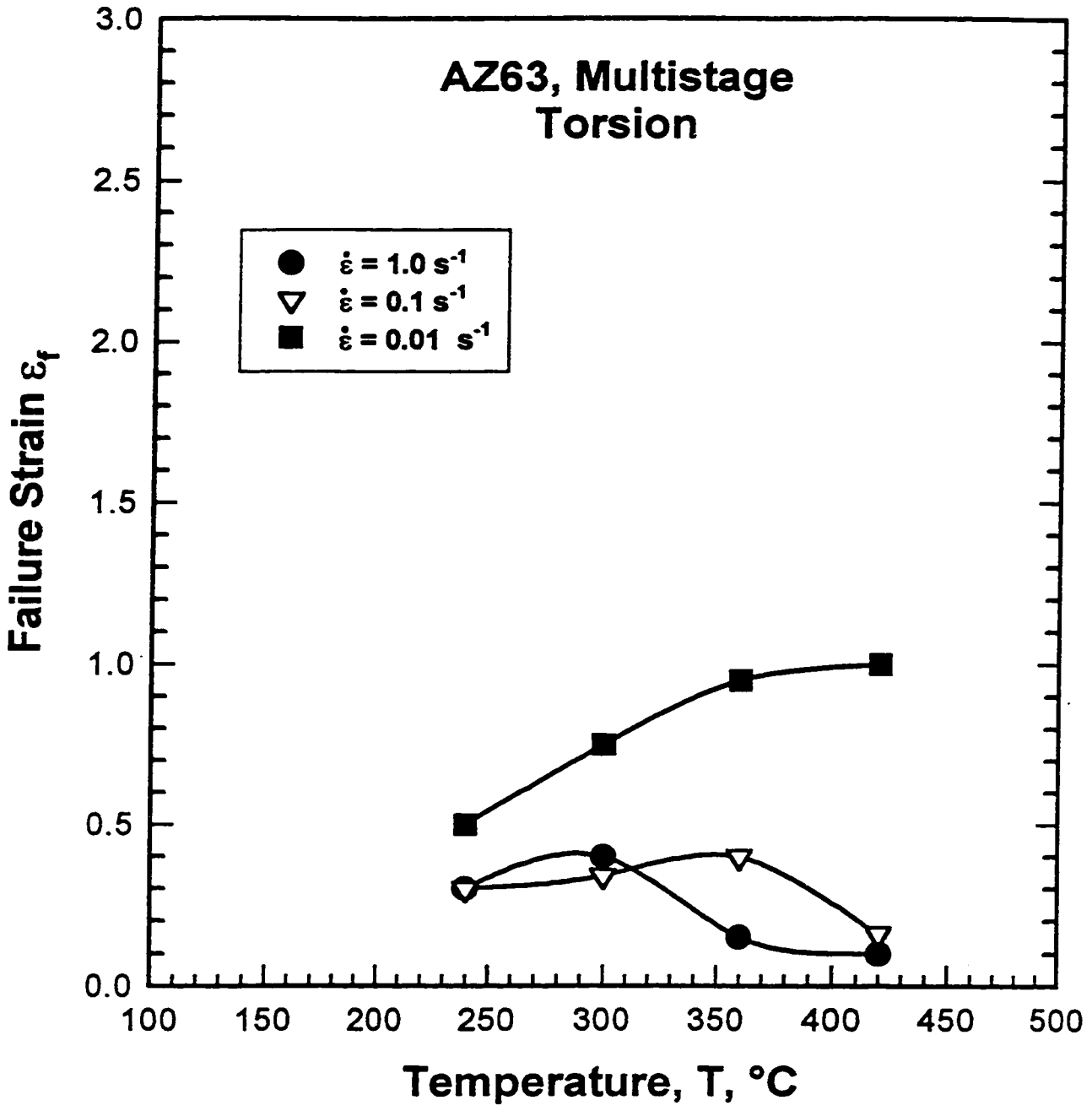

Figure 5.19 Ductility for the alloy AZ63 generally increases with rising temperature and lower strain rate.

5.1.4 Constitutive Plots

The effect of temperature and strain rate on flow stress was analyzed and adequately expressed by Equation 3.5. In the hyperbolic sine analysis, the optimum α should result in the constant temperature lines in plots of log $\dot{\varepsilon}$ versus log sinh($\alpha\sigma$), being close to parallel as shown in Figures 5.20-5.24. However, it is normally the practice to take the value of α for similar alloys as found in the literature in order to facilitate the comparison of the activation energies (Q_{Hw}) and of data by graphical means; a value of α = 0.052 MPa^{-1} was used in the analysis in which the slope n was determined. From the plots of log sinh($\alpha\sigma$) versus 1/T (Figure 5.25-5.29),providing the slope s, Q_{Hw} was calculated from the following relationship:

$$Q_{Hw} = 2.3\ Rns \qquad (5.1)$$

First order regressions were performed on both the constant temperature and constant strain rate data in the two sets of graphs to determine suitable lines and the values of the slopes n and s respectively. The averages of n and s were calculated from the individual slopes and are added to the data as illustrated in Figures 5.20-5.29. It is apparent that the average slopes differ from the best fit lines especially at low temperatures. The separations between some of the data points and the lines indicate experimental error. At low test

temperatures, where there are few active slip systems and the hot working mechanisms are not yet operating, therefore the very low and inconsistent fracture strains cause a large scatter in the maximum flow stress. The values of n, s and Q_{HW} for each material are summarized in Table 5.1. The values n_{av}, r and A, calculated from figures 5.30 and 5.31 are also shown in Table 5.1.

The peak stress data are integrated into a linear dependency on Z which combines the two control variables as a temperature compensated strain rate. The scatter of the data about the line illustrates the quality of the fit which is given by the r values. The slope n is recalculated and differs slightly from the average value. The A values in Equation 3.4 are calculated from the intercepts. The values of n, A and r are reported in Table 5.1.

Table 5.1 Summary of stress exponents (n), slopes (s) and activation energies (Q_{HW}) for magnesium alloys.

Material	$n_{180°C}$	$n_{240°C}$	$n_{300°C}$	$n_{360°C}$	$n_{420°C}$	$n_{450°C}$	**n**(average)
AZ31-Mn	4.20	1.17	2.04	1.80	1.91	2.19	**1.80**
AZ31	1.79	1.64	1.89	1.94	1.99	2.41	**1.90**
AZ91	1.16	1.14	1.04	1.25	1.40	1.73	**1.50**
ZK60	-	2.40	2.33	3.69	2.70	2.19	**2.63**
AZ63	-	1.93	1.99	2.65	-	-	**2.19**

Material	$s_{0.01\ s-1}$	$s_{0.1s-1}$	$s_{1.0s-1}$	**s(average)**	Q_{HW} kJ/mol(2.3Rns)
AZ31-Mn	4.14	3.98	4.03	**4.00**	138
AZ31	3.31	3.49	3.09	**3.30**	130
AZ91★	3.96	4.08	4.09	**4.04**	125
ZK60	3.21	3.19	2.97	**3.15**	140
AZ63	4.40	3.29	2.92	**3.53**	144

Material	Q_{HW} kJ/mol(2.3Rns)	n Z-plot	A Z-plot	r
AZ31-Mn	**138**	1.73	$1.16*10^7$	0.96
AZ31	**130**	1.84	$2.18*10^7$	0.93
AZ91	**125**	1.52	$2.75*10^7$	0.98
ZK60	**140**	2.43	$3.12*10^7$	0.95
AZ63	**144**	2.11	$3.84*10^9$	0.75

★ Tested at $\dot{\varepsilon}$ of 0.05, 0.5 and 5.0 s^{-1}

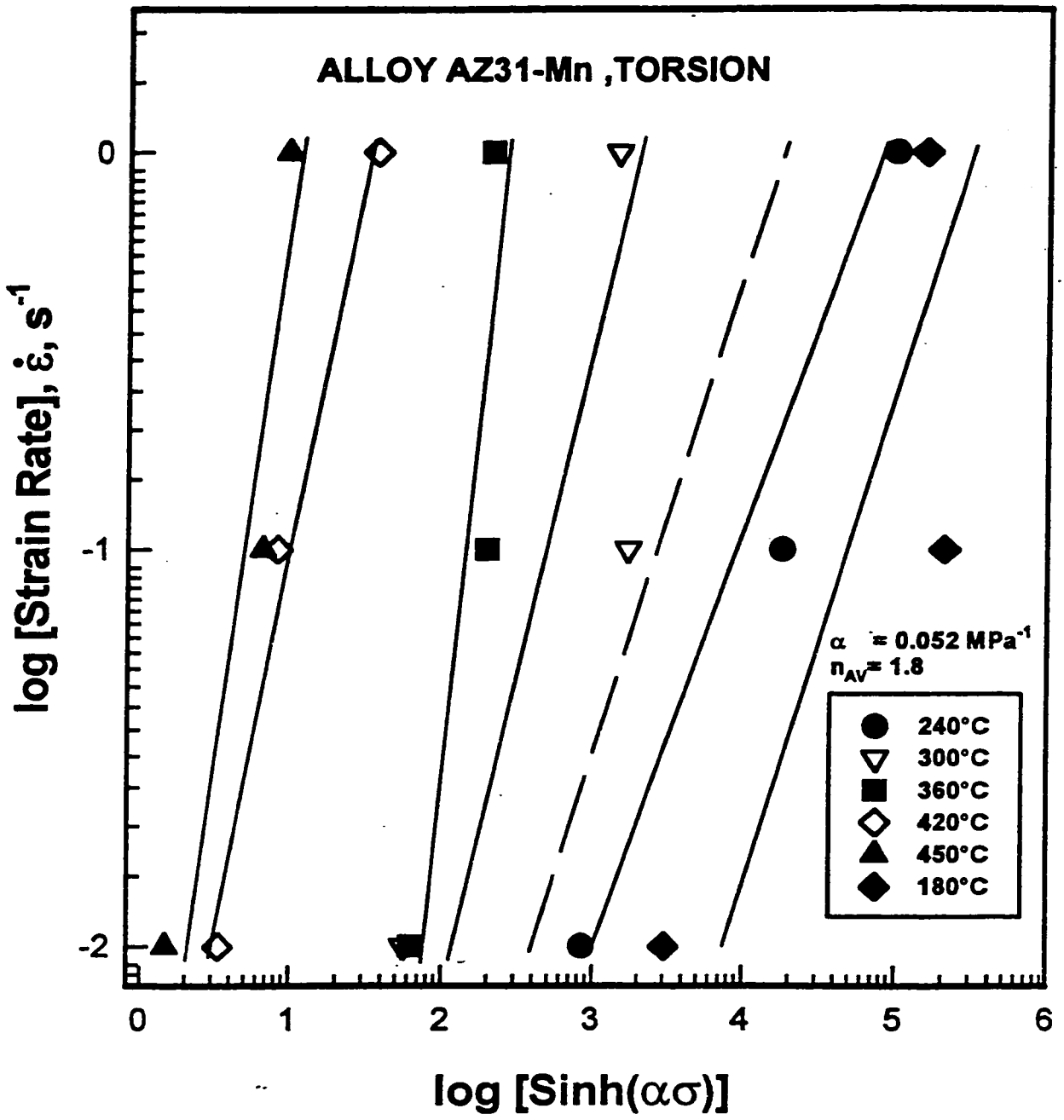

Figure 5.20 Plot of log$\dot{\varepsilon}$ versus log sinh(ασ) (α = 0.052 MPa^{-1}) for the alloy AZ31-Mn. The long dashed line represents the n_{AV}.

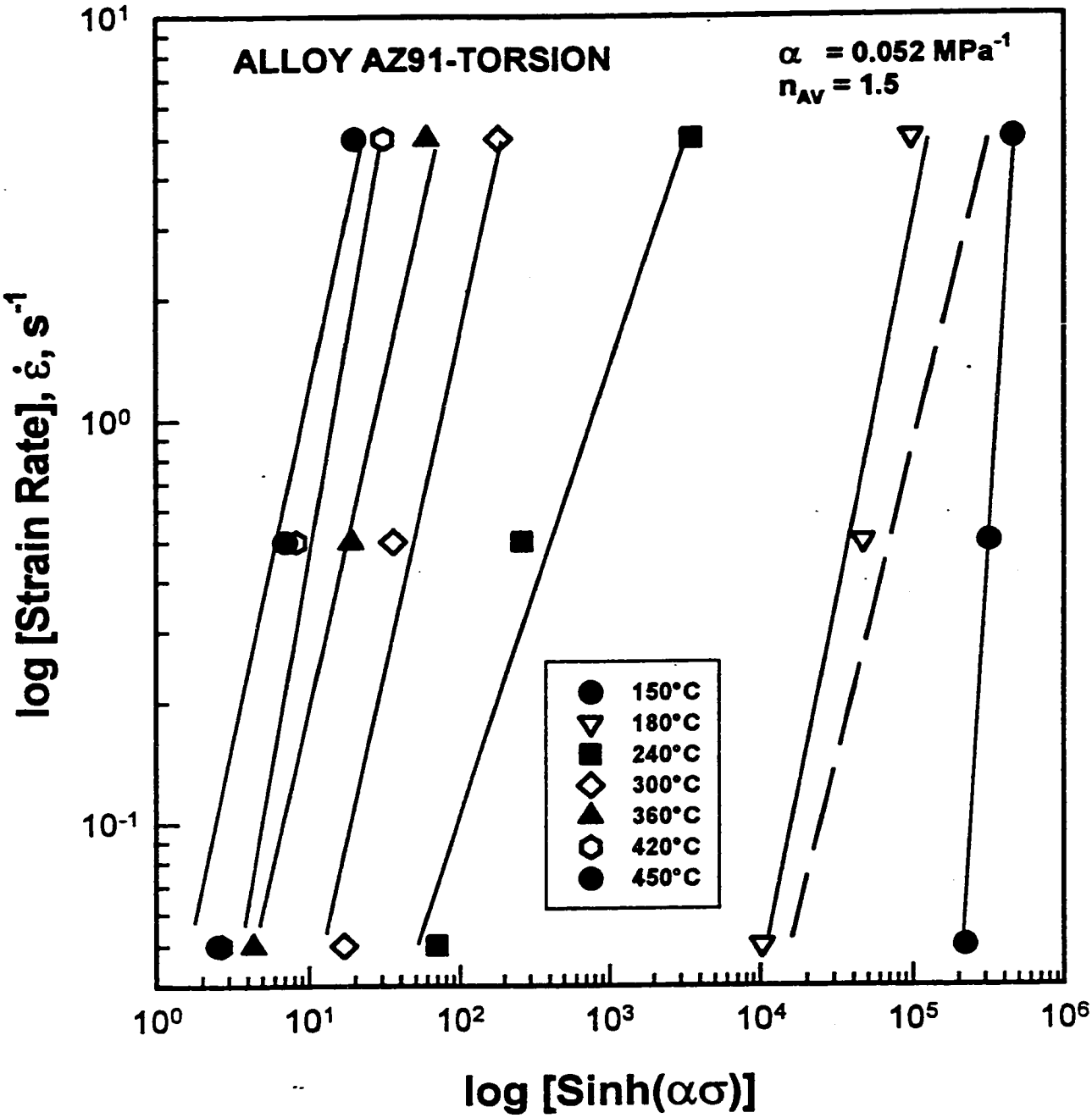

Figure 5.21 Plot of log$\dot{\varepsilon}$ versus log sinh($\alpha\sigma$) (α = 0.052 MPa^{-1}) for the alloy AZ91. The long dashed line represents the n_{AV}.

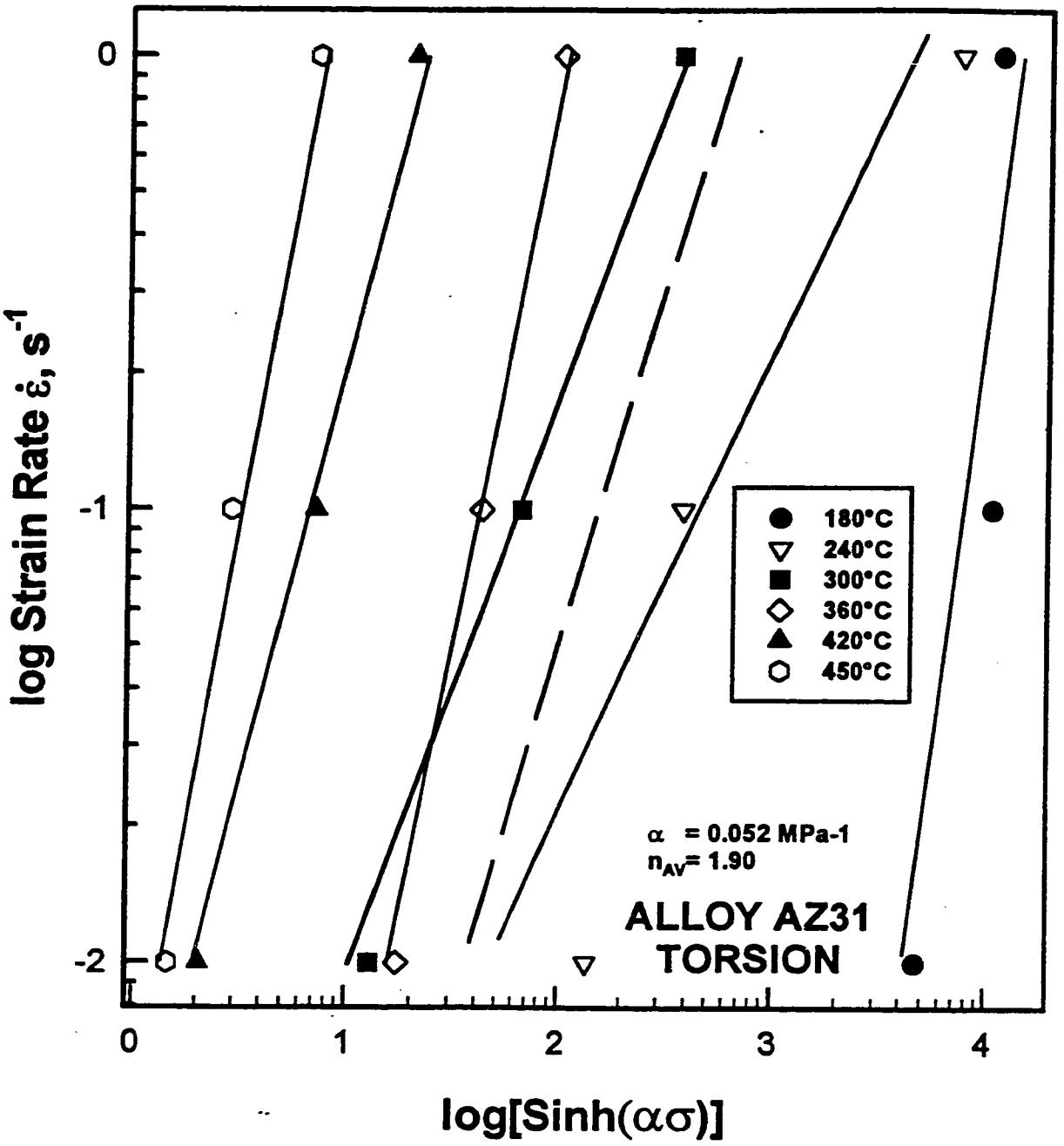

Figure 5.22 Plot of log$\dot{\varepsilon}$ versus log sinh(ασ) (α = 0.052 MPa^{-1}) for the alloy AZ31. The long dashed line represents the n_{AV}.

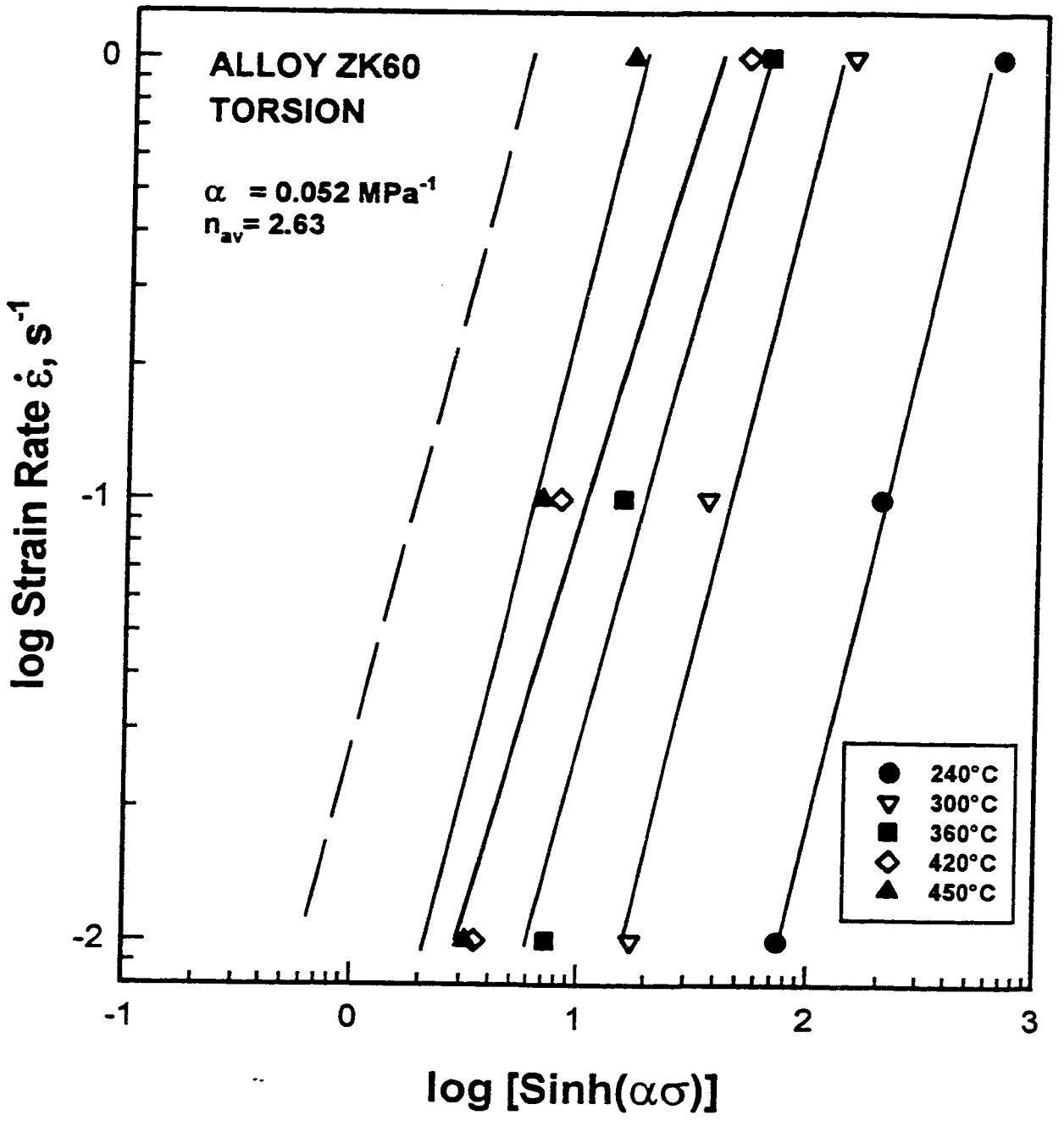

Figure 5.23 Plot of log$\dot{\varepsilon}$ versus log sinh($\alpha\sigma$) (α = 0.052 MPa^{-1}) for the alloy ZK60. The long dashed line represents the n_{AV}.

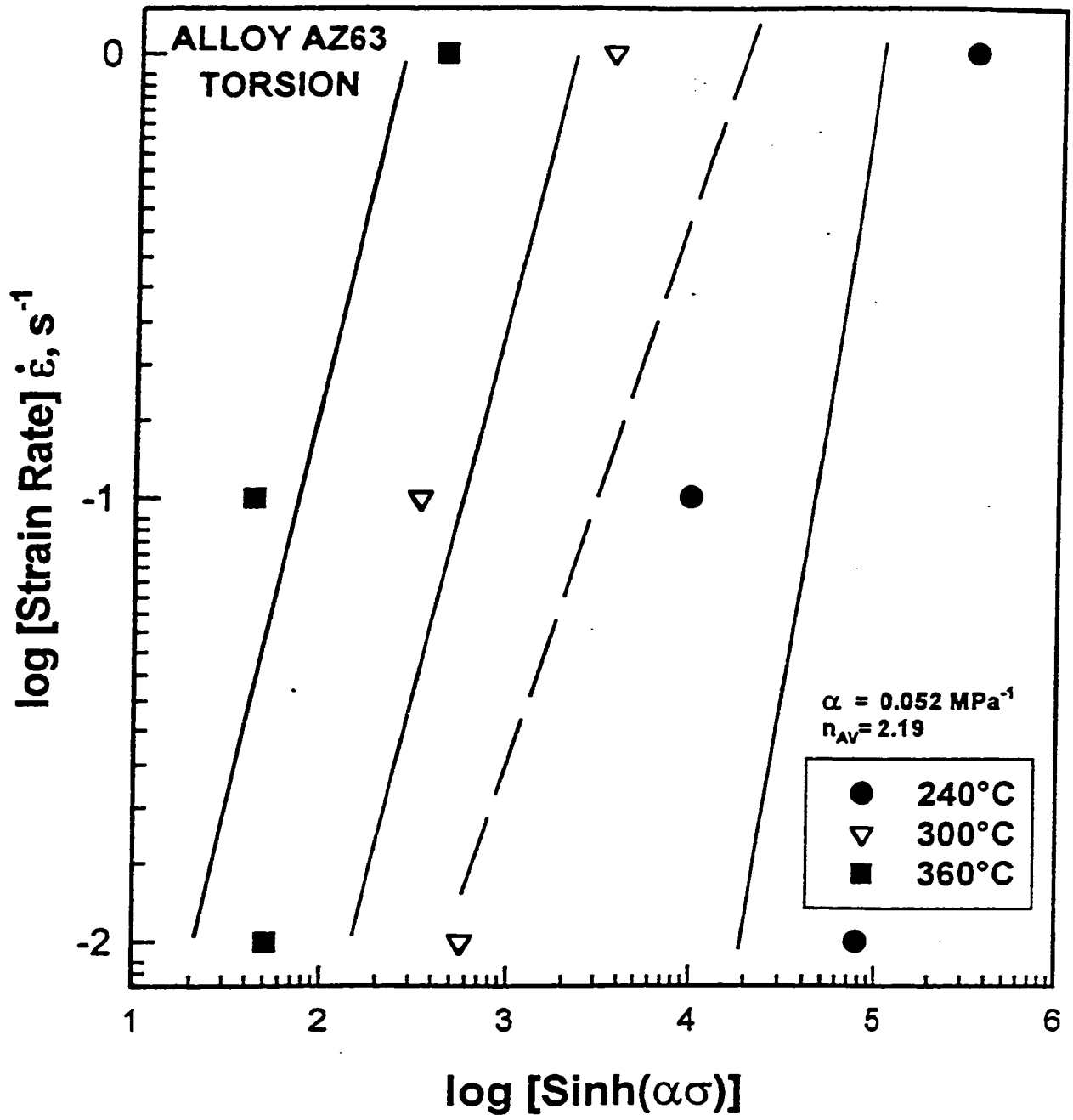

Figure 5.24 Plot of log$\dot{\varepsilon}$ versus log sinh(ασ) (α = 0.052 MPa^{-1}) for the alloy AZ63. The long dashed line represents the n_{AV}.

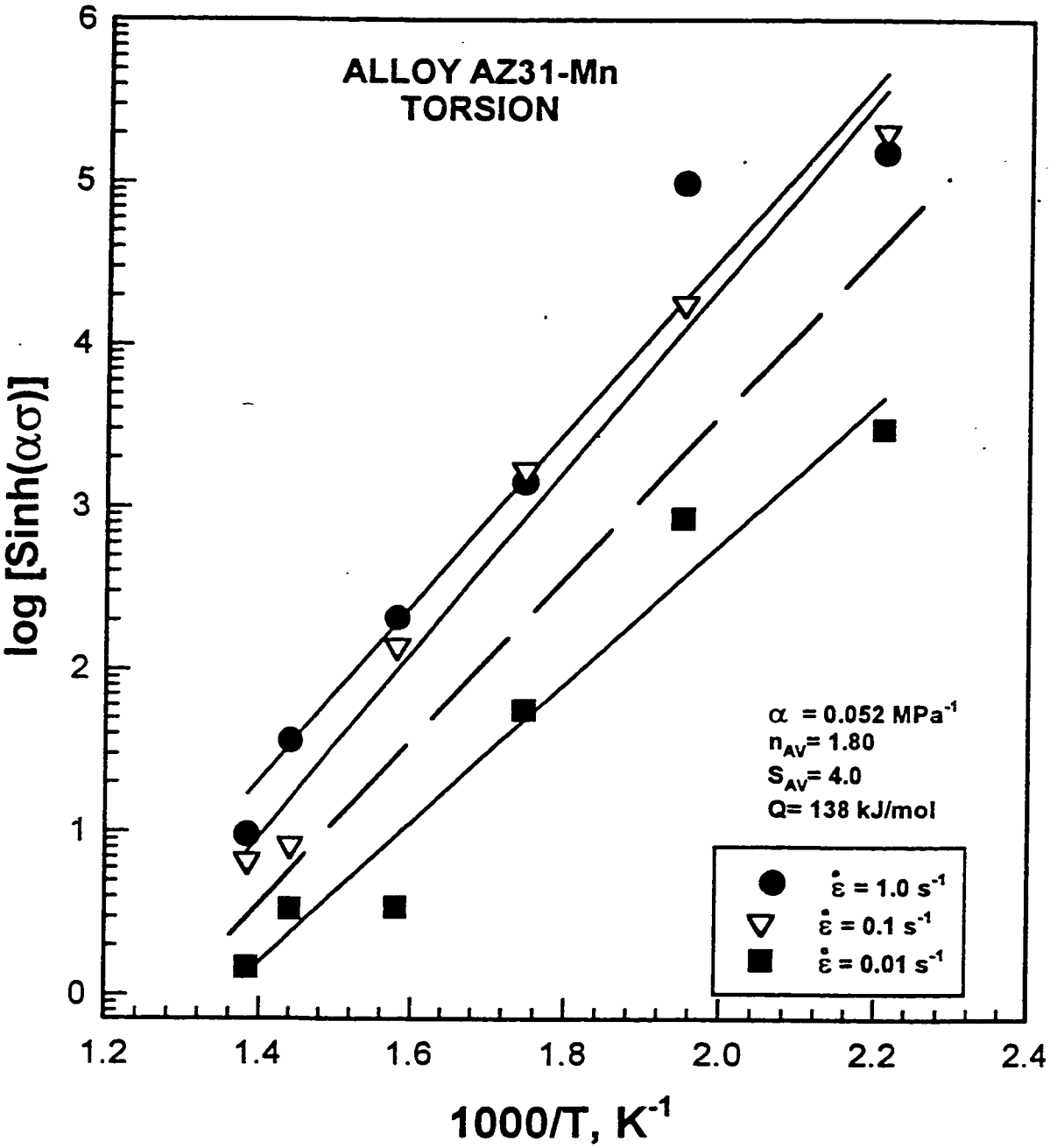

Figure 5.25 Arrhenius relationships linking σ and T suit the data of the alloy AZ31-Mn reasonably well such that straight lines can be drawn and a single Q_{Hw} can be calculated. The long dashed line represents the s_{AV}.

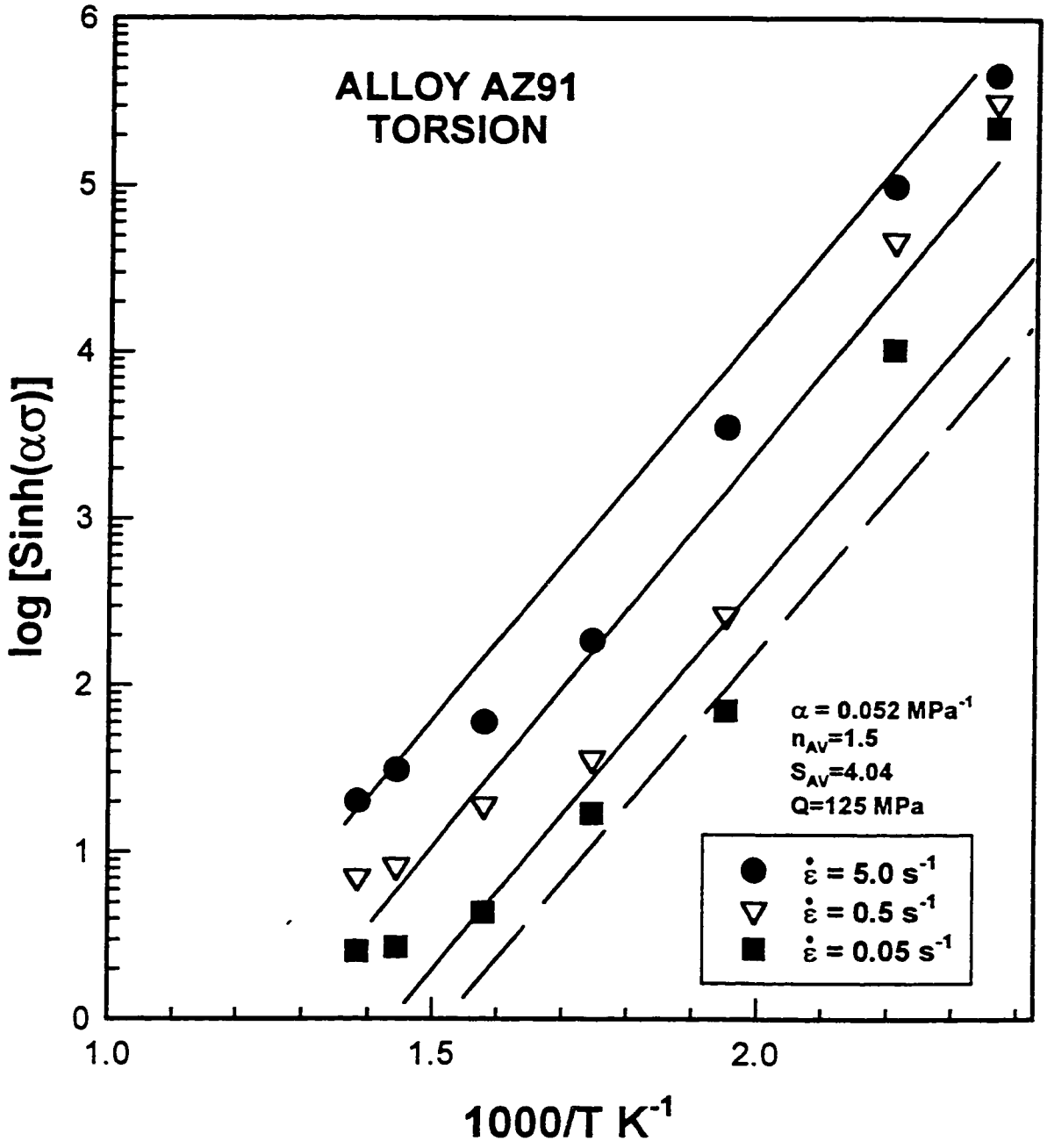

Figure 5.26 Arrhenius relationships linking σ and T suit the data of the alloy AZ91 reasonably well such that straight lines can be drawn and a single Q_{Hw} can be calculated. The long dashed line represents the s_{AV}.

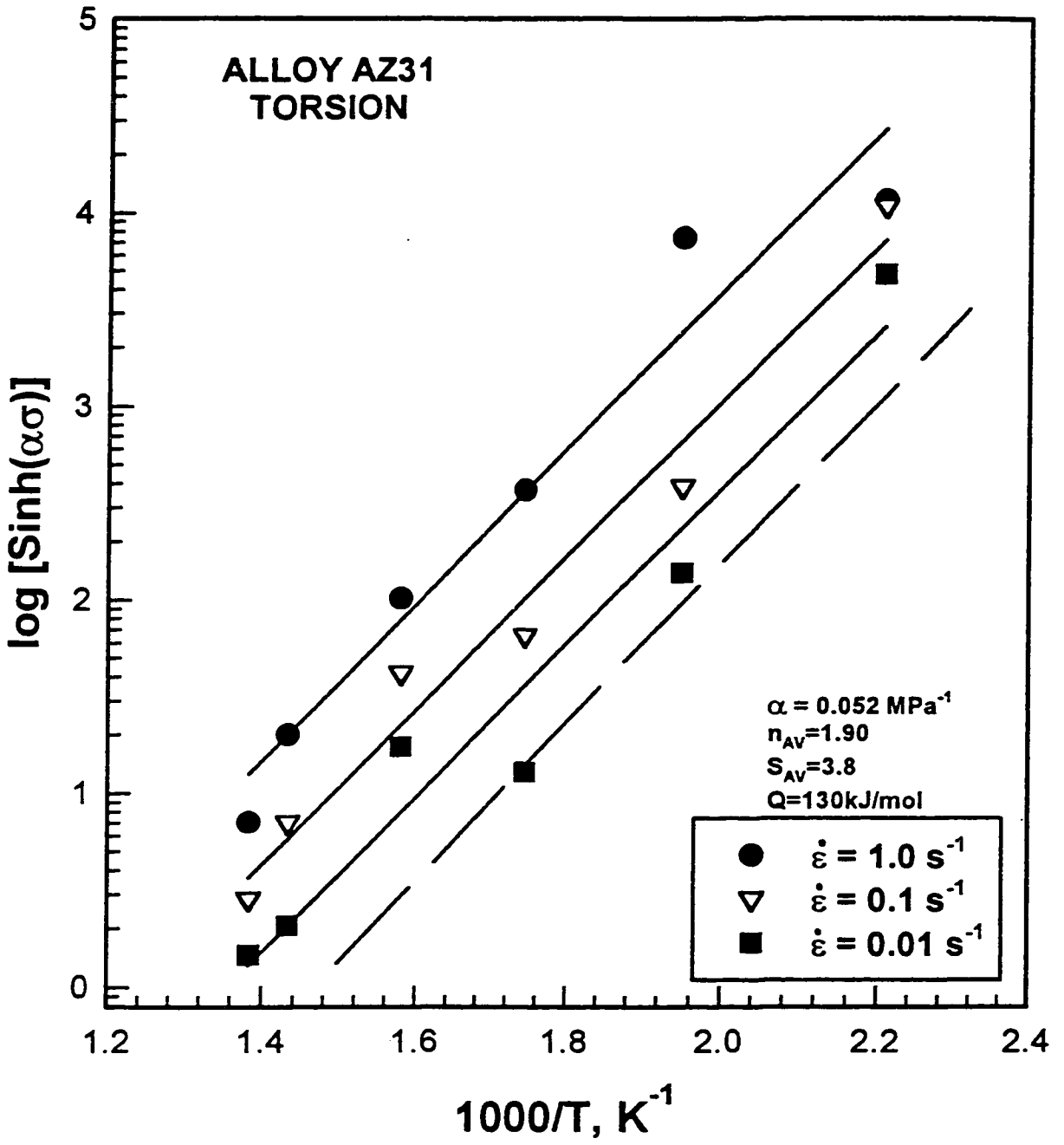

Figure 5.27 Arrhenius relationships linking σ and T suit the data of the alloy AZ31 reasonably well such that straight lines can be drawn and a single Q_{HW} can be calculated. The long dashed line represents the s_{AV}.

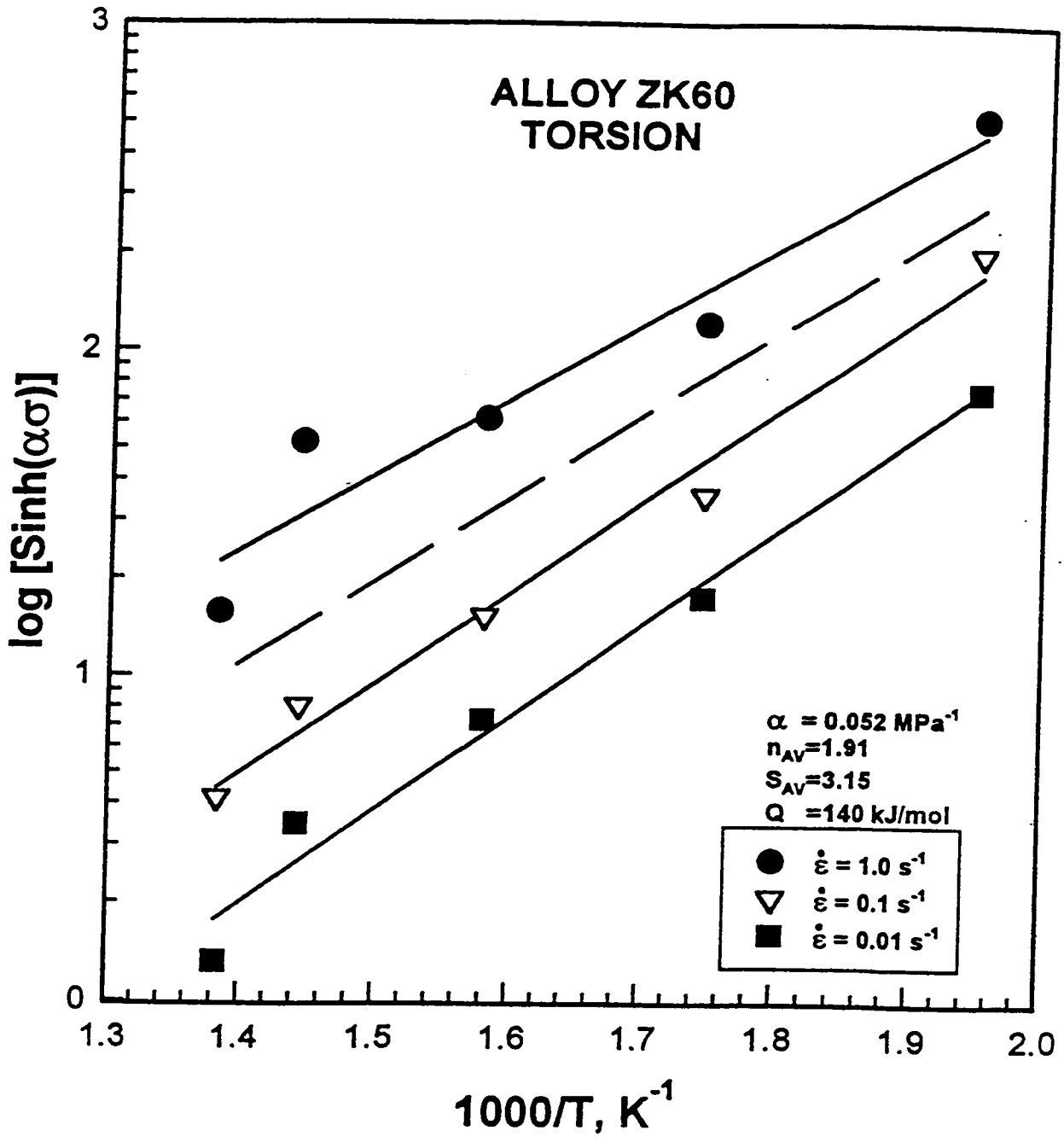

Figure 5.28 Arrhenius relationships linking σ and T suit the data of the alloy ZK60 reasonably well such that straight lines can be drawn and a single Q_{HW} can be calculated. The long dashed line represents the s_{AV}.

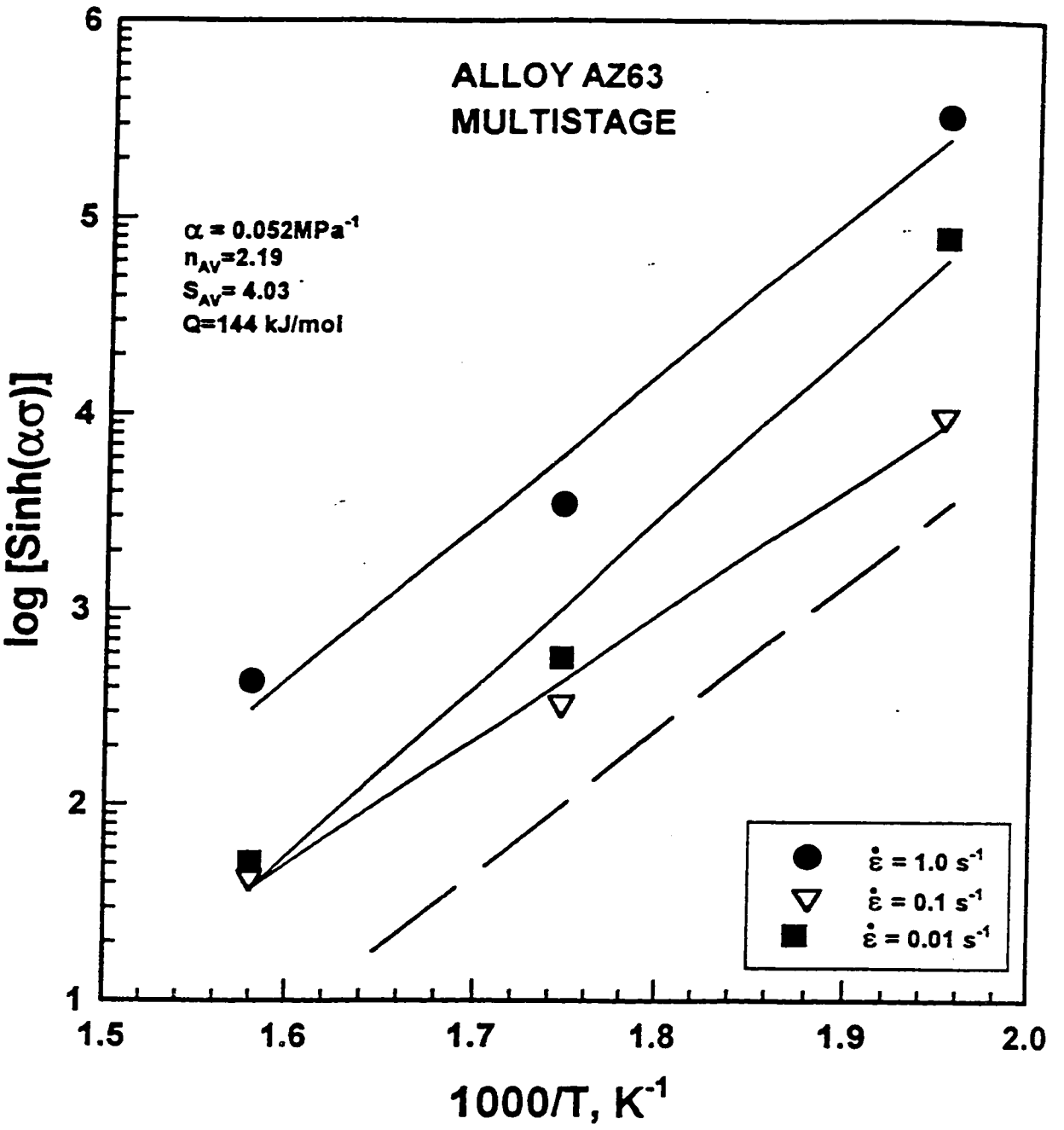

Figure 5.29 Arrhenius relationships linking σ and T suit the data of the alloy AZ63 reasonably well such that straight lines can be drawn and a single Q_{HW} can be calculated. The long dashed line represents the s_{AV}.

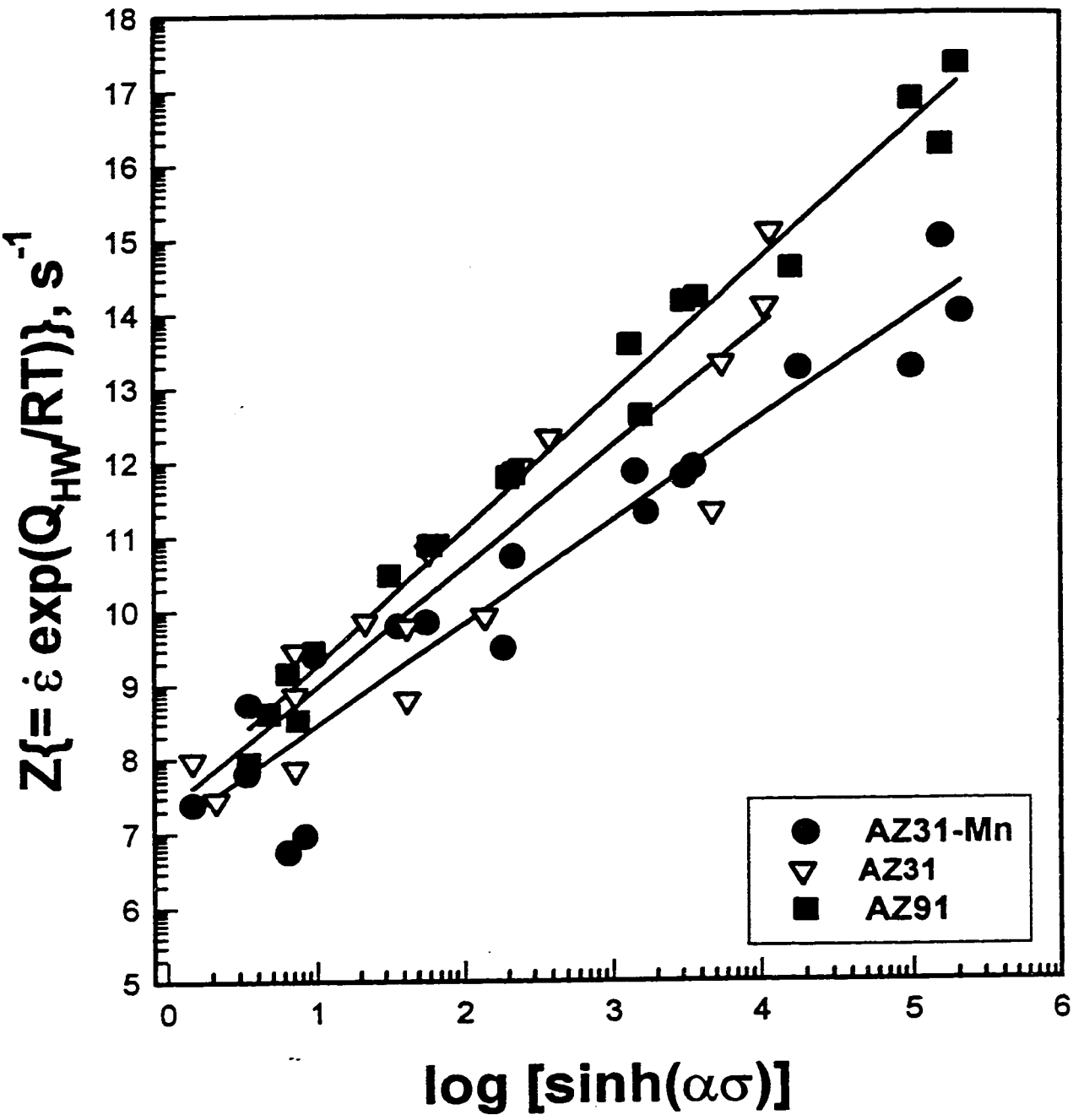

Figure 5.30 Through the use of the Z parameter, the data is organized in a single line. The plots of alloys AZ31-Mn, AZ31 and AZ91 are shown.

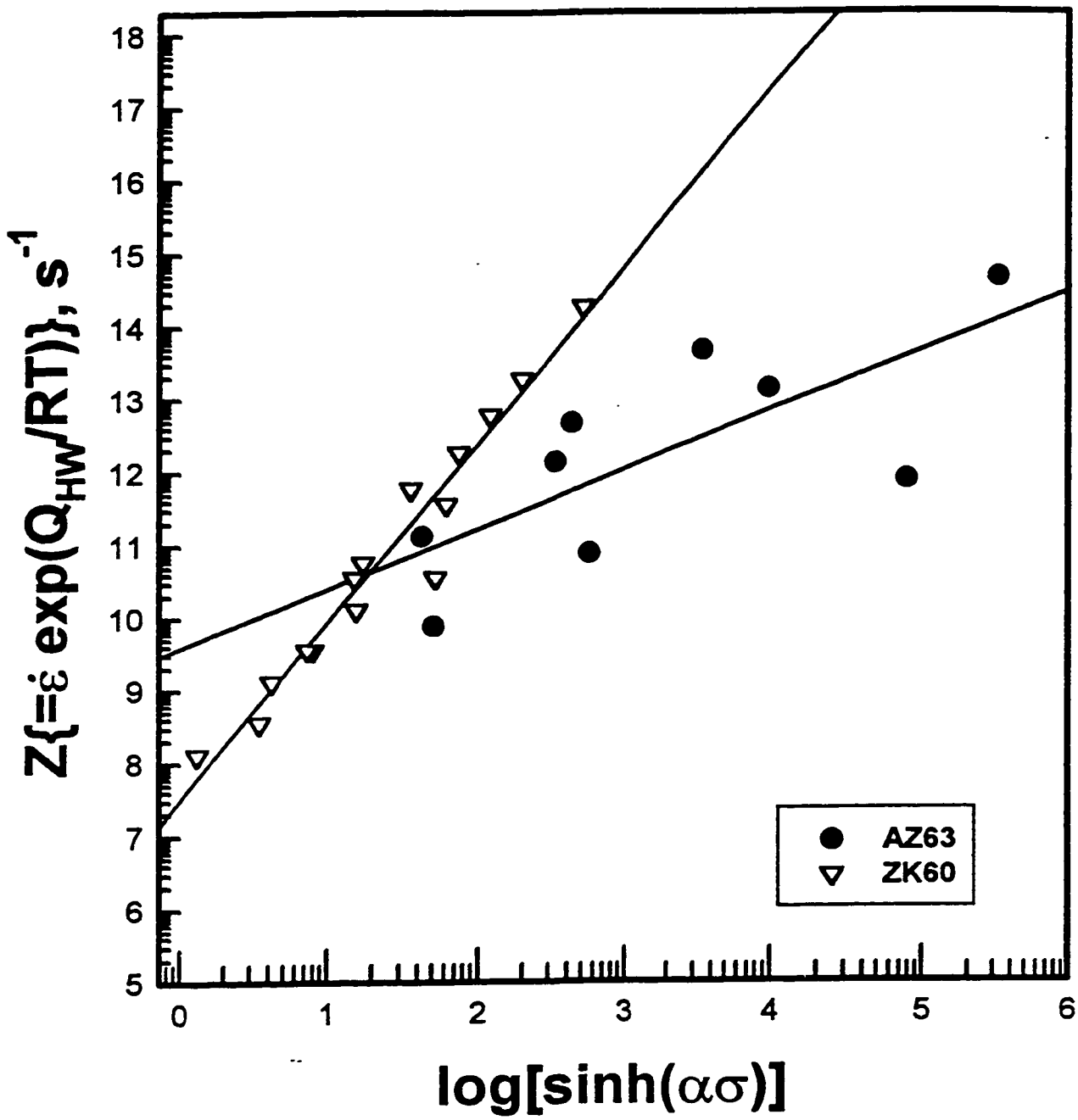

Figure 5.31 Through the use of the Z parameter, the data is organized in a single line. The plots of alloys AZ63 and ZK60 are shown.

5.2. Optical Metallography

5.2.1 Optical Metallography of Alloys AZ31-Mn and AZ31

The microstructural examination was conducted on specimens that had been deformed to fracture. The fracture strain is specified for each micrograph since as T rises the microstructure evolves further during the increased strain as well as due to increase in dynamic restoration. A section normal to the radius and just below the surface is examined in all cases. In some cases the chord sections of the shoulder which is the extension of the tangential section is also presented. In all micrographs the torsion axis is horizontal. The microstructures of AZ31 and AZ31-Mn are described together because the microstructural developments were very similar even though the small difference in composition of the two variants is sufficient to alter the hot strength and constitutive equation.

The microstructures for AZ31 in the high strength (0.52-0.59T_m, melting K) warm working region 180 and 240°C are shown in Figure 5.32. The shoulder exhibits precipitates of 10-20μm at the boundaries of the grains, which are about 200μm diameter. At $\varepsilon_f = 0.5$, the gage grains are visibly elongated and the GB are slightly to strongly irregular. The grains exhibit evidence of twinning which appear as long lenticular regions which are often bent due to the strain subsequent to their formation. The twins intersect each other and distort the GBs. The microstructures of AZ31-Mn are similar but the precipitates are larger and closely spaced along the GB.

For the intermediate region, 300°C (0.66Tm) (Figure 5.33) the strength declines rapidly and ductility rises. At 1.0 s^{-1}, the most noticeable features are the twins which

are similar to those at low T. However along a few GB segments, there are serrations and on others, DRX nuclei are present. Relatively few twins are visible and necklaces of DRX grains appear at GB especially in association with particles, possibly indicating particle stimulated nucleation (PSN). A strong shear band was observed in one specimen. For the low Mn alloy, there is less evidence of twins and more of DRX nuclei.

At 360 and 450°C (0.72-0.83Tm) in the true hot working regime (Figure 5.34), flow stresses are much reduced and ductilities high as a result of more extensive DRX. In most regions there are multiple layers of DRX grains at the original boundaries leaving 30-70% of the centers unaffected. In a few regions DRX has consumed all the initial grains. Increased T results in larger grains (Figure 5.34 (b)) but increased $\dot{\varepsilon}$ has the opposite effect. On many GB at $1s^{-1}$, there are strong serrations without any nuclei. In AZ31-Mn at 360°C, necklaces of DRX grains are prominent. Moreover, at 450°C, there are wider GB layers of DRX grains at 0.1 than at 1.0 s^{-1} but there are no regions where DRX completely filled the grains.

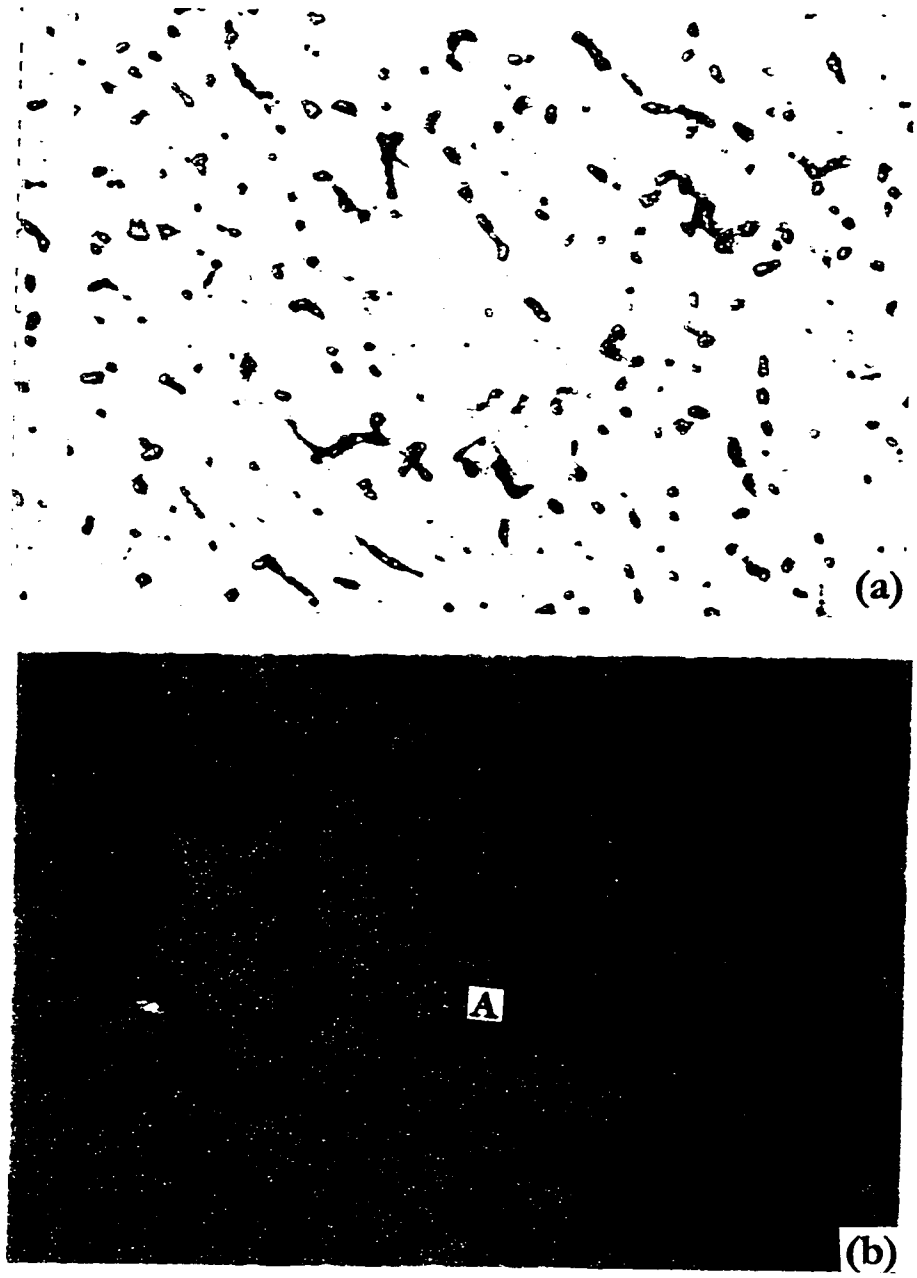

Figure 5.32 Optical micrograph of hot worked AZ31 in the warm working range, i.e. without DRX: a) tangential section of gage at 180°C, $\varepsilon = 0.1\ s^{-1}$, ε_f=0.5, X100 twins are clearly visible in some grains. b) tangential section at 240°C and $\dot{\varepsilon} = 1.0 s^{-1}$ to $\varepsilon_f = 0.2$, X100, twins are observed with poles and precipitates (A) of $Mg_{17}Al_{12}$. The shoulder is relatively twin free.

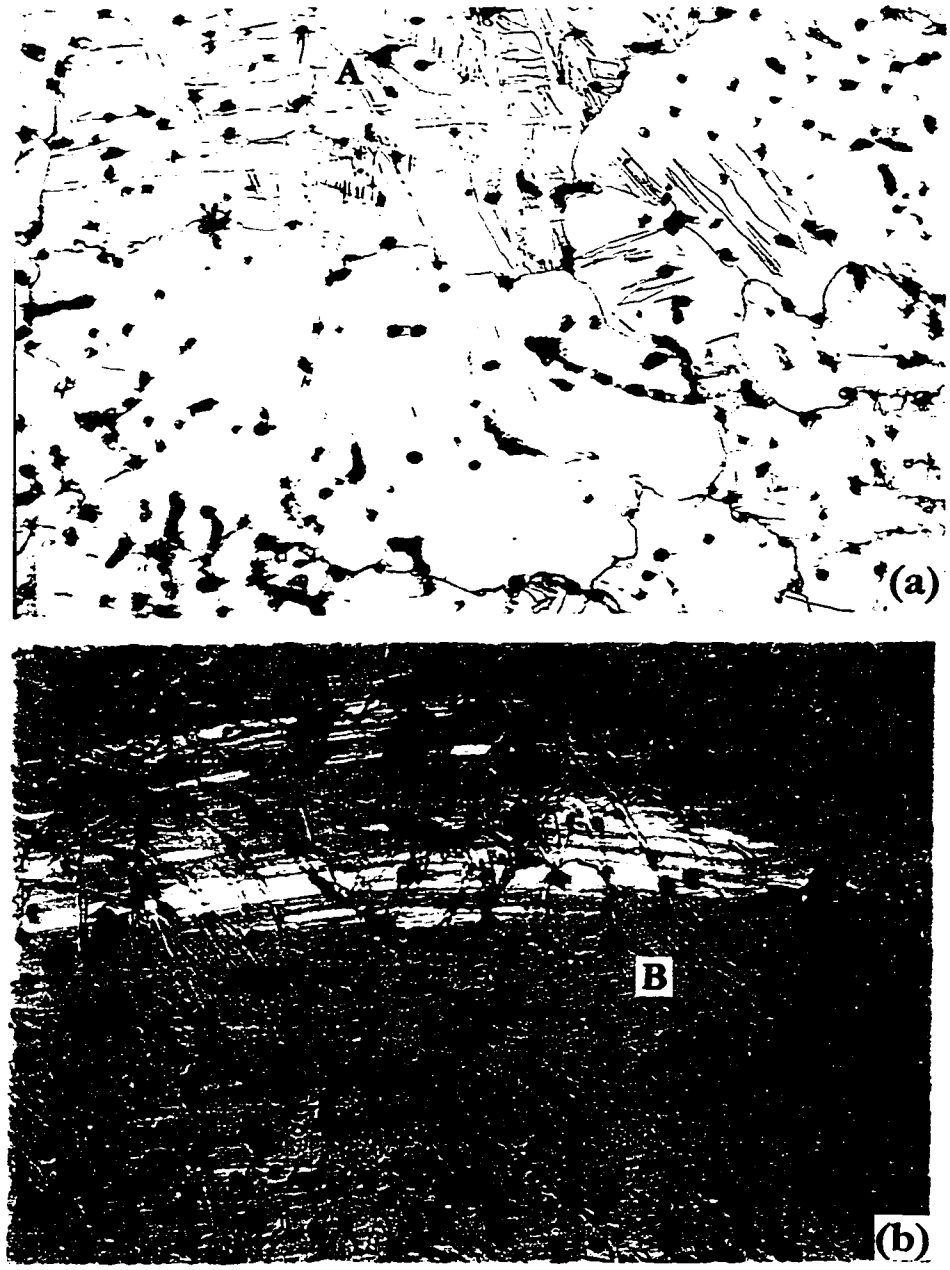

Figure 5.33 Microstructure of AZ31-Mn deformed under intermediate conditions between warm and hot working at 300°C, a) $\dot{\varepsilon} = 1.0s^{-1}$ to $\varepsilon_f = 0.2$, X100, distorted twins (A) are observed to intersect each other and distort some GB; b) $\dot{\varepsilon} = 1.0s^{-1}$ to $\varepsilon_f = 0.2$, X100, highly strained region showing slightly elongated particles with DRX nuclei at particles (PSN) and along serrated GB (B). The new DRX grains are evident along twin boundaries.

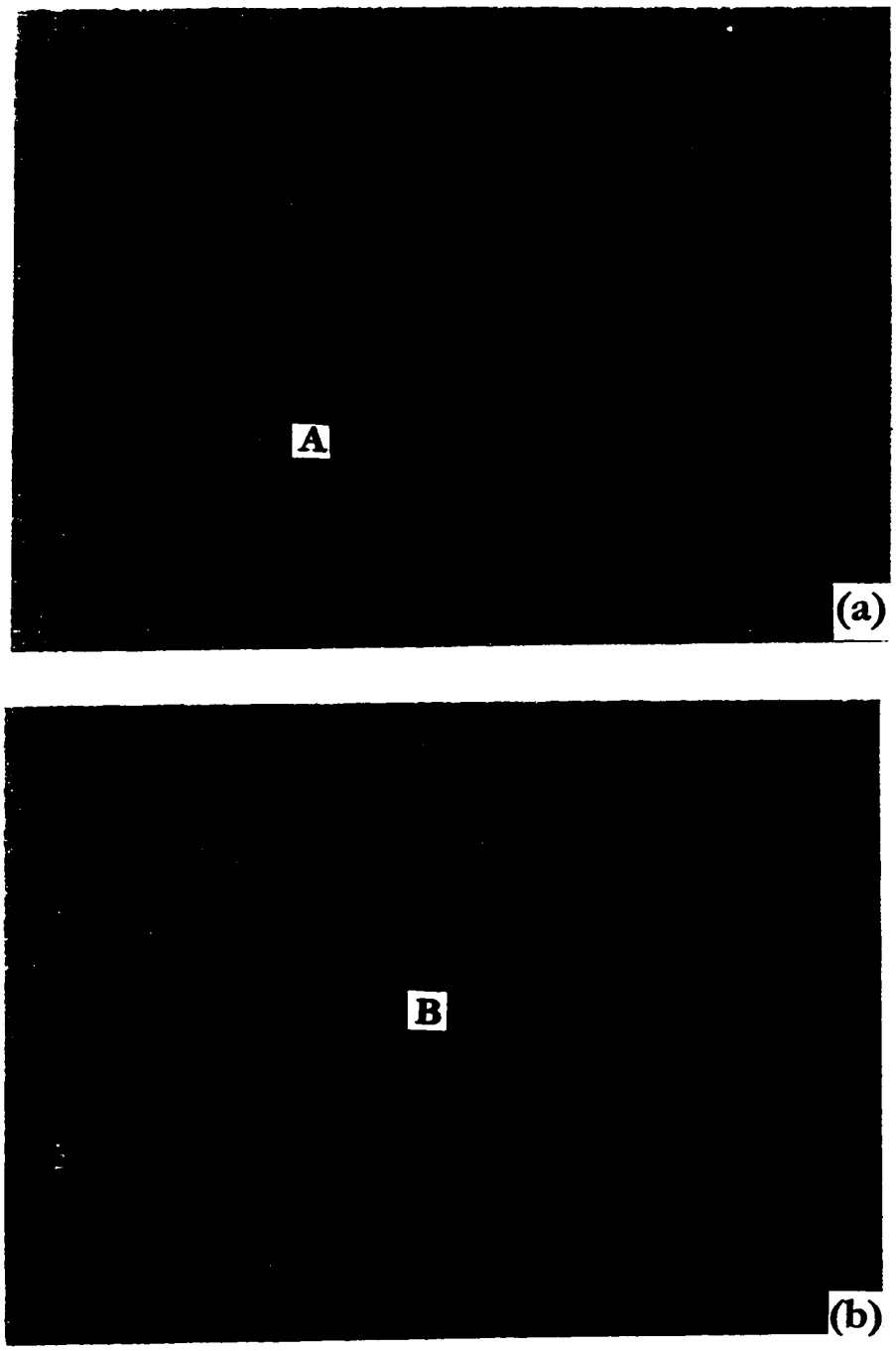

Figure 5.34 Microstructure in tangential gage section of a) AZ31-Mn at 360°C, $\dot{\varepsilon} = 0.1\ s^{-1}$, $\varepsilon_f = 0.87$, X100, after hot working. DRX grains (A) mainly along GB but also in patches of completion b) AZ31 450°C, $\dot{\varepsilon} = 0.1\ s^{-1}$, $\varepsilon_f = 1.80$, X200, showing the new DRX grains which have completely consumed the old grains (B).

5.2.2 Optical Metallography of Alloy AZ91

Optical micrographs of AZ91 (Mg-9.1Al-0.7Zn-0.13Mn) are shown in Figures 5.35-5.37. The as-received structure was generally uniform consisting of massive $Mg_{17}Al_{12}$ compound at the boundaries of small cored grains. At low test temperatures between 180-240°C, the massive $Mg_{17}Al_{12}$ compound can be seen uniformly distributed along the grain boundaries; in some regions it can be seen as a dark phase. The twins are observed but cannot be seen clearly as in AZ31-Mn due to the smaller grains and the more extensive presence of the $Mg_{17}Al_{12}$ at the GBs.

The alloy was subjected to a prior TMP at 300°C to a total strain of 0.2 in order to prevent hot-shortness. In the intermediate temperature region (360°C) the new DRX grains can be clearly seen as the $Mg_{17}Al_{12}$ has segregated and appears as the dark phase. Grains poorly oriented for slip develop twins which are suitably oriented.

In the true hot working regime (0.66Tm, K) the flow stresses are minimal with high ductility as a result of extensive DRX. In most regions the new grains have covered the entire area (Figure 5.37).

Figure 5.35 The as-cast microstructure of alloy AZ91 before heating X400

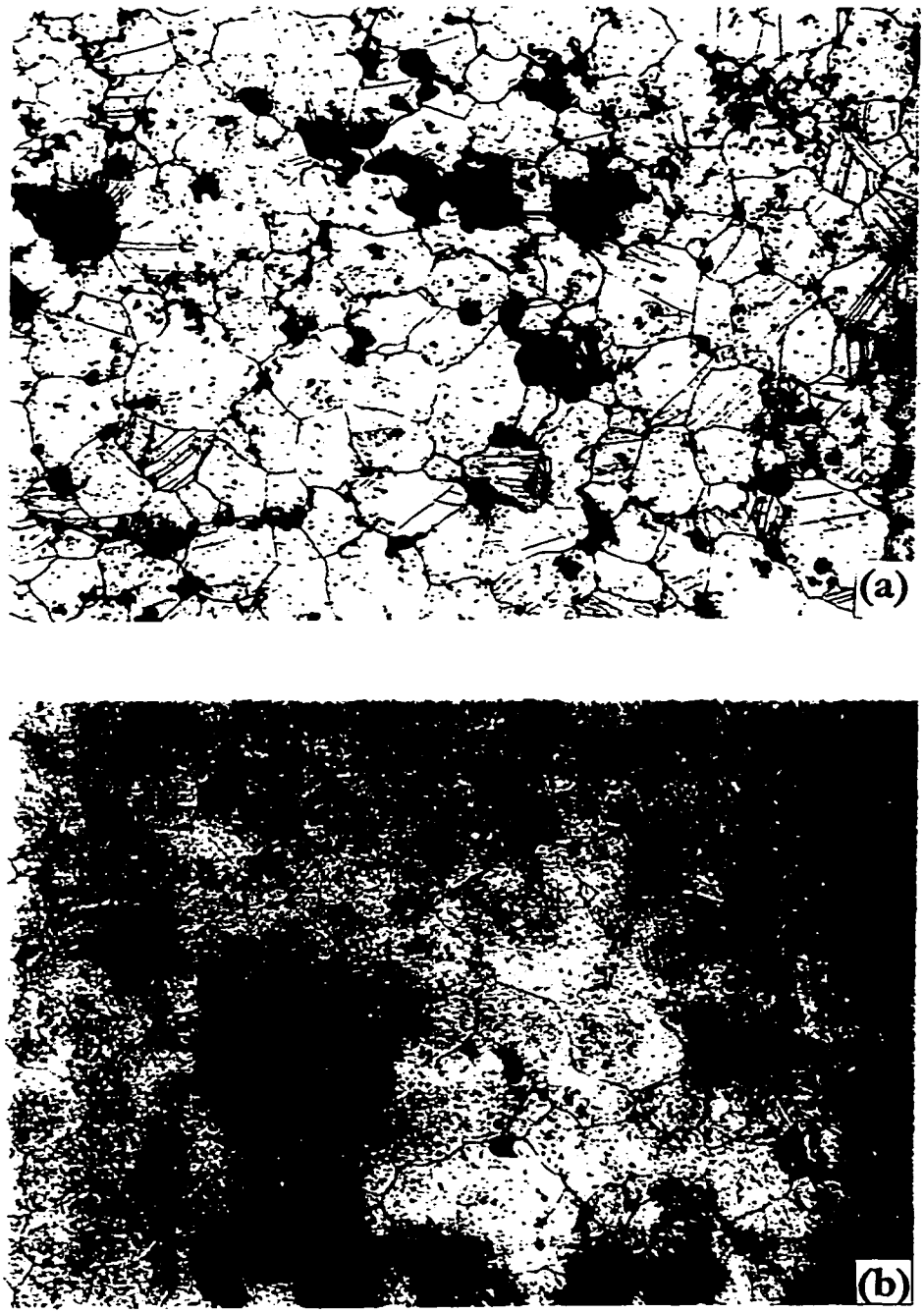

Figure 5.36 a) Microstructure in tangential gage section of alloy AZ91 at 300°C, $\dot{\varepsilon} = 5.0\ s^{-1}$, $\varepsilon_f = 1.35$, X200. The twins are clearly visible and the dark phase is $Mg_{17}Al_{12}$; b) there are no twins in the shoulder section for the same test conditions as in (a).

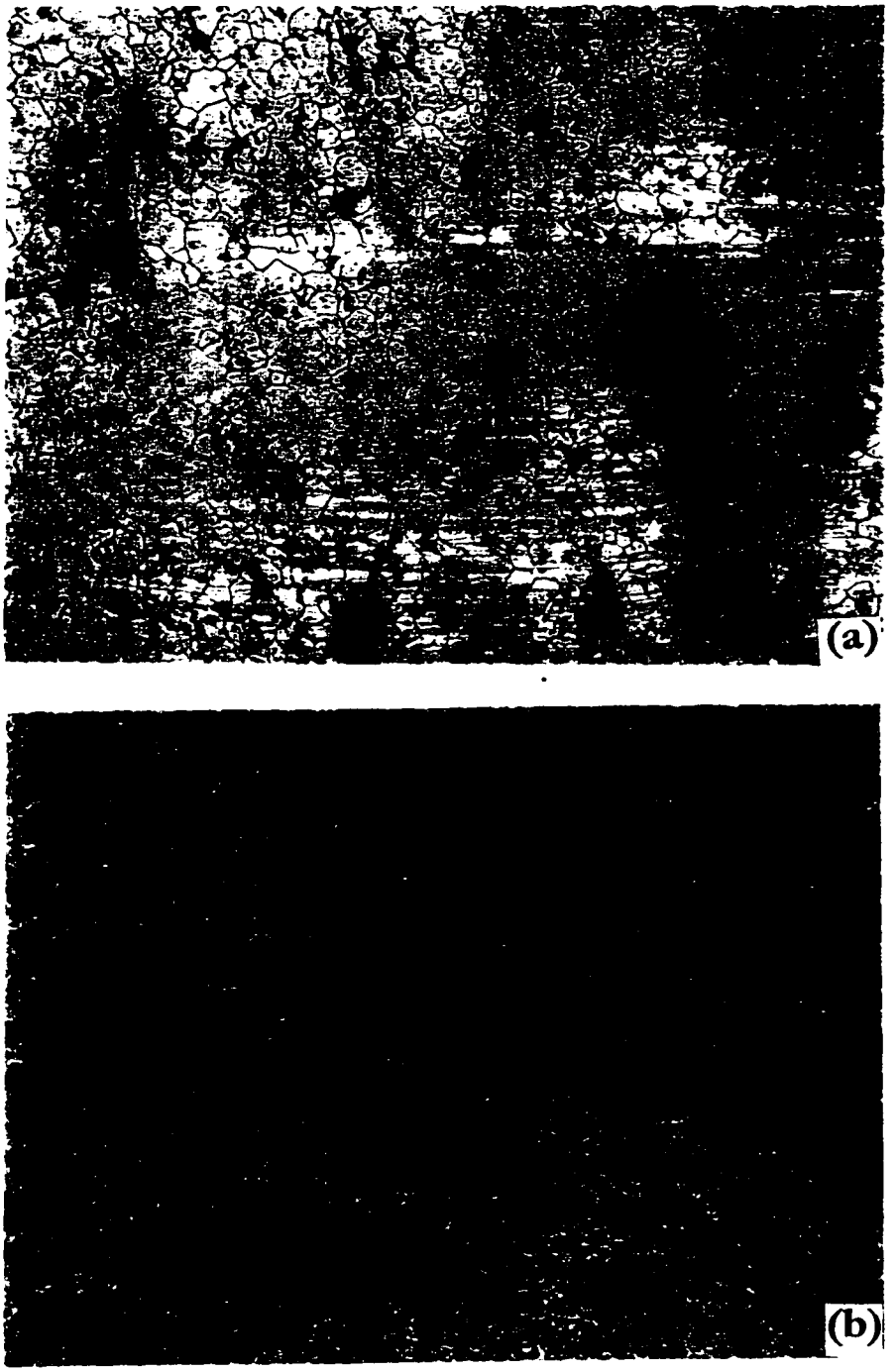

Figure 5.37 Optical micrographs of hot worked AZ91 in the true hot working range, i.e. at 450°C, $\dot{\varepsilon} = 5.0\ s^{-1}$ $\varepsilon_f = 1.35$, X200. a) The small DRX grains have spread throughout the gage section, however these are after TMP to refine grains; b) the shoulder section is shown in (a).

5.2.3 Optical Metallography of Alloy ZK60

The microstructures for ZK60 in the high strength (0.52-0.59T_m) warm working region 180 and 240°C are shown in Figures 5.38 and 5.39(a). This alloy shows very limited precipitates compared to the Al bearing alloys. The lightly strained grains exhibit evidence of twinning which appears as long lenticular regions which are often bent due to the strain subsequent to their formation. The twins intersect each other and distort the GBs. There are also slip bands inside the twins. As the strain rate increases there is an increase in the density of the twins and the spread of the twinned regions.

In the intermediate region, 300°C (0.66Tm), particularly at 0.1 and 0.01 s^{-1} (Figure 5.39(b)), the alloy strength declines while ductility rises noticeably. At 1.0 s^{-1} (Figure 5.40(b)), the most marked feature are the twins which are similar to those observed at low T; however, along a number of GB segments DRX nuclei are present and can be seen as necklaces. Nucleation where twins were observed indicates strain concentration in the twin regions, particularly at intersections. As the strain rate decreases from 1.0 s^{-1} ε_f = 0.2 (Figure 5.39(b)) to 0.01 s^{-1} ε_f = 0.4 (Figure 5.40 (b)) there is an increase in the density of the new DRX grains.

At 360 and 450°C (0.72-0.83Tm) in the true hot working regime (Figure 5.41), flow stresses are much reduced and ductilities much improved as a result of more extensive DRX. In most regions there are multiple layers of DRX grains at the original boundaries leaving 10-40% of the centers unaffected. In many regions DRX has consumed all the initial grains.

Increased T results in larger grains (Figure 5.42). The new grains grow in the deformed area and along old grain boundaries elongated in the direction of deformation.

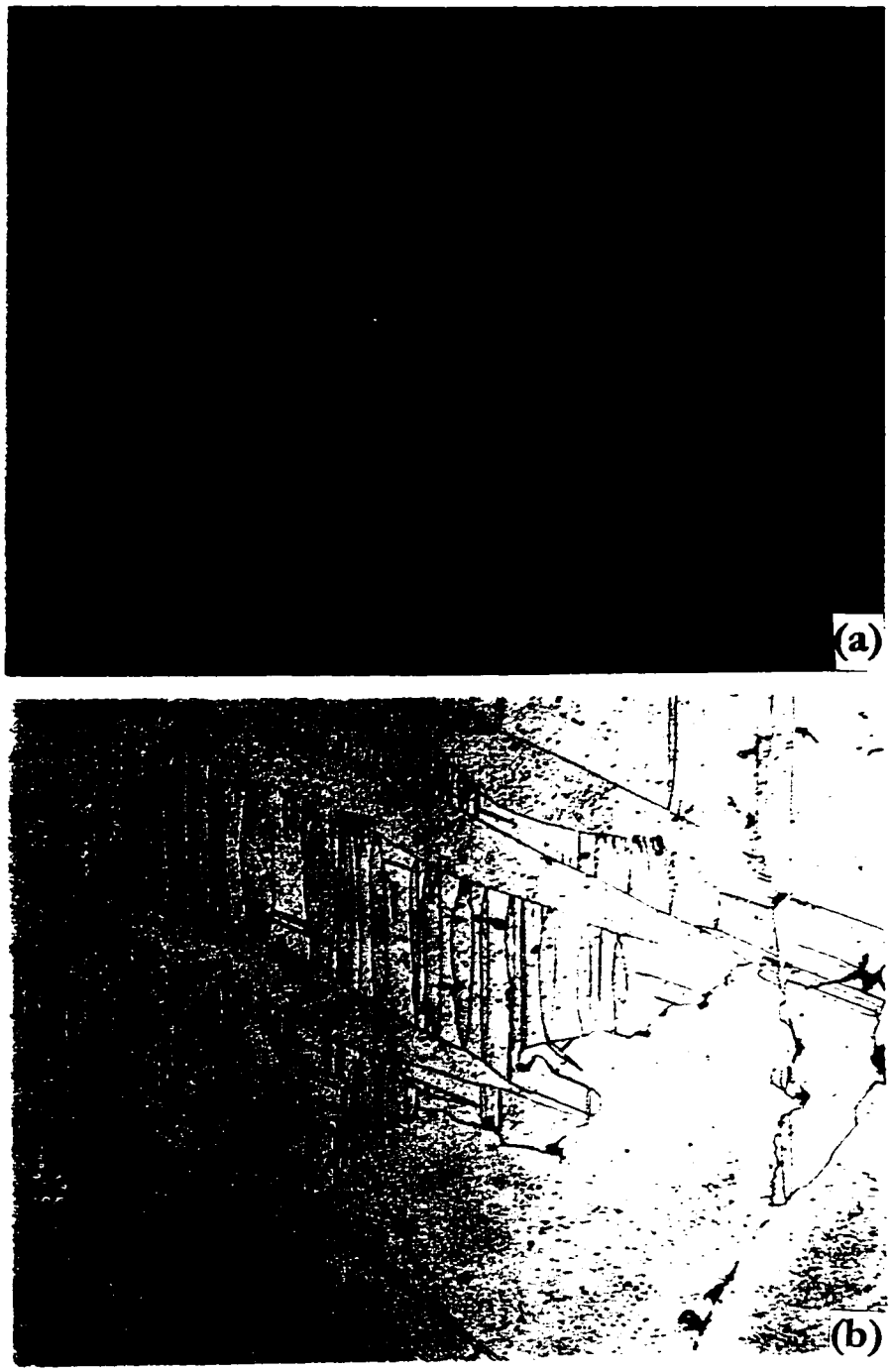

Figure 5.38 Micrograph of alloy ZK60 at 240°C, a) $\dot{\varepsilon} = 1.0\ s^{-1}$, $\varepsilon_f = 0.10$, X200, Twins can be seen in the gage area (right), while the shoulder (left) remains undeformed; b) $\dot{\varepsilon} = 0.1\ s^{-1}$, $\varepsilon_f = 0.15$, X200. Twins bands have formed in the highly deformed region.

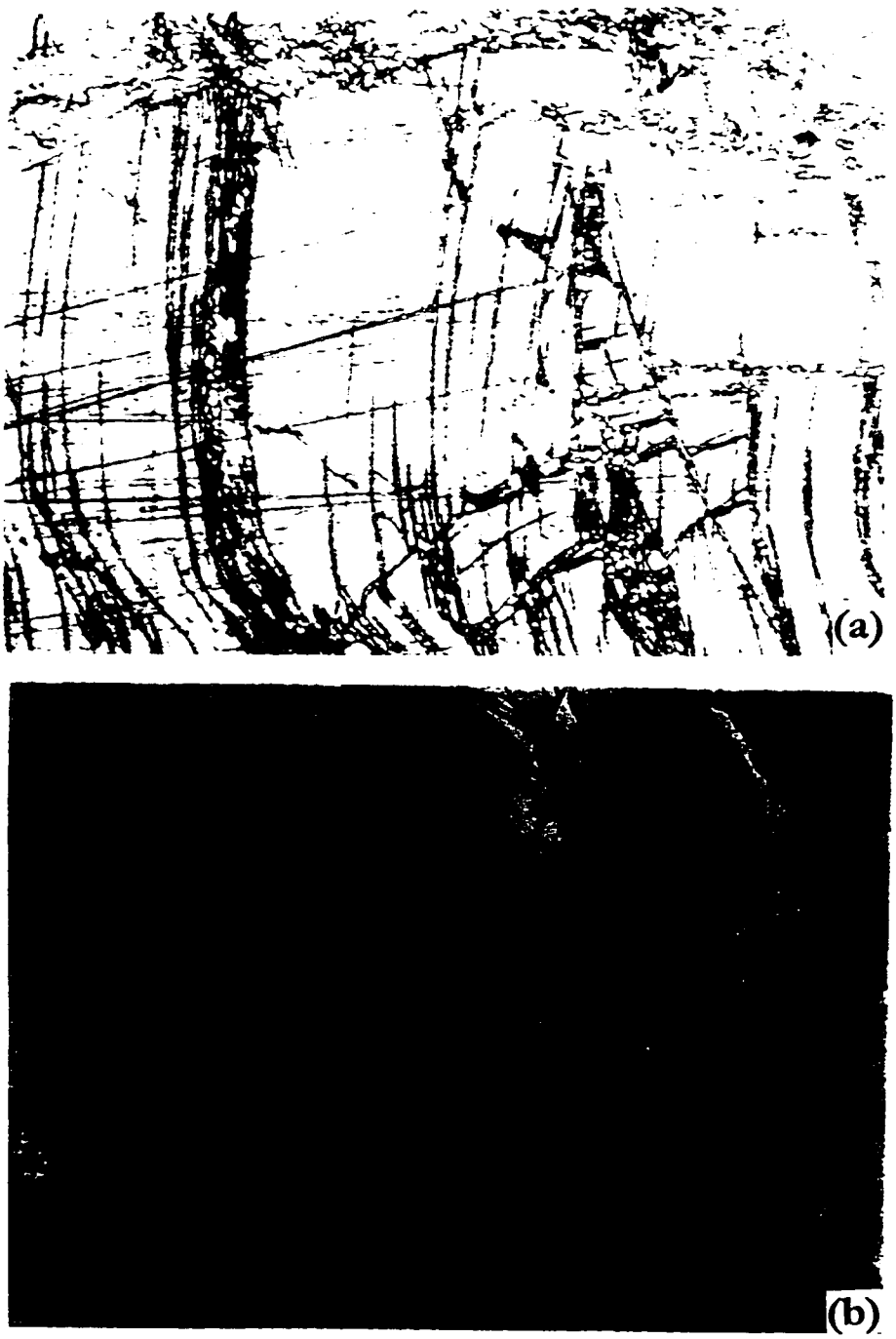

Figure 5.39 Micrograph of alloy ZK60 at a) 240°C, $\dot{\varepsilon}$ = 0.01 $s^{-1}\varepsilon_f$ = 0.20, X200 The new grains can be clearly seen along the twin boundaries. There also appears to be new grains along some grain boundaries; b) at 300°C, $\dot{\varepsilon}$ = 1.0 s^{-1}, ε_f = 0.20, X400. The new grains which formed along the twin boundaries principally at intersections are evident.

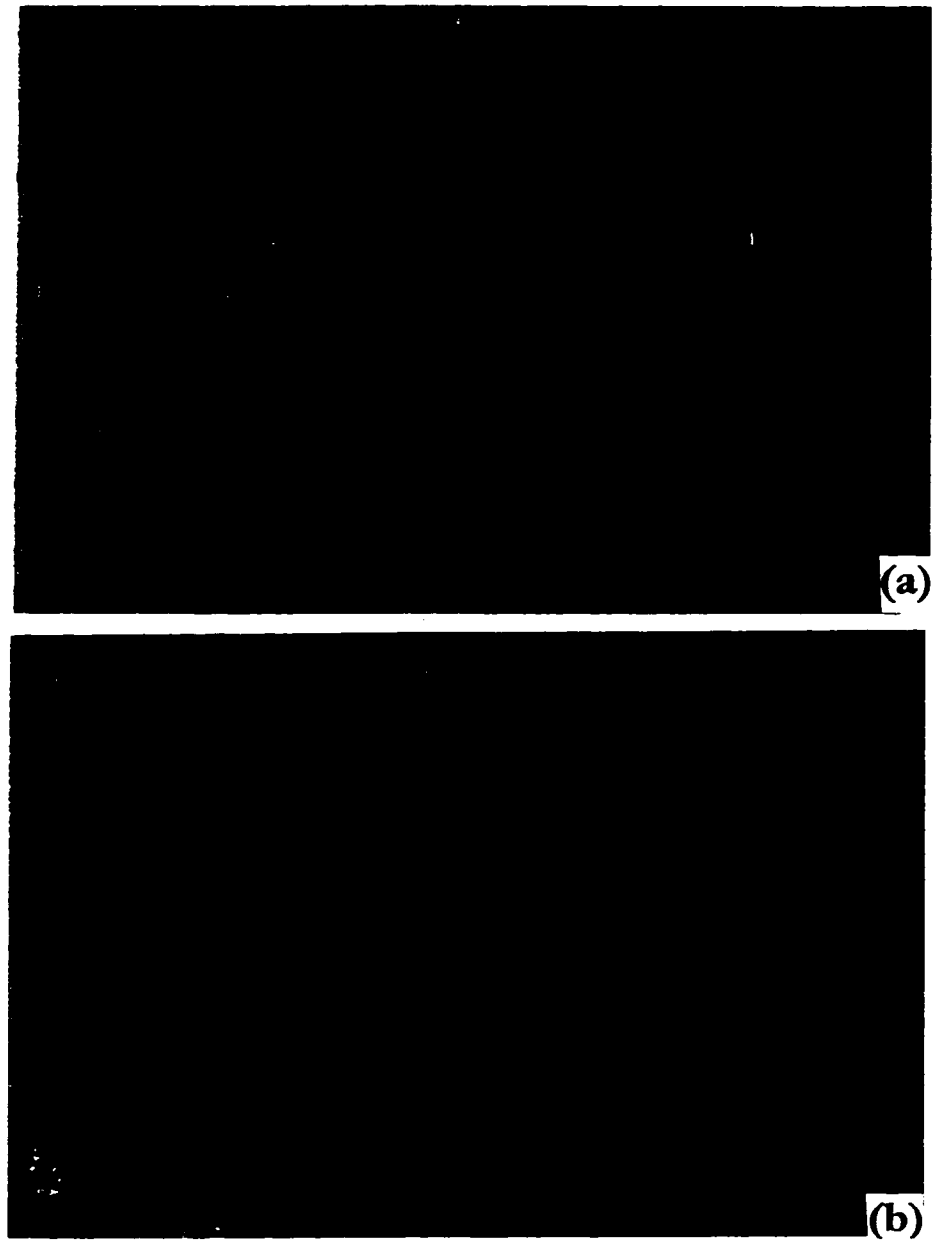

Figure 5.40 Micrograph of alloy ZK60 at 300°C, a) $\dot{\varepsilon} = 0.1\ s^{-1}$, $\varepsilon_f = 0.23$, X200. The shoulder region with undeformed grains can be clearly seen on the left hand side while the gage section (right) shows new DRX grains formed along the twin and grain boundaries; b) tangential gage section, $\dot{\varepsilon} = 0.01\ s^{-1}$, $\varepsilon_f = 0.28$, X200. Chains of new DRX grains are evident along twin boundaries. Serrations along GBs serve as nuclei sites for the grains that have formed and grains appear very elongated at the left.

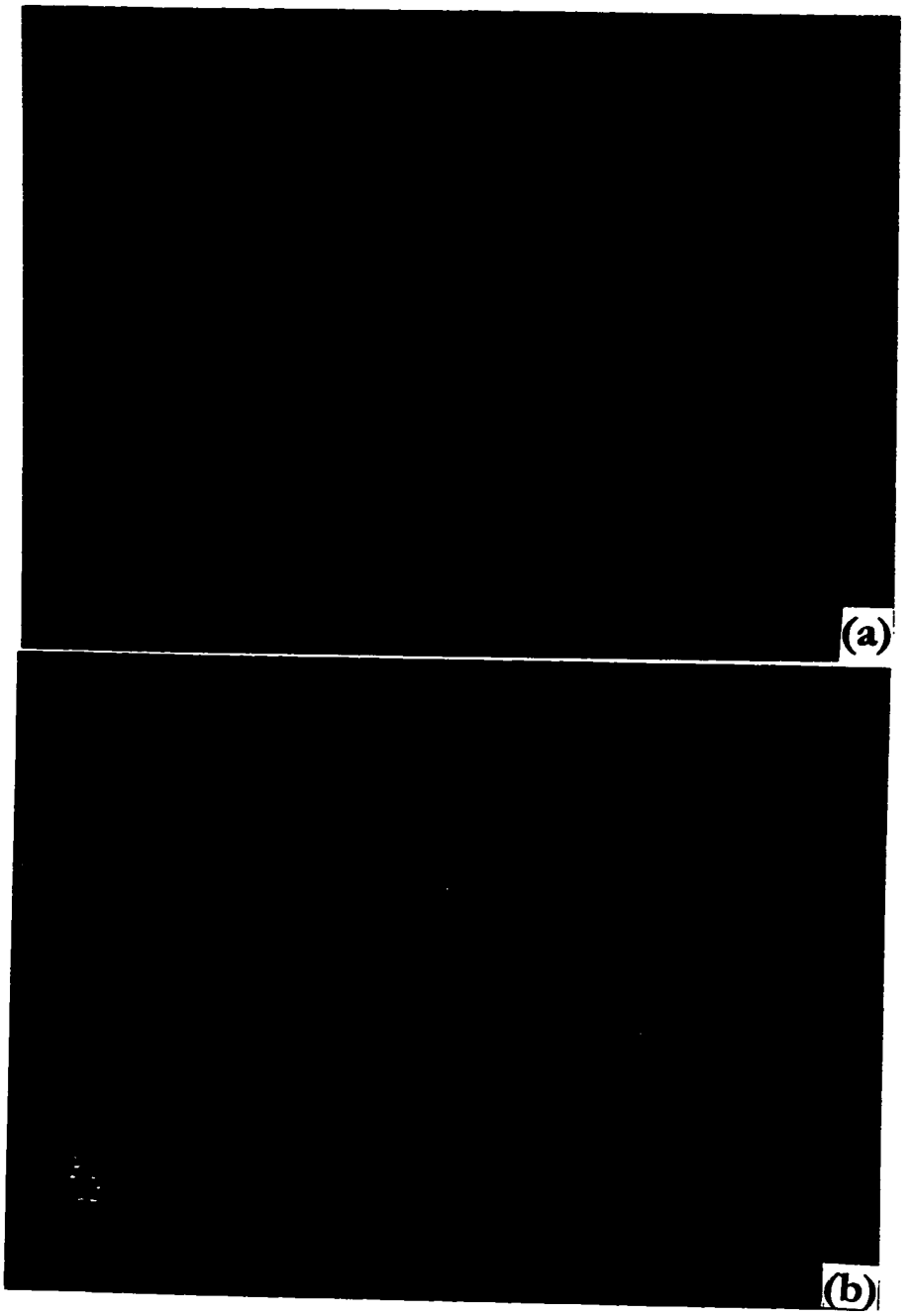

Figure 5.41 Micrograph of alloy ZK60 at a) 360°C, $\dot{\varepsilon} = 0.1\ s^{-1}$, $\varepsilon_f = 0.45$, X200. The newly formed DRX grains can be seen along the twin and grain boundaries. However, there are still some GB at which there are serrations without nuclei; b) 420°C, $\dot{\varepsilon} = 0.1\ s^{-1}$, $\varepsilon_f = 0.60$, X200. The new DRX grains have formed in the highly deformed sections of the gage area (left). As there is little evidence of twins, nucleation occurs entirely at GB.

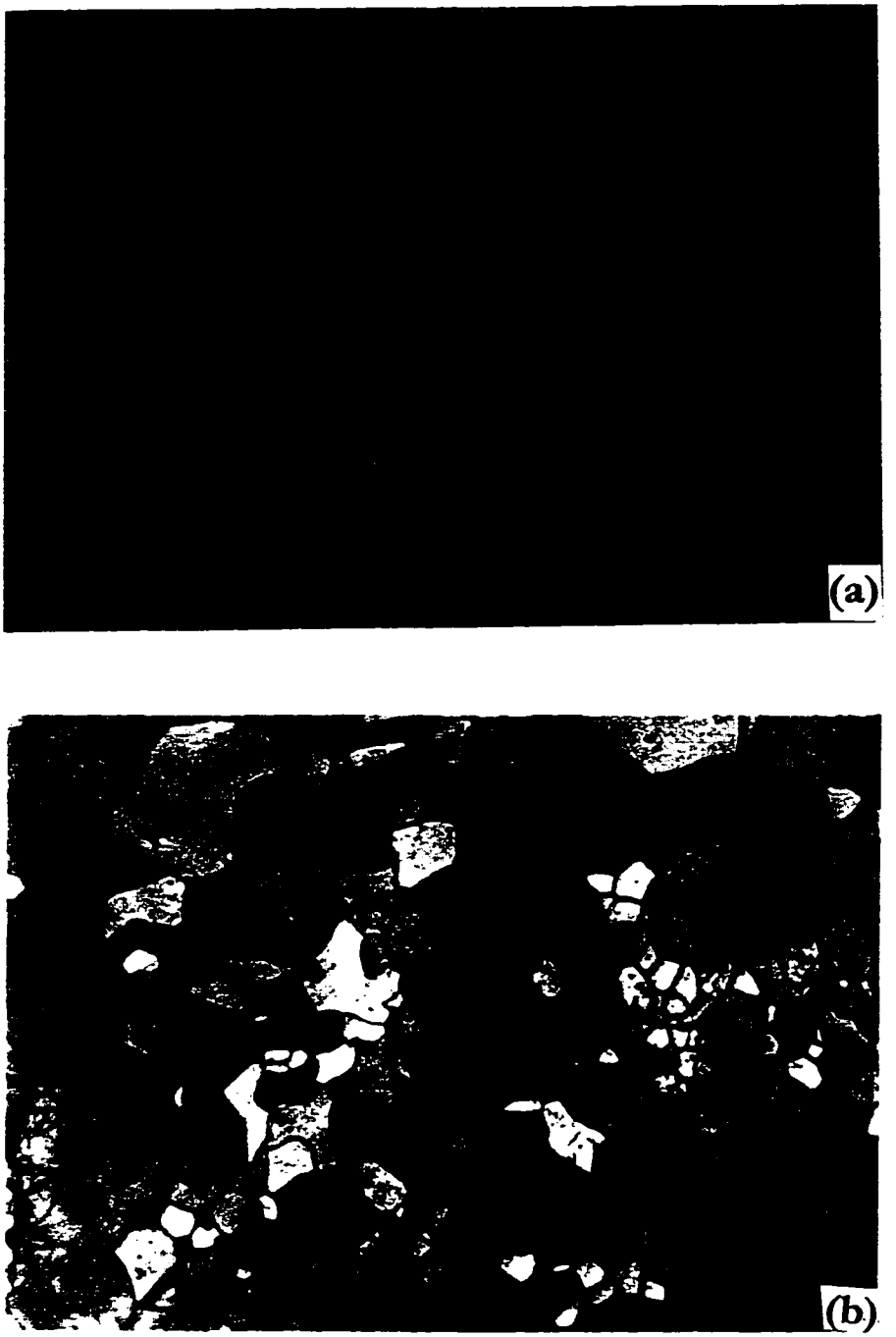

Figure 5.42 Micrograph of alloy ZK60 at a) 420°C, $\dot{\varepsilon} = 0.01\ s^{-1}$, $\varepsilon_f = 0.31$, X200, showing the tangential region completely consumed by the new DRX grains; b) 450°C, $\dot{\varepsilon} = 0.01\ s^{-1}$, $\varepsilon_f = 0.40$, X200, showing the deformed gage area with new grain distributed fairly evenly.

5.2.4 Optical Metallography of Alloy AZ63

Microanalysis was performed for the alloy AZ63 (Mg-5.5Al-2.7Zn-0.34Mn) at 240, 300, 360 and 420°C and strain rate 1.0, 0.1 and 0.01 s-1. At 240°C (Figure 5.43a) the volume of twins increases with increasing strain rate. Large twins gradually transform into separate grains as the morphology of the twin boundaries alter notably at high temperatures. With an increase in the degree of deformation, the twins bend, become wavy and begin to migrate. At 300°C new DRX grains can be clearly seen in Figure 5.43(b).

In the intermediate T region, 300°C (0.66 Tm, K) increased plastic flow leads to the formation of chains of new grains, mainly along initial grain boundaries and occasionally on those of twins. For the initial GBs with especially high dislocation density, the process begins early and proceeds more intensely; here the formation of new grains occurs and leads to the appearance of a 'mantle' (Figure 5.44), whose thickness continuously increases during deformation. Even when deformation is high, the microstructure consists of large and elongated remnants of the initial grains containing twins, with regions of small recrystallized grains in them.

At high T the gage area has patches of complete recrystallization. The flow stresses are much reduced and the ductilities increased as a result of more extensive DRX and SRX (Figure 5.45). In many regions there are multiple layers of DRX grains at the original GB, leaving 30-40% of the grain centers unaffected. Intense shear in some mantle regions can lead to DRX grain refinement.

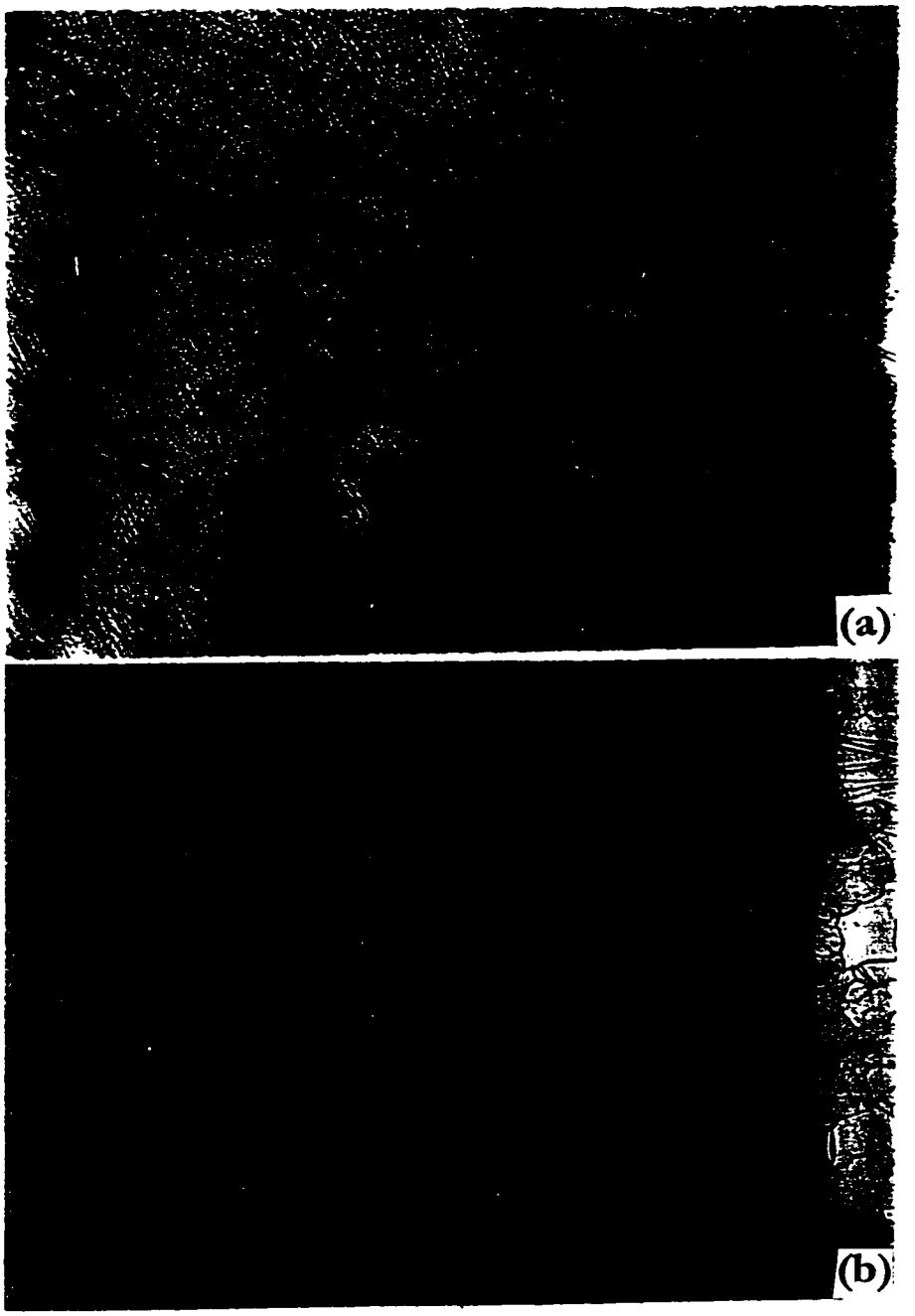

Figure 5.43 Optical micrograph of hot worked AZ63 in the warm working range, a) gage section at 240°C, $\dot{\varepsilon} = 0.1\ s^{-1}$, $\varepsilon_f = 0.30$, X200. i.e. without DRX. The gage area is highly deformed as can be seen by the number of twins; b) transition area at 300 °C, $\dot{\varepsilon} = 1.0\ s^{-1}$, $\varepsilon_f = 0.40$, X200. Some twins within the old grain are evident while the new DRX grains can be seen along twin boundaries and intersections. The undeformed shoulder is on the left.

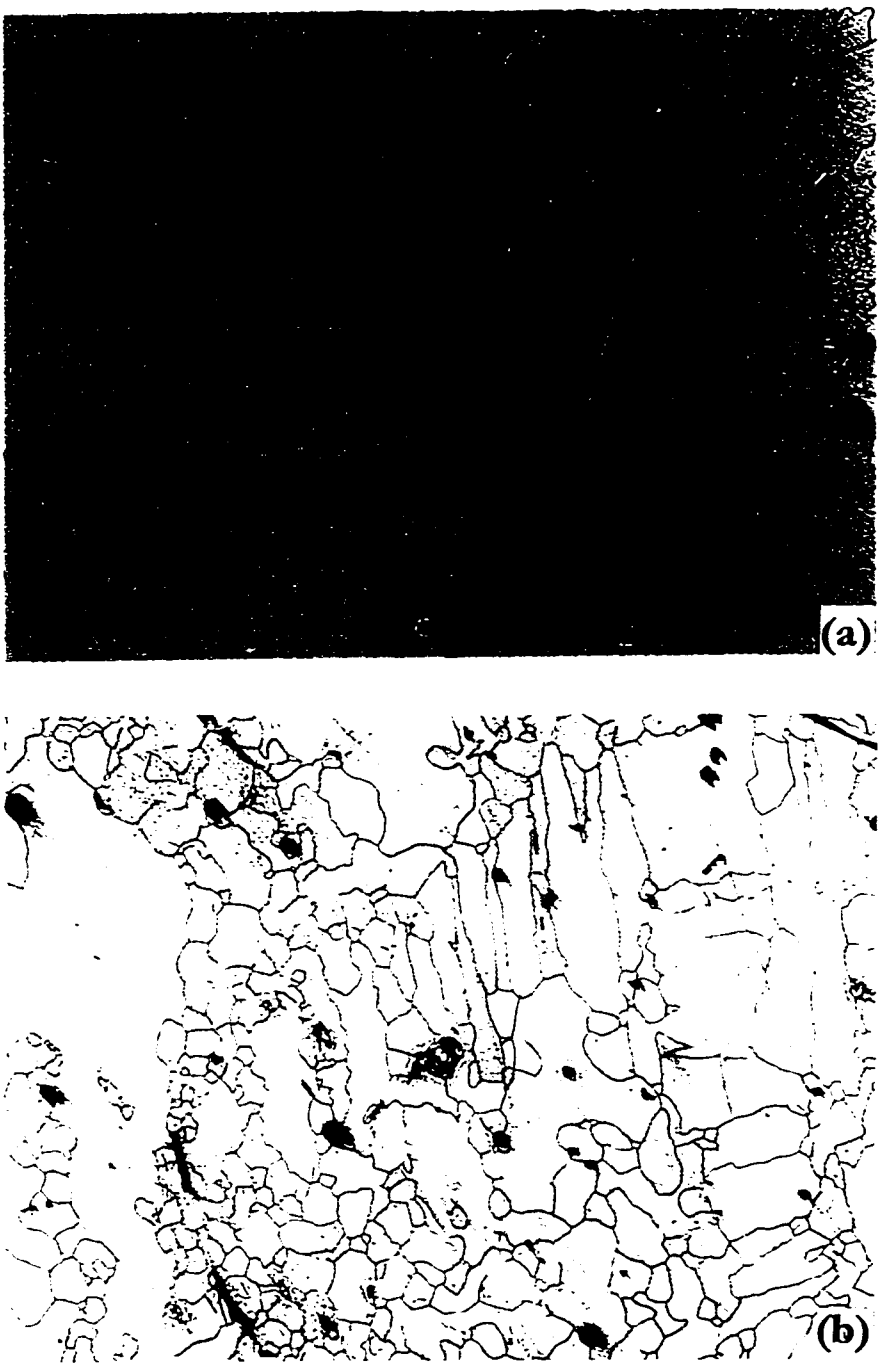

Figure 5.44 Micrograph of alloy AZ63 at 360°C, a) $\dot{\varepsilon} = 1.0\ s^{-1}$, $\varepsilon_f = 0.15$, X200. The micrograph shows the shoulder (left) and gage (right) sections. The grains have formed at GB and at twin intersections; b) $\dot{\varepsilon} = 0.01\ s^{-1}$, $\varepsilon_f = 0.40$, X200, the gage section has DRX grains as well as elongated grains.

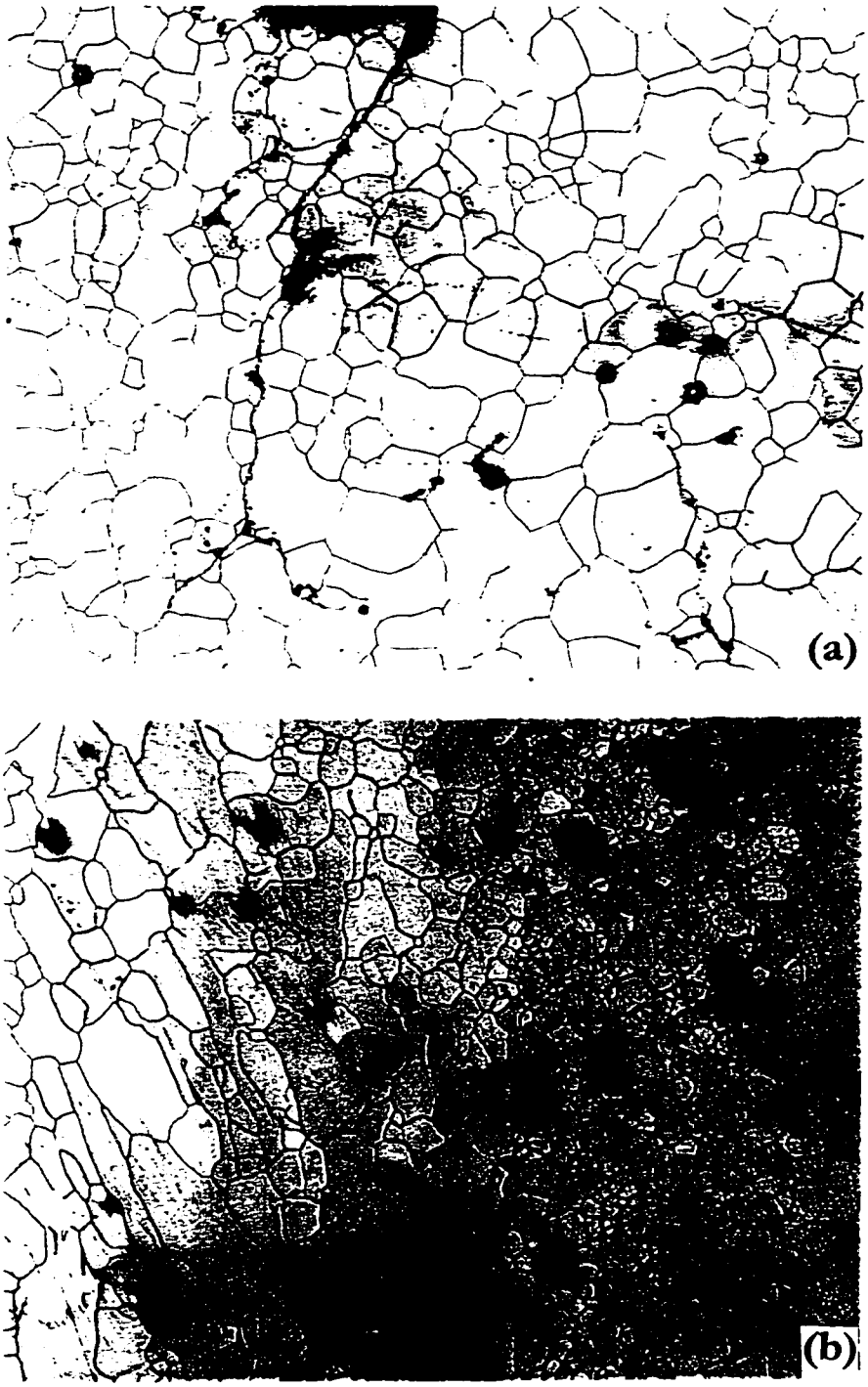

Figure 5.45 Micrograph of alloy AZ63 at 420°C, a) $\dot{\varepsilon} = 0.1\ s^{-1}$, $\varepsilon_f = 0.10$, X200 DRX grains distributed fairly evenly in the gage section; b) $\dot{\varepsilon} = 0.01\ s^{-1}$, $\varepsilon_f = 1.0$, X200, the small grains are evidence of DRX.

6.0 DISCUSSION

Flow curves decrease in peak stress but exhibit greater ductility associated with work softening and approach to steady state. The dependence on $\dot{\varepsilon}$ is reasonably filled by a $(\sinh\alpha\sigma)^n$ relationship and by the Arrhenius function with a Q value for climb controlled creep. The deformation mechanism shifts from twinning, basal slip and climb, DRV to DRX consistent with decrease in flow stress and increase in ductility

Twinning is the predominant deformation mechanism in magnesium alloys in the low T regime (Table 6.1). On formation, the twins had the characteristic lenticular morphology and on further straining the twins consumed more of the original grain. In the high T region, dynamic recrystallization (DRX) is the predominant softening mechanism. However, dynamic recovery, which is clearly observed in creep of Mg with strong similarities to the behavior of Zn [13,14], plays a significant role although not made apparent by the present microstructural techniques. The extent of DRV was made clear by transmission electron microscopy (TEM) examination conducted on AZ31 specimens [105]. The σ-ε curves which at high T rise to a peak and then a decline to a steady state plateau are evidence that DRX is occurring; reduction in the peak stress and strain with rising T are further confirmation. The strain hardening rate before the peak and the final stress level decrease as temperature rises, giving evidence that the dislocation densities which control the strain hardening rate are reduced by DRV. The activation energies in Table 5.1 are close to the value reported for creep.

In the low T domain, associated with basal glide, the activation energy Q_C equals 135-140 kJ/mol [31,32], being in good agreement with diffusion, Q_D=135 kJ/mol and confirming

Table 6.1 Summary of Alloy Parameters

Alloy	σ_p/ε_f at 240°C, 1.0 s^{-1} (MPa)	Q_{HW} KJ/mol	Principal Deformation and Softening Mechanisms at 240°c	σ_p/ε_f at 420°C, 1.0 s^{-1} (MPa)	Principal Softening Mechanisms at 420°c
AZ31-Mn	235/0.50	138	Twinning and DRV	82/0.86	DRX and DRV
AZ91	170/1.00	125	Twinning and DRV	80/1.25	DRX and DRV
AZ31	185/0.55	130	Twinning and DRV	71/0.75	DRX and DRV
ZK60	137/0.10	140	Twinning and DRV	88/0.36	DRX and DRV
AZ63	257/0.30	144	Twinning and DRV	35/0.10	DRX and DRV

climb as rate controlling [22-34]. The same activation energy extends to high T in the hot working because the high $\dot{\varepsilon}$ and σ preclude rate control by cross-slip [22-26] which is found in the high T domain (>0.7-0.8 Tm), where prismatic slip is clearly occurring [22-26], and gives a Q_C equaling about 230 kJ/mol [21-29,35,42]. The activation energy in creep, for the alloy Mg-0.8%Al calculated by S. S. Vagarali and others [59], was found to be in the range 140 ± 10 kJ/mol, which is in good agreement with the activation energy for the 5 alloys investigated in this research.

6.1 Continuous Deformation Behavior of AZ31-Mn and AZ31

Representative strain-stress curves of alloys AZ31-Mn and AZ31 are presented in Figure 5.6. In the temperature range 150-240°C failure occurs near the peak but at higher temperatures failure occurs after the peak. At 280°C and above the flow curves exhibit a smooth peak at low strains followed by a steady decline towards a plateau. The peak stresses σ_p of AZ31-Mn decline fairly smoothly with rising T and decreasing $\dot{\varepsilon}$: from as high as 248 MPa at 180°C and 0.1 s^{-1} down to 22 MPa at 450°C and 0.01 s^{-1} (Figure 5.10). Similarly, the peak stresses σ_p of AZ31 decline from 193 MPa at 180°C and 1.0 s^{-1} to 22.7 MPa and 0.01 s^{-1} (Figure 5.12). In the constitutive analysis for T and σ dependency of peak stresses, the slopes n at low T do not fit very well with the n value at other test temperatures (Figures 5.20, 5.22); possibly due to the fact that in Mg at low T, deformation is primarily on basal planes, while at higher T, the onset of DRX and slip on prismatic planes improves

ductility. At low T, the peak stress may be abnormally reduced as a result of premature fracture of the specimen, due to the presence of voids.

The ductility of both alloys AZ31 and AZ31-Mn (Figures 5.15-5.16) generally rise with increasing T becoming almost twice as great in the hot working region with DRX as in the warm working regime. Increased $\dot{\varepsilon}$ clearly lowers the fracture strain due to increased stress concentration and higher ε_p for DRX; the reduced and variable fracture strains at high T and $\dot{\varepsilon}$ may be related to deformation heating and melting of segregated phases at the grain boundary. At 180°C the ε_f of AZ31 is between 0.4 and 0.6, but it rises to as high as 2.0 at 450°C.

The microstructural developments of the two alloys are described together because they were very similar even though the small difference in composition of the two variants is sufficient to alter the hot strength and constitutive equation. In the warm working region 180-240°C (Figure 5.32), the grains exhibit evidence of twinning which appear as long lenticular regions. The twins intersect each other and distort the GBs. For the intermediate region 300°C (Figure 5.33), necklaces of new DRX grains appear at GBs. At 360-450°C (Figure 5.34), the true hot working regime, multiple layers of DRX grains can be seen at the original boundaries.

The activation energies of 138 and 130 kJ/mol for AZ31-Mn and AZ31 respectively are consistent with values observed in creep where basal glide and climb predominated.

6.2 Continuous Deformation Behavior of AZ91

The hot working behavior of AZ91 is very similar to the AZ31 type alloys. The additional alloying results in more precipitates, however it is sufficiently coarse to have little additional effect in the strength The flow curves at 240°C and above, where there is reasonable ductility, indicate a peak and flow stress decrease, giving evidence of DRX. The flow stress declines fairly smoothly as T rises (Figure 5.7); the higher values at 300 and 360°C are considered to be due to the refined TMP structure. It is clear that σ_p decreases as T rises and $\dot{\varepsilon}$ declines, from as much as 250 to 34 MPa. Moreover, the fracture strain ε_f rises from about 0.75 to 2.5 as T rises at $\dot{\varepsilon} = 5.0\ s^{-1}$ but for each T, declines as $\dot{\varepsilon}$ rises, most noticeably from 2.5 to 1.25 at 420°C. These trends can be seen more clearly in Figure 5. 11 and 5.16 where σ_p and ε_f are plotted as functions of T. For higher $\dot{\varepsilon}$ the lines of constant $\dot{\varepsilon}$ are at a higher slope (Figure 5.11) but at lower slope (Figure 5.16).

The ductility of the as-cast specimens is quite good at 240 and 300°C due to the fine grain size resulting from die casting (Figure 5.7, 5.11). However, at 360°C and above, the ductility in the as-cast condition was almost negligible, probably the result of segregated phases. After a TMP at 300°C, 0.05 s^{-1} to a strain of 0.4, equaling about half of the fracture strain, they exhibited good total strain inclusive of that in the TMP (Figures 5.7, 5.11). The ductility rises with rising T because of the speed up of DRX which moves grain boundaries away from fissures thus halting their propagation.

The sinh equation seems to fit the data well (Figure 5.21). The data shows a discrepancy at high strain rates that could arise because cracking initiates at low strain so that

the material has no opportunity to work harden to the true peak. The Arrhenius plot shows a poor fit because the points at 300°C are too low compared to those at 360°C. If instead of a single line, one were to draw two segments, the result would give a higher Q at low T and a lower Q at high T which do not agree with reports of 230 kJ/mol at high T (about 0.7-0.8 Tm) due to cross slip onto prismatic planes. At the temperatures and strain rates used here, slip is primarily basal and softening is by dislocation climb; thus DRV plays a significant role both before DRX is nucleated and as it progresses. The present lines pass considerably above those points at 300°C, but fit the data quite well as shown in the Z plot (Figure 5.30) with an activation energy which agrees with the values reported for creep in the range 320-450°C, that is 135-140 kJ/mol [22-23], although 120 kJ/mol was proposed earlier [30-31]. The TMP at 300°C, 0.5 s^{-1}, ε_f = 0.2 shows a pass curve which conforms to the continuous curve and thus indicates that SRX between passes is only partial because the lower $\dot{\varepsilon}$ develops insufficient strain energy. The arrest had been inserted because partial SRX between passes can increase ductility by moving grain boundaries away from fissures, inhibiting their propagation [3-34]. However, the principal beneficial effect of the TMP was to reduce the effects of casting segregation.

At low test temperatures, 180-240°C, the microstructure shows uniformly distributed $Mg_{17}Al_{12}$ compound along grain boundaries; in some regions it can be seen as a dark phase. The twins are observed but due to the presence of the $Mg_{17}Al_{12}$ at the GBs, they cannot be clearly distinguished. At intermediate T (Figure 5.36), i.e. 360°C, the new DRX grains are clearly visible as most of the $Mg_{17}Al_{12}$ has segregated and appears as the dark phase. In the true hot working regime, 360-450°C (Figure 5.37), there is more extensive DRX with the new grains covering the entire area.

6.3 Continuous Deformation Behavior of ZK60

For ZK60 (Figure 5.8) the flow curves at low T and high $\dot{\varepsilon}$ show a low maximum stress and a very rapid decline from peak compared to AZ31 or AZ91; a large part of this is likely due to crack propagation since the ductility is also lower. In the high T regime, most notably at 0.01 s^{-1}, the flow curves indicate a peak and a decrease towards steady state; this evidence of DRX is confirmed by optical microscopy. The flow stress (Figure 5.13) declines fairly smoothly as T rises over the test range to reach levels similar to AZ31 and AZ91, thus indicating similar significance of the dynamic softening mechanisms. Despite the comparatively low flow stresses, the ductility remains much lower than those alloys even though there is an increase with rising temperature (Figure 5.18). The sinh equation seems to fit the data quite well (Figure 5.23) in that the constant T lines are maintained parallel; however, the slope is much higher than the other alloys, possibly indicating the absence of solute drag as in the Mg-Al alloys. The twinning appears to be more frequent and wider than in the Al alloys; moreover the twins show more evidence of slip. The Arrhenius plot Figure 5.9) fits the data quite well to give a slope lower than the other alloys (consistent with comment on Figure 5.13). The activation energy calculated to be 140 kJ/mol thus agrees with the data reported for creep in the temperature range 250-500°C. The mechanical behavior and constitutive results are consistent with rising DRV from 250-450°C. DRX is a significant softening mechanism in the above range.

The microstructure of ZK60 in the warm working region 180-240°C (Figures 5.38,5.39) shows twins in the lightly strained grains. The twins intersect each other and

distort the GBs with slip bands inside the twins. In the intermediate region, 300°C, while twins similar to those observed at low T are still evident, new DRX grains can be seen as necklaces along a number of GB segments (Figure 5.40(a)). In the true hot working region, 360-450°C (Figures 5.41,5.42), there is extensive DRX and the new grains can be seen, throughout the gage area. It also appears that DRX occurs more extensively and at lower T than in Al bearing alloys. It is strange that these factors do not lead to good ductility but cracking at solidification.

6.4 Deformation Behavior of AZ63

Representative multistage stress strain curves for alloy AZ63 are presented in Figure 5.9. In the warm working region, 180-240°C failure occurred just after the peak. At 300°C, the flow stresses work-harden to a peak and failure occurs thereafter. In the true hot working region 360-450°C and at 0.01 s^{-1} the alloy work hardens to a peak followed by a decline towards a plateau. The flow stresses generally decrease with increasing deformation temperature although the variations with strain rate are not consistent. The fractional softening in general does not change the flow curve substantially. The ductility of AZ63 is generally much lower than that of other alloys. The microstructural developments of AZ63 are similar to those of other alloys investigated. In the low T region (180-240°C) the grains exhibit evidence of twinning (Figure 5.43). In the intermediate T regime (300°C), new grains that have formed at GB and twin intersections are evident (Figure 5.44). In the high T regime (360-

450°C) DRX grains are distributed fairly evenly throughout the gage section. Dynamic recrystallization and static softening play a significant role above 360°C.

6.5 Flow Curves

In the temperature region 180-240°C, the flow curves of all 5 alloys generally work harden towards a peak and failure occurs either before it or immediately thereafter. The peak stresses generally decline with rising T and declining $\dot{\varepsilon}$. In the intermediate T region (300°C), the flow curves work harden to a plateau with gradual decline to failure. At 360°C and above the flow curves work harden to a peak with gradual decline to steady state. The flow stresses of AZ31-Mn were generally higher than all the other alloys. The flow curves at high temperatures exhibit the shape characteristic of DRX which is confirmed by microscopy.

At 240°C and $\dot{\varepsilon} = 1.0\ s^{-1}$ the peak stress for the 5 alloys rises from 138 MPa for the alloy ZK60 up to 234 MPa for AZ31-Mn. The peak stress for alloy AZ91 at 240°C and $0.5\ s^{-1}$ is 107 MPa. The dominant deformation mechanism is twinning which is clearly observed in the optical micrographs. Work hardening is limited by the occurrence of DRV, a thermally activated softening mechanism. At 420°C the flow stresses up to the peak are much reduced principally by DRV. The final softening near the peak and the decline towards

steady state are due to the occurrence of DRX. Failure of the specimen can be attributed to formation of voids at grain boundaries which finally link up and to some incipient melting following deformation heating.

The peak stresses of 4 alloys at 1.0 s^{-1} are shown in Figure 6.1 as a simple plot against temperature. The alloy AZ91tested at 5.0 s^{-1} exhibited comparatively low flow stresses possibly due to the strong segregation of the second phase. Generally the flow stresses of all the alloys decline with rising temperature in a fairly similar manner.

The present flow curves are confirmed by tests conducted by S. S. Vagarali and others [51] on Mg-0.8%Al solid solution alloy tested in hot compression up to 0.7 in the range 150-327°C, 10^{-6} to 10^{-1} s^{-1}. The σ-ε curves rise to a peak and drop to a steady state plateau. The strain hardening rate, the peak stress and strain and the final stress level decrease as temperature rises. S. E. Ion and others [39] tested Mg-0.8%Al specimens in uniaxial compression in the temperature range 150-350°C at strain rates between 10^{-6} and 10^{-1} s^{-1}, to strains up to 90%. The specimens were machined from extruded rod with a strong preferred orientation; some specimens were aligned with the basal planes parallel to the compression axis while for others those planes were aligned at 45° to the compression direction as shown in Figure 6.2. The peak stress was strongly dependent on the initial orientation of the specimen as well as on temperature. For specimens which had basal planes parallel to the compression axis, basal slip, the predominant slip mode at low T, was not favored. Rapid initial work hardening in such specimens was attributed to {1012} twinning which reorients the basal planes so they become more favorable for slip. Subsequently the flow stress rises until the onset of softening by DRX. In specimens with many grains favorably oriented for basal slip, there is a lower peak stress and higher strains. These results show a more complex behavior than the present randomly oriented cast specimens;

however, the peak stresses and work softening have many similarities. Kaibyshev et. al. carried out compression tests on pure magnesium (Fig 6.3) in the temperature range 20-500°C, 0.0013-0.065 s^{-1} [75]. In the initial stages of plastic flow, at low and intermediate temperatures, there is a sharp rise in flow stress to a peak followed by stabilization at lower stress levels; this behavior is consistent with the present results even though the strain rate is much lower.

6.6 Stress, Strain rate and Temperature Dependence

Flow stresses for all alloys generally declined with rising T and declining $\dot{\varepsilon}$. For AZ31-Mn the slight variation from this at 1.0 $s^{-1}$and 0.1 s^{-1} (180-360°C) can be attributed to variation in the amount of segregated phases at the GB which can lead to melting upon sufficient deformation heating. The strength for the alloy AZ63 generally declined with rising T and with decreasing $\dot{\varepsilon}$ from 1.0 to 0.1 s^{-1}. The dependence on $\dot{\varepsilon}$ is reasonably fitted by a log $\dot{\varepsilon}$ vs. log[sinh($\alpha\sigma$)] plot and the dependence on T by the Arrhenius function with a Q value near that for climb controlled creep. In Figures 6.4 and 6.5 the plots of log strain rate vs. log[sinh(as)] and 1/T K^{-1} respectively, at 1.0 s^{-1} for the 5 alloys show that the peak stresses decline with rising temperature and falling strain rate in a fairly consistent manner. It is clear that the alloy without Al i.e. ZK60 has a different temperature dependence in the Arrhenius plot compared to the alloys with Al, namely AZ31, AZ63 and AZ91.

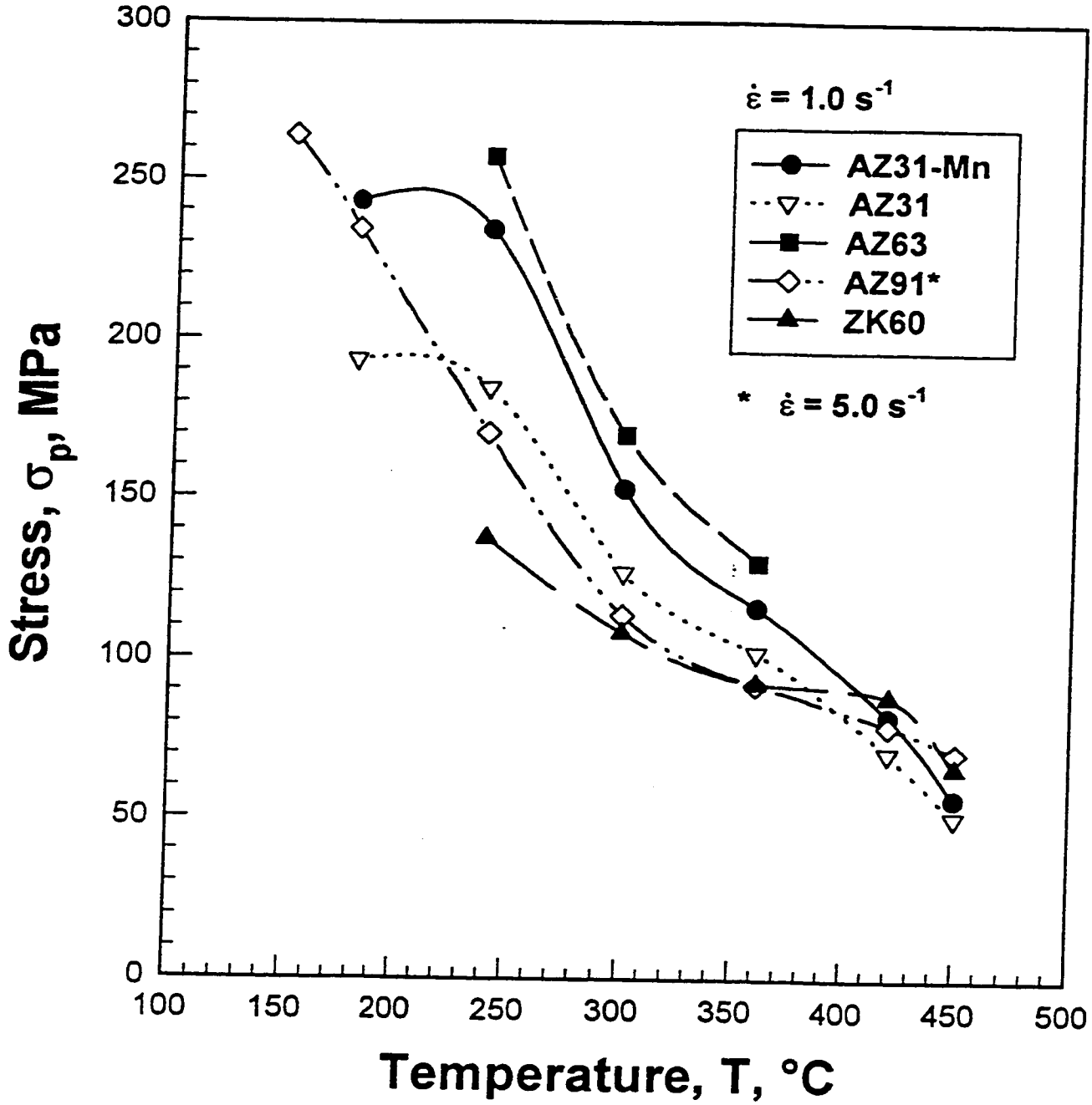

Figure 6.1 Comparison of the variation with temperature of the strengths of the 5 magnesium alloys at $\dot{\varepsilon}$ = 1.0 s^{-1} except for AZ91.

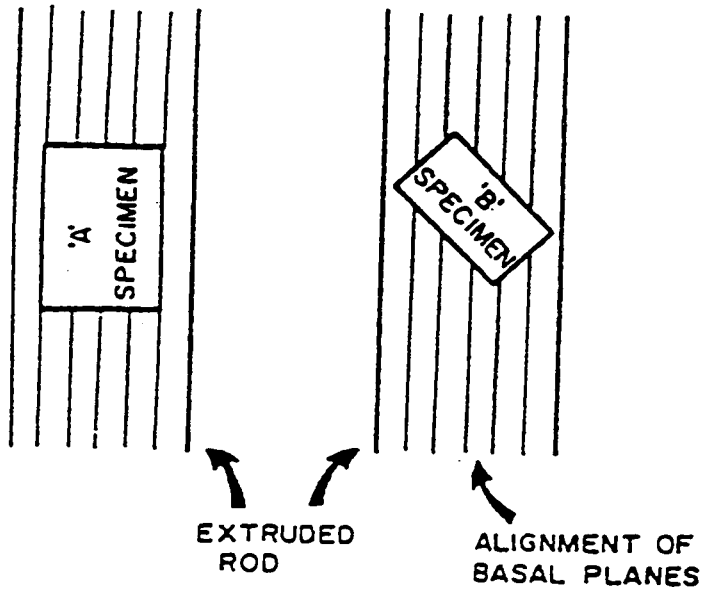

Figure 6.2 The orientation of the compression specimens with respect to that of the original extruded rod which had a strong preferred orientation (After Ion et. al. [39]).

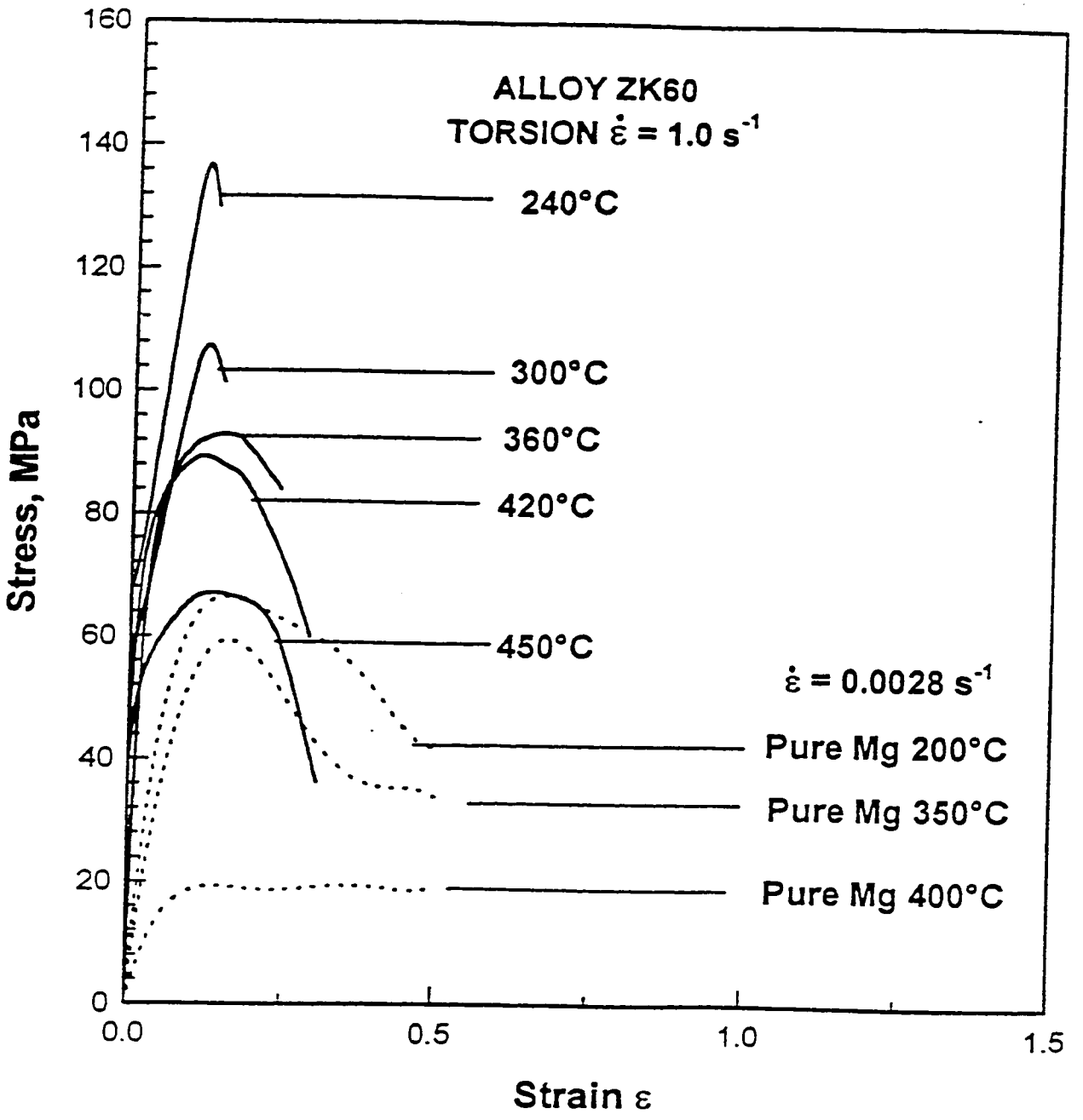

Figure 6.3 Flow curves of ZK60 and pure Magnesium (After Kaibyshev and Sitdikov [75]).

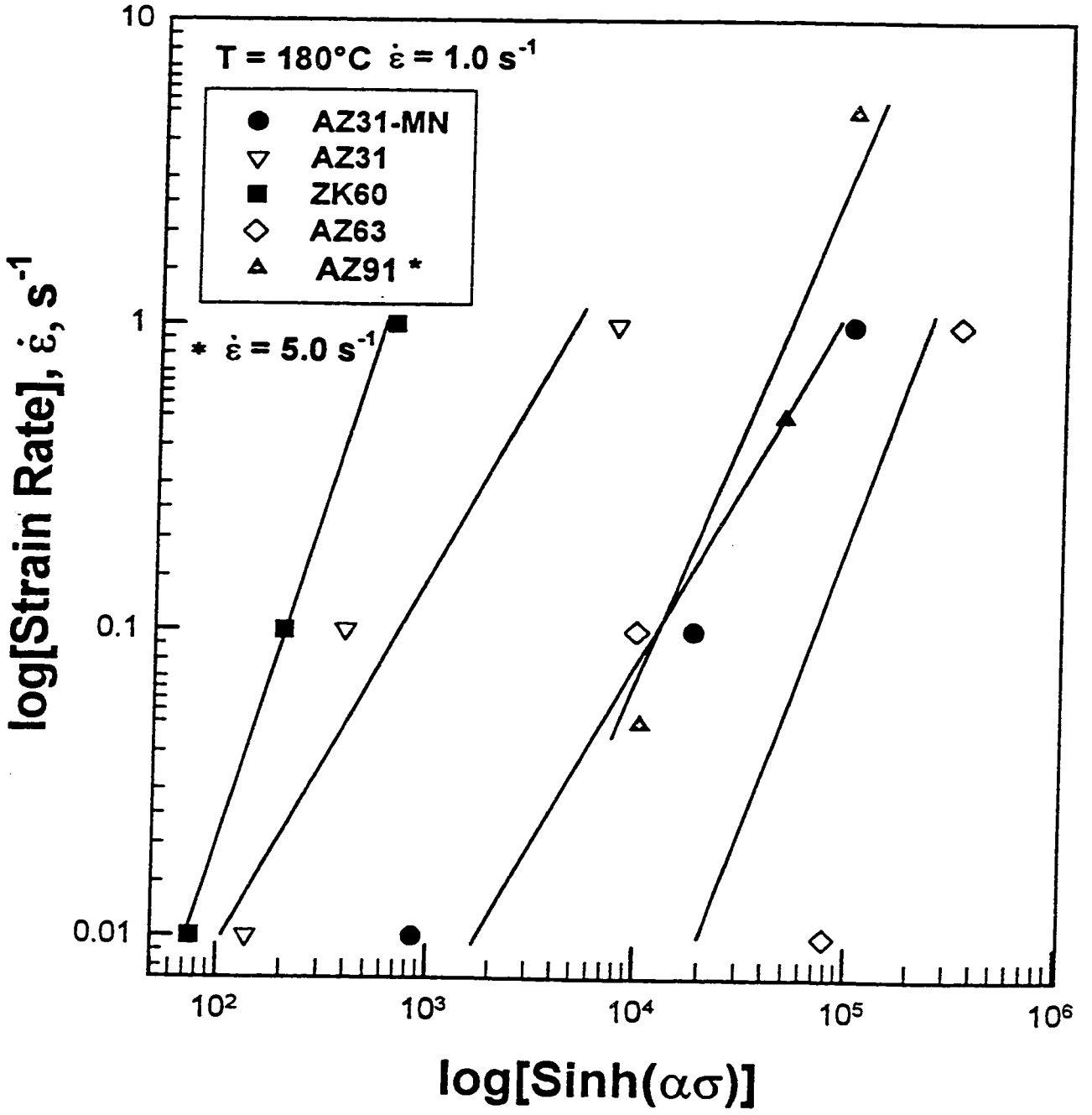

Figure 6.4 Plot of log$\dot{\varepsilon}$ vs. log[sinh(as)] for the 5 Magnesium alloys studied.

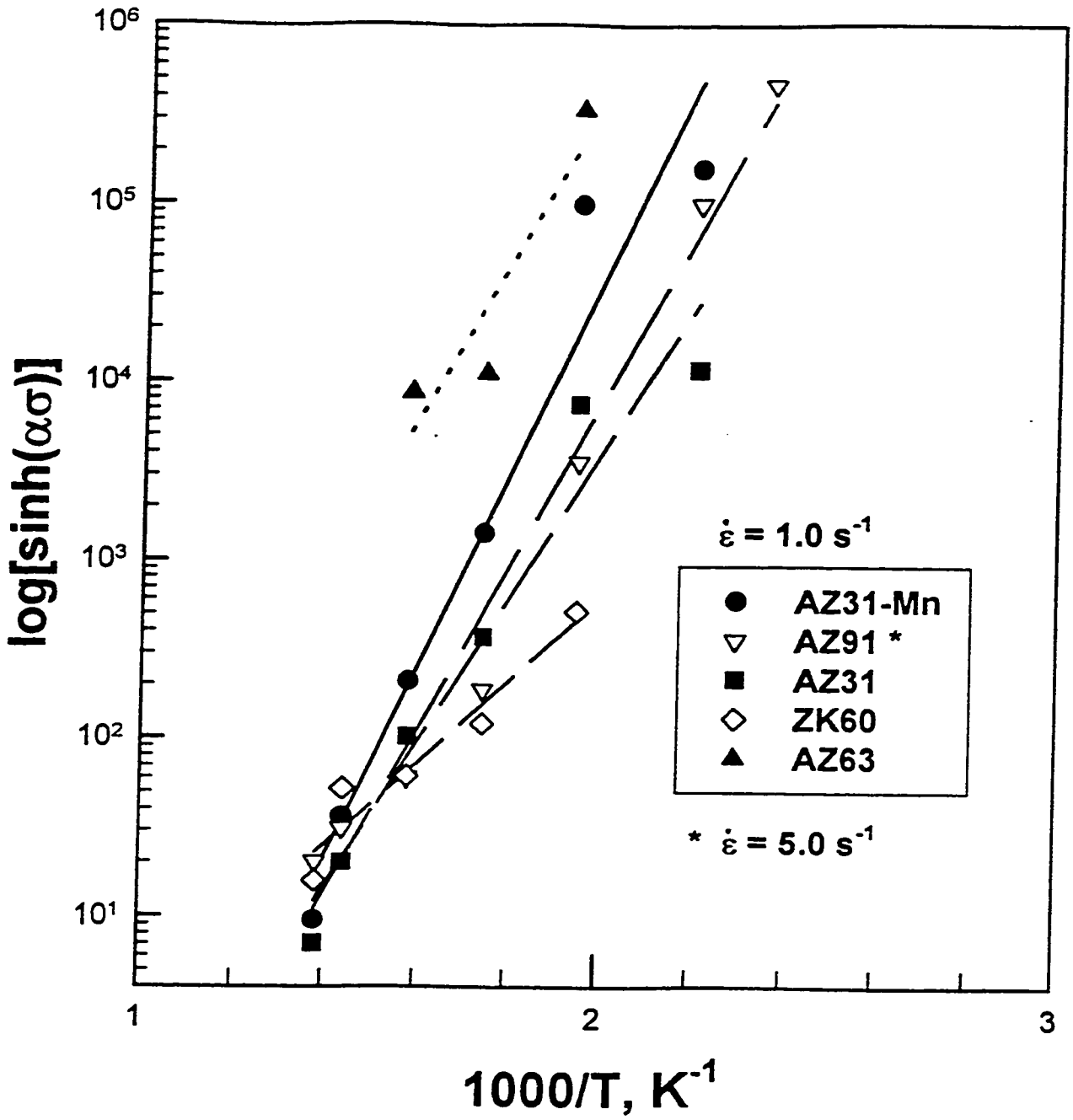

Figure 6.5 Plot of log[sinh(ασ)] vs. 1/T, K^{-1} for all the 5 alloys.

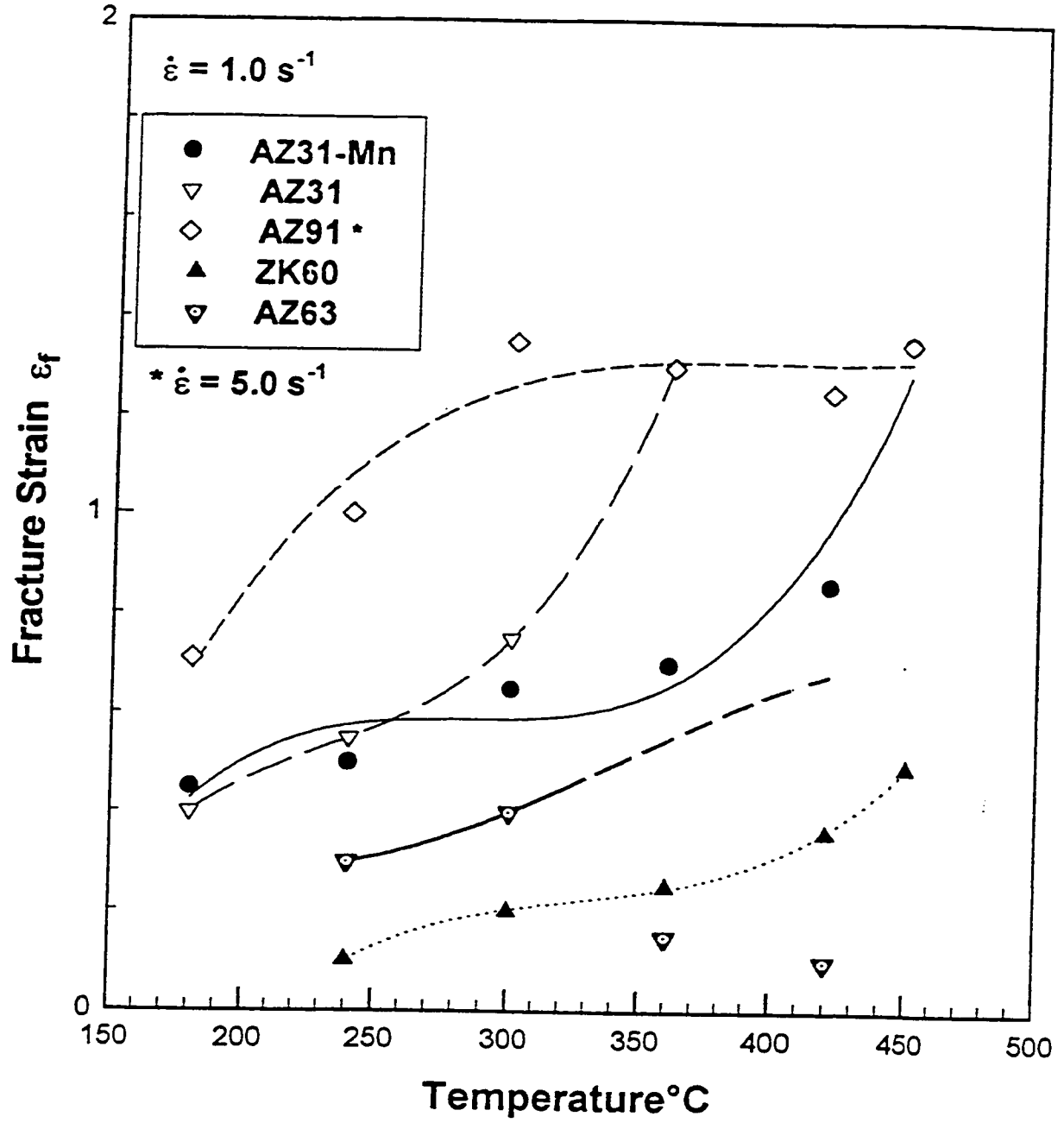

Figure 6.6 The ductility of the 5 alloys is highest for the die cast specimens AZ91 while ZK60 has the lowest ductility due to severe segregation.

6.7 Ductility

In general the torsional ductility rises with rising T and is higher for lower strain rate. The ductilities range between ~0.2 –1.0 below 300°C. At higher temperatures the ductilities rise to ~1.5 – 2.5 notably at low $\dot{\varepsilon}$. The rise in ductility is consistent with the decline in stress due to increasing dynamic recovery which reduces stress concentrations and grain boundary cracking. The ductility is further enhanced by the occurrence of DRX which separates GB from pores or fissures. The alloys AZ31-Mn, AZ31 and AZ91 exhibit this behavior with high strength levels compared to AZ63 and ZK60 which follows it less closely. For AZ63 ductility at 0.01 s^{-1} rises with T but at 1.0 and 0.1 s^{-1} it drops to as low as 0.12 at 420°C. This departure from the norm may be due to deformation heating and melting of segregated phases at the grain boundary.

The fracture strain variation with temperature for each of the 5 alloys at 1.0 s^{-1} is shown in Figure 6.6. It is clear that the fracture strain of the die cast alloy AZ91 with the finest grain size is the highest over the entire temperature range. Generally the two AZ31 alloys have similar fracture strains with marked differences only at the highest test temperature. The alloy ZK60 has low fracture strain due to bad segregation; however it improves with rising temperature. The alloy AZ63 has the most segregation and this explains its apparent low ductility; it appears to decrease with increasing temperature but this is likely due to excessive casting defects or segregation of the AZ63 specimens used in this study rather than being an alloy property. These problems were partly avoided in AZ91 with higher alloy additions

through the use of die cast specimens; but even these needed a treatment to improve homogeneity.

6.8 Microstructure

The present Mg alloys undergo initial twinning and basal slip [31,36,45]; dynamic recovery occurs to an increasingly high degree with decreasing Z consistent with a climb-control regime [44,53,59]. The mechanical, constitutive and ductility behavior are consistent with the occurrence of rising dynamic recovery which superimposes on twinning, lowering strain hardening [31-33]. In the alloys, dynamic recrystallization nucleates initially at the GB starting at about 300°C, 1.0 s^{-1} and becomes more widespread and with larger grains as the temperature rises and strain rate declines in similarity to previous work [11,22,39,40]. New DRX grains form primarily near grain boundaries in a broadening mantle as temperature rises; this seems sufficient to markedly improve ductility as a result of deformation in the small new grains as proposed by Humphreys et. al [39]. R.O. Kaibyshev and N.G. Zaripov [73] carried out tension tests on a fine grained magnesium alloy MA15 (Mg-3.1Zn-1.6Cd-0.95La), at 0.04 s^{-1} with an initial grain size of 15μm. Optical microscopic investigations led to the conclusion that the new fine grains with diameter 2-10μm, which formed along GBs, were the result of DRX.

6.9 Principal Hot Working Mechanisms

The principal hot working mechanisms, with peak stresses and fracture strains are summarized for 240 and 420°C in Table 6.1. It is evident from the table that stresses decrease and strains increase with rising temperature. At 240°C the flow stresses related to twinning are reduced by DRV while at 420°C the peak stresses are reduced by DRV although dynamic recrystallization becomes the dominant softening mechanism at higher strains. Previous results on creep of Mg alloys indicate that climb processes in association with basal glide [23,46,52] are active in the range 300-450°C exhibiting Q values of 135-140 kJ/mol (similar to self-diffusion) [25]. In creep of alloys with Al, the solute atoms form atmospheres near the dislocations thus slowing their climb and glide raising the flow stress. The power exponents near 3 which were observed in creep, are not expected at high $\dot{\varepsilon}$ as employed here [65,66]. Above 470°C in creep, prismatic slip became more frequent and cross-slip became rate-controlling with increase in activation energy to 230 kJ/mol [23-33]; however at high $\dot{\varepsilon}$ of hot working, insufficient testing has been done in this project to confirm this.

Subgrains are observed in creep above 0.7 Tm and form more readily when prismatic slip is occurring. Since additional slip systems are expected to operate near the GBs, subgrains form first near them. This was confirmed indirectly by the present optical techniques in the formation of serrations on GBs as they are induced to migrate down subgrain boundaries (SGB). Increasing misorientation of the SGB gives rise to the DRX nuclei along the GB.

The present range of DRX agrees reasonably well with that in Mg-0.58Zn-0.65Zr where it occurred from 250°C to 400°C at 10^{-4} s^{-1} [22,27]. These new grains were observed in conjunction with subgrains and GB serrations and, in the compressive strain range studied, did not exceed two or three necklaces at the periphery of the original grains. The layer of new grains was called a deformation mantle surrounding the cores of relatively rigid initial grains. The theory was proposed that further deformation in these small, randomly oriented DRX grains was easier than in large poorly oriented initial grains so that repeated DRX took place in them [22,26,73]. DRX did not progress to completion generally but only in the initial grains with favorable orientations. This form of DRX greatly improved the ductility but on some occasions gave rise to shear bands in the mantle.

The presence of subgrains in the present AZ31 specimens has been confirmed by an independent TEM study; with increasing T and decreasing $\dot{\varepsilon}$, augmented DRV causes the twin boundaries and the slip to become more diffuse and subgrains to develop. In addition, DRX grains were observed at grain boundaries and twin intersections [105].

6.10 Industrial Relevance

In industry, most of the guidelines used on working of magnesium alloys was obtained through practice and has been relatively stagnant for several decades. It is important to establish a data base for constitutive analyses to enable modeling of mechanical forming processes by precise mechanical testing at high temperatures. Such developments are necessary if magnesium is to take a more competitive role at a time where growing demand for light metals in land-transport is growing and precise production control is increasingly necessary. Knowledge of the deformation behavior of the complete range of industrial alloys is very beneficial when considering extending a particular forming operation to other alloys with increased product strength. For example, such analysis is important to a jobbing forge plant which must use existing machinery on alloys selected by the customer. Another important application is related to new installations where the forces required for expanded operations must be defined in order to design the new forming equipment. Information on the microstructures at different temperatures can be related to product properties so that the processing temperature of each alloy can be selected to provide the final characteristics desired.

6.11 Possible Future Work

1. The alloys can be tested after different homogenizing treatments to find out their effects on ductility and strength.

2. Tests can be conducted on worked homogenized material, which has reduced segregation and internal voids closed by rolling or extrusion. This would establish the inherent properties of the alloy.

3. Specimens from different places in the cast billet can be tested to determine the effect of segregation and as-cast microstructure on strength and ductility.

4. The effect of solution or overaging treatment on strength and ductility can be examined.

5. The effect of composition variation within the industrial specification limits on strength and ductility can be studied.

6. The optimization of composition to provide suitable variations on strength and ductility in order to facilitate processing.

7. Other industrial alloys can be studied to determine the dependence of strength and ductility on stress, strain rate and temperature.

8. The effects of specific alloying elements can be determined by special alloys with a range of compositions.

7. CONCLUSIONS

- With increasing deformation temperature and decreasing strain rate, the flow stresses decrease fairly uniformly and there is increasing progress towards a plateau with gradual decline. The shape of the flow curves indicate that dynamic recrystallization is a significant softening mechanism above 300°C. The alloys AZ31-Mn, AZ31 and AZ91 exhibit this behavior with high strength levels compared to AZ63 and ZK60 which follow it less closely.

- The sinh-Arrhenius constitutive equation adequately represents the peak flow stress dependence on temperature and strain rate. The sinh exponents of the alloys lie in the range 3.15 to 4.04 and the activation energies in the range 125 to 144 kJ/mol, consistent with climb control observed in creep.

- The ductility of the alloys AZ31-Mn, AZ31 and AZ91 (after a 300°C TMP to refine a segregated microstructure) increases fairly smoothly with rising T and lower $\dot{\varepsilon}$. The ductility is improved by increasing occurrence of dynamic recrystallization and in some cases by intermediate partial static recrystallization. The ductility of ZK60 is limited and the ductility of AZ63 is quite low.

- The present Mg alloys undergo initial twinning and dynamic recovery to a fairly high degree consistent with basal-slip climb control regime. The mechanical, constitutive and microstructural behavior and results are consistent with the occurrence of rising dynamic recovery which superimposes on twinning, lowering strain hardening and improving ductility.

- In the alloys, dynamic recrystallization initiates at about 300°C, 1.0 s^{-1} and becomes more widespread and with larger grains as the temperature rises and strain rate declines. New DRX grains form primarily near grain boundaries and twin intersections in a broadening mantle as temperature rises; this seems sufficient to markedly improve ductility.

- Magnesium alloys exhibit the principal hot working mechanisms found in other metals, but show numerous significant differences. There is scope to examine the behavior in greater detail over the entire hot working range and in a variety of alloys to see how some solutes and particles alter the mechanisms and thus affect the strength and ductility. Constitutive relations need to be determined with improved accuracy over a wide range for use in modeling industrial processes. The microstructural examination determines the mechanisms which give rise to the improved mechanical properties. However, the variation between microstructure developed during hot working and product properties would be valuable in design.

7. REFERENCES

1. H. J. McQueen and M. Pekguleryuz, "Magnesium Alloys and Their Applications", B. L. Mordike and F. Hehman, eds., DGM Oberursel, 1992, pp. 101-108.
2. H. Mecking, G. Gottstein: "Recrystallization of Metallic Materials", F. Haessner ed., Dr. Reidereer Verlag, Stuttgart, 1977, pp. 195-202.
3. S. Roberts, Magnesium and its Alloys, John Wiley and Sons, Inc., New York, 1960. pp. 17-41.
4. A. Mwembela and H. J. McQueen, "Hot Workability of Magnesium alloy AZ91", Light Metals and Applications, C. Bickert, M. Bouchard and others eds., CIM, 32nd Annual Conference of Metallurgists of CIM, Quebec City, 1993, pp. 523-532.
5. W. Lacomb, K. Spiradek, P. Kutlesa and G. Fetta, "Advanced Al and Mg Alloys", T. Khan, G. Effenberg eds., ASM International, 1990, pp. 815-822. Park, Ohio, 1993, pp. 815-821.
6. K. Buehler, Materials And Manufacturing Processes, Vol. 4, 1989, pp 603-616.
7. E. Taleff and O. Sherby, " Mechanical Behavior of Fine-grained Mg-6.5Li at Elevated Temperature",_Mater. Sci. Eng., Al 25, 1993 pp. 1-15.
8. Magnesium Die Castings, International Magnesium Association,_Maclean, Virginia, 1991.
9. H. J. McQueen and J. J. Jonas, Journal of Applied Metal Work., Vol.3, 1984, 233-241.
10. H. J. McQueen and J. J. Jonas, Journal of Applied Metal Work., Vol.3, 1984, pp. 410-420.

11. R. O. Kaibyshev and B. Solokov, Physics of Metals and Met., vol. 74, No. 1, 1992, pp. 72-78.

12. D. L. Bourell and H. J. McQueen, Journal of Mat. Shaping Tech., Vol. 5, 1987, pp. 53-53.

13. H. J. McQueen and D. L. Bourell, Journal Mat. Shaping Tech, vol. 5,1987, pp. 163-189.

14. H. J. McQueen and D. L. Bourell, Journal of Metals, Vol. 39, No. 7, 1987, pp. 28-35.

15. H. J. McQueen and J. J. Jonas, "Al. Alloys '90 (2nd Intl. Conf. Bejing.)",C. Q. Chen Ed, 1990, pp. 727-742.

16. H. J. McQueen and M. E. Kassner, "Superplasticity in Aerospace II", T. R. McNelly ed., TMS-AIME, Warrendale, PA, USA, 1991, pp. 189-206.

17. H. J. McQueen, E. Evangelista and M. E. Kassner, Z. Metalkde, Vol. 82, 1991, pp. 336-345.

18. H. J. McQueen, "Hot Deformation of Aluminum Alloys", T. G. Langdon et al. eds., AIME, Warrendale, PA, USA, 1991, pp. 31-54.

19. H. J. McQueen, Material Science Eng., Vol. A101, 1987, pp. 149-160.

20. T. Sakai and J. J. Jonas, Acta Metal., Vol. 32, 1984, pp. 189-209.

21. H. J. McQueen, E. Evangelista and N. D. Ryan, "Recrystallization ('90) in Metals and Materials", T. Chandra Ed., TMS-AIME, Warrendale, PA, USA, 1991, pp. 89-100.

22. S .E. Burrows, F .J. Humphreys and S. W. White, "Strength of Metals and Alloys (ICSMA5)", P. Haasen et al. Eds., Pergamon Press, Oxford, 1979, pp. 607-612.

23. Metals Handbook, Ninth Edition, vol. 2, Properties and Selection of Nonferrous Alloys and pure Metals, Metals Park, Ohio, U.S.A, 1978, pp. 525-609.

24. I. Polmear, Light Alloys- Metallurgy of the Light_Metals, R. Honeycomb and P. Hancock eds., Edward Arnold, London, pp. 169-173, 1989.

25. H. Mayer, R. Rosch, H. Liposky, B. Zettl, M. Papkyriacoul and S. E. Tschegg, Fatigue Properties of Die Cast Magnesium Alloys, The First Israeli International Conference on Magnesium Science and Technology, Israel, 1997.

26. B. Landkof and M. Gur, Magnesium Wrought Alloys Forming and Application, The First Israeli International Conference on Magnesium Science and Technology, Israel, 1997.

27. I. Dahan and E. Dabush, Microstructure Characterization of Rolled AZ31 Magnesium Alloys, The First Israeli International Conference on Magnesium Science and Technology, Israel, 1997.

28. I. Dahan and E. Dabush, Microstructure Characterization of Extruded AZ31 Magnesium Alloys, The First Israeli International Conference on Magnesium Science and Technology, Israel, 1997.

29. A. Ben-Artzi, et. al. Optimization of Rolling Process for the AZ31 Magnesium Alloy, The First Israeli International Conference on Magnesium Science and Technology, Israel, 1997.

30. N. C. Spare, "Magnesium Technology", The Institute of Metals, Book 396, 1987, pp. 36-39.

31. S. Roberts, Magnesium and its Alloys, John Wiley and Sons, Inc., New York, 1960. pp. 171-191.

32. T. Sheppard: "Proc. 8th Light Metal Congress", J. Jeglitsch et al. Eds., The University, Leoben, 1987, pp. 301-311.

33. G. E. Dieter, Mechanical Metallurgy, M. B. Bever et. al eds., McGraw-Hill Book Company, New York, U.S.A, 1986, pp. 114-127.

34. W.T Read Jr., Dislocations in Crystals, McGraw-Hill Book Co., New York, 1953, Chapt. 7.

35. A.Seeger, Report of The Conference on Defects in Crystalline Solids, The Physical Society, London, 1955, pp. 328.

36. C. S. Roberts, Magnesium and its alloys, John Wiley & Sons Inc., California, U.S.A. 1960, pp 84-93.

37. J. W. Suiter and W. A. Wood, "Deformation of Magnesium at Various Rates and Temperatures," J. Inst. Metals, 81, 1952 pp. 181.

38. C. S. Roberts, "Creep Behavior of Extruded Electrolytic Magnesium," Trans. AIME, 197, 1953 pp. 1121.

39. S. E. Ion, F. J. Humphreys and S. H. White, Acta Metall., vol. 30, pp. 1909-1919, 1982.

40. R. O. Kaibyshev, A. M. Galiev and B. K. Solokov, The Physics of Metall., vol. 78, no. 2, pp. 221-231, 1994.

41. A. Couret and D. Caillard, Acta Metall., vol. 33, no. 8, pp. 1447-1454, 1985.

42. G. I. Taylor, J. Inst. of Met., vol. 62, 1938, pp. 307.

43. U. F. Kocks, Acta Met., vol. 6,1958, pp. 85.

44. C. S. Roberts, "Creep Behavior of Magnesium-Cerium Alloys," Trans. AIME, vol. 200, 1954 pp. 634.

45. R. E Reed-Hill, Physical Metallurgy Principles, Princeton, New Jersey, U.S.A., pp. 399-418.

46. G. E. Dieter, Mechanical Metallurgy, McGraw-Hill Book Company, New York, U.S.A, 1986, pp. 132-135.

47. C. S. Roberts, Magnesium and its alloys, John Wiley and Sons Inc., U.S.A., 1960, pp. 88-93.

48. M. J. Luton and J. J. Jonas, Can. Met. Quart., vol. 11, 1972, pp. 79.

49. J. P. Richardson, C. M. Sellars and W. J. McG. Tegart, Acta Met., vol. 14, 1966, pp. 1225.

50. F. E. Hauser, C. D. Starr, L. S. Tietz, and J. E. Dorn, Trans. ASM, vol. 47, 1955 pp. 102.

51. S. S. Vagarali and T. G. Langdon, Acta Metall. vol. 30, pp. 1982, 1157-1170. Santa Barbara, California, U.S.A.

52. O. D. Sherby and P. M. Burke, Prog. Mater. Sci., vol. 13, 1968 pp. 325.

53. F. A. Mohamed and T. G. Langdon. Acta Metall. vol. 22, 1974, pp. 779.

54. W.J. McG. Tegart and O.D. Sherby, Phil. Mag. Vol. 3, 1958, pp. 1287.

55. B. L. Mordike, F. Moll and B. Sommer Creep behavior of Magnesium Matrix Composites, The First Israeli International Conference on Magnesium Science and Technology, Israel, 1997.

56. W. Blum, P. Weidinger, B. Watzinger, F. breutinger and R. Rosch, Creep of the Diecast Magnesium AlloyAZ91 and AS21, The First Israeli International Conference on Magnesium Science and Technology, Israel, 1997.

57. W.J. McG. Tegart and O.D. Sherby, Acta Metall., vol. 9,1961, pp. 861.

58. K. Milicka, J. Cadek and P. Rys, Acta Metall., vol. 18, 1970, pp. 1071.

59. S. S. Vagarali and T. G. Langdon., Acta Metall. Vol. 29, 1981, pp. 1969-1982.

60. H. J. McQueen and H. Mecking, "Creep and Fracture of Engineering Materials and Structures", B. Wilshire and D. R. J. Owen eds., Pineridge Press, Swansea, 1984, pp. 169-184.

61. H. J. Frost and M. F. Ashby, The Plasticity and Creep of Metals and Ceramics, Pergamon Press, 1982, TA.417.6.F76 pp. 43-49.

62. H. J. McQueen, W. A. Wong and J. J. Jonas, Canadian Journal of Physics, vol. 45, 1967, pp.1225-1234.

63. H. J. McQueen and W. J. M. Tegart, Scientific American, vol. 232, no. 4, April 1975, pp.116-124.

64. H. J. McQueen, Journal of Metals, vol. 18, no. 4, April 1968, pp. 31-38.

65. R. A. Petkovic, M. J. Luton, and J. J. Jonas, Canadian Metallurgical Quarterly, vol. 14, no.2, 1975, pp.137-145.

66. H. J. McQueen, Metallurgia I Odlewnictwo, vol. 5, no. 3, 1979, pp.421-451.

67. H. J. McQueen, E. Evangelista Czech. J. Phys., vol. B38, 1988, pp. 359-372.

68. H. J. McQueen and K. Conrod, Microstructural Control in Al Alloy Processing, E. Chia and H. J. McQueen Eds., TMS-AIME, Warrendale, PA, 1986, pp. 197-220.

69. C. M. Sellars, Phil. Trans, R. Soc. vol. A288, 1978 pp.178.

70. G. Glover and C.M. Sellars, Met. Trans, vol. 4, 1973, pp.765.

71. B. Stetac, Proc. 5th Int. Conf. On Strength of Metals and Alloys, eds., P. Haasen , V. Gerold and G. Kostorz, vol. 3, Aachen ,1979, pp.1461.

72. S. S. Vagarali and T. G. Langdon, Acta Metal., vol. 30, 1982, pp.1157-1170.

73. R. O. Kaibyshev and N. G. Zaripov, Fiz. Metal. i metalloved., vol. 66, No. 1, 1988, pp. 133-137.

74. S. S. Vagarali and T. G. Langdon, Acta Metal., vol. 29, 1981, pp. 1969-1982.

75. R.O Kaibyshev and O. Sitdikov, The Physics of Metals and Metallography, vol. 73 No. 6, 1992, pp 635-642.

76. H. J. McQueen and B. Baudelet: "Strength of Metals and Alloys (ICSMA5)", P. Haasen et. al. Eds., Pergamon Press, Oxford, 1979, pp. 329-336.

77. F. E. Hauser, T. R. Langdon and J.E. Dorn, Trans. Am. Soc. Metals, vol. 48, 1956, pp.968.

78. G. Sambasiva Rao, Y. V. R. K. Prasad: Met. Trans., vol. 13A, 1982, pp. 2219-2222.

79. J. Towle and T. Gladman, Metal Science, vol. 13, March/April 1979, pp. 246-256.

80. D. R. Barraclough and C.M. Sellars, Metal Science, vol. 13, March/April 1979, pp. 257-267.

81. H. J. McQueen, Canadian Metallurgical Quarterly, vol. 21,No. 4, 1982, pp. 445-460.

82. J. R. Pickens, T. G. Langan, R.O. England and M. Liebson, Metallurgical Transactions A, vol. 18A, February 1987, pp. 303-312.

83. H.J. McQueen and P. Sakaris, , "Mechanical Shaping of Metal Matrix Composites", S.V. Hoa and R. Gauvin eds., Elsevier Applied Science, London, 1992, pp. 297-306.

84. A. Espedal, H. Gjestland, N. Ryan and H.J. McQueen, Scandanavian Journal of Metals, vol. 18, 1989, pp. 131-136.

85. P. Sakaris, H.J. McQueen, Q. Meng, Y. Cui and B. Li, Advances in Production and Fabrication of Light Metals, CIM, Pergamon Press, Oxford, 1992 (in press).

86. K. Conrod and H. J. McQueen, Microstructural Control in Al Alloy Processing, TMS-AIME, Warrendale, PA, 1986, pp. 197-200.

87. D. S. Fields and W. A. Backofen, Proc. ASTM. 57, 1957, p1259.

88. S. Fulop, K. Cadien, M. J. Luton, H. J. McQueen, Journal of Testing and Evaluation, vol. 5, 1977, pp.419-426.

89. S. L. Semiatin, G. D .Lahoti and J. J. Jonas, vol. 8, ASM Metals Handbook, 9th Edition, ASM, Metals Park, Ohio, 1985, p.154.

90. P. Sakaris, "Hot Deformation Behavior of SiCp/Al Composites and Their Matrices and an Al-Mg-Si Alloy", Master Thesis, Concordia University, Montreal, 1993.

91. T. Maccagno, S. Yue, J. J. Jonas and K. Dyck, Metall. Trans. A, vol. 24A, July 1993, pp.1589-1596.

92. Operator's Manual, Materials Testing System No. 910.30, MTS System Corporation, MN, 1972.

93. P. N. Bakarian and C. W. Mathewson, Trans., AIME, vol. 152, pp. 226-254, 1943.

94. H. Sato and H. Oikawa, "Strength of Metals and Alloys (ICSMA9)", D. G. Brandon et al. eds., Freund Publishing, London, 1986, pp. 463-470, 1986.

95. H. J. McQueen, N. D. Ryan, E. V. Konopleva and X. Xia, Can. Metal. Quart., vol. 34, pp. 219-229, 1993.

96. T. G. Langdon, "Strength of Metals and Alloys (ICSMA5)", R. C. Gifkins ed., Pergamon Press, Oxford, pp. 1105-1120,1982.

97. H. J. McQueen K. Conrod and G. Avramovic-Cingara, Can. Metal. Quart., vol. 32, pp. 375-386, 1993.

98. G. R. Edwards, J. R. McNelly and O. D. Sherby, Scripta Met, vol. 8, pp. 475-480, 1974.

99. R. W. Cahn, I. J. Bear and R. L. Bell, Journal Inst. Met., vol. 82, pp. 481-489, 1953-54.

100. J. V. Sharp, A. Mitchell and J. W. Christian, Acta Metal., vol. 13, pp. 965, 1965.

101. H. J. Frost and M. F. Ashby, "Deformation Mechanism Maps", Pergamon Press, Oxford, 1982.

102. F. J. Humphries, "Deformation of Polycrystals", N. Hansen et al. Eds., Risö Natl. Lab., Roskilde, Denmark, pp. 305-310, 1981.

103. O. A. Kaibyshev, "Recrystallization ('90) in Metals and materials", T. Chandra ed.,TMS-AIME, Warrendale, PA, pp. 855-860, 1988.

104. K. Schemine, E. Hornbogen, "Advanced Al and Mg Alloys", T. Khan, G. Effenberg eds., ASM International, pp. 797-803, 1990.

105. M. Myshlaev, H. J. McQueen, A. Mwembela and E. V. Konopleva, Mat. Sci. Eng. (In Press).